This is to certify that the

dissertation entitled

Characterization of a Three-Phase Magnetically Stabilized Fluidized Bed Bioreactor

presented by

Vicki Sue Thompson

has been accepted towards fulfillment
of the requirements for

Ph.D. degree in Chemical Engr.

R. Mark Worden
Major professor

Date March 31, 1993

CHARACTERIZATION OF A THREE-PHASE MAGNETICALLY STABILIZED FLUIDIZED BED BIOREACTOR

By

Vicki Sue Thompson

A DISSERTATION

Submitted to
Michigan State University
in partial fulfillment of the requirements
for the degree of

DOCTOR OF PHILOSOPHY

Department of Chemical Engineering

1993

ABSTRACT

CHARACTERIZATION OF A THREE-PHASE MAGNETICALLY STABILIZED FLUIDIZED BED BIOREACTOR

By

Vicki Sue Thompson

Three-phase fluidized bed systems have many desirable properties such as excellent phase contacting, low pressure drops, reduced plugging, and reduced shear. However, at high gas flow rates, bubbles coalescence tends to reduce phase contacting, and increase shear and turbulence. Studies have shown that application of a magnetic field to two-phase fluidized beds can reduce or eliminate this undesirable behavior. The focus of this study was to examine the properties of a three-phase fluidized bed with an applied magnetic field.

Bed regimes, gas void fraction, axial liquid mixing and gas-to-liquid mass transfer were examined in this study. Six bed regimes were identified: random, chain, chain-channel, destabilized, channel, and frozen. Bed properties varied markedly from regime to regime. Local gas void fraction was found to increase 200% in the frozen regime. The axial dispersion coefficient, a measure of liquid mixing, decreased 400% in the chain-channel regimes for low liquid velocities, and gas to liquid mass transfer increased by 30% in the chain-channel and destabilized regimes. A mathematical model was also developed to predict the effect of intraparticle tracer diffusion into the solid phase on measurement of axial mixing. The

mathematical model allowed development of criteria to determine when intraparticle diffusion could be ignored relative to effects of dispersion and convection, and allowed correction of experimental measurements.

ACKNOWLEDGEMENTS

I would like to thank my parents, Kenneth and Carol Freund, for their support and patience through all of this. None of this would have occurred without them. I would like to thank my husband, David N. Thompson, for his support (both emotional and technical) during my project and the writing of this dissertation. I would like to thank my advisor, Mark Worden for his guidance during this project. Finally, I would like to acknowledge the Upjohn Company and the National Institute of Health for providing me fellowship support during my work.

TABLE OF CONTENTS

LIST OF TABLES

LIST OF FIGURES

NOMENCLATURE

Symbol	Description	Units
A	cross-sectional bed area	cm^2
a	gas-liquid interfacial area per unit liquid volume	cm
a_1	inner solenoid radius	cm
a_2	outer solenoid radius	cm
b	half length of solenoid	cm
C_{ad}	amount adsorbed in the beads	g/mL
C_B	bead concentration	g/mL
C_{expt}	experimentally measured concentration	g/mL
C_f	final solute concentration	g/mL
C_g	gas concentration	g/mL
C_{gi}	concentration at gas-liquid interface	g/mL
C_{go}	initial gas concentration	g/mL
C_i	initial solute concentration	g/mL
C_L	liquid concentration	g/mL
C_{Li}	concentration at liquid-gas interface	g/mL
C_L^*	liquid concentration in equilibrium with gas phase	g/mL
C_o	initial concentration	g/mL
D_{ax}	dispersion coefficient	cm^2/s
D_e	diffusion coefficient	cm^2/s
D_i	diameter of molecule i	Å
F	flow rate	mL/s
$F(s)$	transfer function	[-]
F_g	gas flow rate	mL/s
g	acceleration due to gravity	cm/s^2
g_w	mass of water	g
H	Henry's law constant based on partial pressure in gas phase	atm mL/g
H	Henry's law constant based on concentration in gas phase	[-]
H_B	bed height	cm
H_g	height of gas	cm
H_o	maximum field strength	gauss
H_z	axial field strength	gauss
i	angle of light incidence	°
i_o	angle of light refraction	°
I	current	amps
k_a	adsorption rate constant	s^{-1}
k_f	film mass transfer coefficient	cm/s
k_g	gas phase mass transfer coefficient	cm/s
k_L	liquid phase mass transfer coefficient	cm/s
k_La	volumetric mass transfer coefficient	s^{-1}
K_{ad}	adsorption equilibrium constant	g/mL
K_L	overall mass transfer coefficient	cm/s
K_p	partition coefficient	[-]
L	distance between measuring points	cm

L_B	bubble length	cm
L_C	column length	cm
m_n	n^{th} weighted moment	s^n
M	particle magnetization	$cm^{1/2}s/g^{1/2}$
M_n	n^{th} moment	s^n
n	refractive index of fluid	[-]
$n_{highest}$	highest moment used	[-]
n_o	refractive index of probe	[-]
N	number of turns of wire	[-]
N_m	ratio of kinetic energy to magnetization energy	[-]
N_v	voidage modulus	[-]
O_f	optical rotation	[-]
$O_{f,c}$	corrected optical rotation	[-]
p	dry weight of beads	g
P	pressure	kPa
P_E	partial pressure of gas at electrode	atm
P_T	total system pressure	kPa
Q	gas transfer rate	g/mLs
r	radial distance in beads	cm
R	radius of the beads	cm
R_{xy}	cross-correlation function	[-]
s	Laplace variable	[-]
t	time	s
t_B	time for bubble to traval across the probe	s
t_g	time probe spends in gas phase	s
$t_{max,input}$	time when input curve is maximum	s
$t_{max,response}$	time when response curve is maximum	s
T	total time	s
U	superficial velocity	cm/s
U_B	bubble velocity	cm/s
U_i	interstitial velocity	cm/s
V_B	accessible bead volume	mL
V_g	gas volume	mL
V_i	volume of water inaccessible to a molecule of diameter D_i	mL
V_L	liquid volume	mL
V_p	particle volume	mL
w	mass of solute	g
x_{O2}	mole fraction of oxygen in gas phase	[-]
z	axial position in bed	cm

Greek Letters

Symbol	Description	Units
α	ratio of liquid volume to accessible bead volume	[-]
α_p	fractional increase in pressure due to weight of bed	[-]
γ	bed conductivity	ohm
γ_L	pure liquid conductivity	ohm

δ_i	specific mass of water in pores inaccessible to a solute of size i	[-]
Δt_D	time delay between input and response curves	s
ϵ	root-mean-square error	[-]
ϵ_g	gas void fraction	[-]
ϵ_L	liquid void fraction	[-]
ϵ_p	bead porosity	[-]
ϵ_s	solid bed fraction	[-]
θ	angle between magnetic field and disturbance	°
λ	angle between flow and disturbance	°
ρ_B	bead density	g/mL
ρ_g	gas density	g/mL
ρ_L	liquid density	g/mL
ρ_p	particle density	g/mL
ρ_s	solid density	g/mL
ρ_w	density of water	g/mL
τ	1/2 time for the response tail to disappear	s
τ_E	electrode response time	s
τ_{max}	time for bubble to travel between probes	s
χ	chord susceptibility	[-]
$\hat{\chi}$	differential susceptibility	[-]

Chapter I: Introduction

Industrial applications for three-phase fluidized beds are numerous, with such examples as the H-oil process for hydrogenation and hydrodesulfurization of residual oil[1], flue gas desulfurization[2], the H-coal process for coal liquefaction[3], biological oxidation of waste waters[4], hydrogenation of unsaturated fats[5], and Fischer-Tropsch reactions[5]. The advantages of fluidized beds for these processes include excellent phase contacting, which eliminates the need for mechanical mixing, low pressure drops and shear, which prevent damage to fragile particles, and reduced plugging, which decreases the amount of process down time. Unfortunately, the desirable properties of three-phase fluidized beds disappear at higher gas velocities and in low density particle systems[6]. Under these conditions, bubbles tend to coalesce leading to increased agitation and shear, and less effective phase contacting. These problems have been alleviated in two phase fluidized beds by applying a uniform axial magnetic field to the bed. With the applied magnetic field, fluidized beds exhibit a wide range of operating conditions where bubble coalescence is eliminated, solids move through the bed in plug flow, mixing of the fluid phase is greatly reduced, and contacting efficiency between phases is increased[7,8,9]. To date, few studies have been conducted on three-phase magnetized fluidized beds, and no comprehensive analysis has been carried out on the bed characteristics.

In this study, the effect of an applied magnetic field on the gas void fraction, liquid mixing, and gas to liquid mass transfer properties of a three-phase system was examined. In addition, the

macroscopic bed structure, and how it changed with magnetic field strength, was characterized.

This dissertation is divided into six chapters. Following the introduction, the second chapter examines the history and development of the magnetically stabilized fluidized bed (MSFB) and discusses the methods used to measure and analyze the data from gas void fraction, liquid mixing and mass transfer studies. The third chapter is devoted to describing the design and construction of the three-phase magnetically stabilized fluidized bed, the experimental methods used to measure the bed properties, and the data analysis techniques used to analyze the data. In the fourth chapter, a mathematical model of the fluidized bed is developed to analyze axial dispersion data when intraparticle diffusion into the solid phase is present. The fifth chapter presents the results of this study, and the sixth chapter discusses the significance of these results and conclusions of the study. Also included in the dissertation are three appendices which include derivation of key equations, listings of the computer programs used to analyze the data, and tables of the experimental data.

Chapter II: Literature Survey

2.1 Fluidized Beds

Fluidized bed reactors offer properties that make them preferable to other types of reactors for the growth of living cells. They have lower pressure drops and fewer plugging problems than packed beds. The excellent phase contacting achieved in fluidized beds eliminates the need for mechanical mixing; thus, energy requirements are less than in stirred tank reactors. In addition, immobilizing cells on or within solid particles gives high cell densities and protects fragile cells from mechanical shear. Unfortunately, except under conditions of very low gas flow rates or in systems of large dense particles[10], the gas bubbles in fluidized beds tends to coalesce, even forming large slugs in reactors having diameters less than three inches. Coalescence is particularly inherent in systems of light particles such as porous biocatalyst particles[6]. Coalescence and slugging greatly reduce phase contacting and may reduce the rate of oxygen transfer below that needed by the cells. Also, larger bubbles increase bed turbulence and damage to the particles and cells. Entrainment of particles and loss from the bed is also exacerbated by coalescence.

Over the last decade, extensive work on gas-solid and liquid-solid fluidized bed systems has shown that application of a magnetic field can greatly reduce or even eliminate the problems mentioned above. However, the effects of magnetizing three-phase fluidized beds have not been well characterized to date.

The following sections of this chapter will examine in depth the properties of gas-solid, liquid-solid and three-phase magnetized

systems, and examine the theory and measurement techniques for bed properties of phase holdup, liquid mixing and mass transfer of three-phase fluidized beds.

2.2 Magnetically Stabilized Fluidized Bed (MSFB)

2.2.1 Early Studies

The first reports of an MSFB were published in the early 1960's in the eastern European literature by Filippov[11-15], who magnetized water-fluidized bed of iron particles magnetized using an A.C. magnetic field. He observed that the transition from a packed to fluidized bed occurred at the same pressure drop as an unmagnetized bed. He also observed the appearance of five distinct regimes or phases in the bed properties which depended upon field strength and fluid velocity: i) packed, ii) pseudopolymerized, characterized by chaining of particles and lack of particle movement, iii) start of particle motion, iv) extensive particle mixing, and v) particle entrainment at very high fluid velocities. Kirko and Filippov[12], showed the entire bed could be levitated as a cohesive unit at very high field strengths. This phenomenon is now referred to as a frozen bed[16]. At approximately the same time, Herschler[17,18] observed that a fluidized bed of permanently magnetized particles subjected to an A.C. magnetic field was free of bubbles, slugs and channelling. Katz and Sears[19,20] found that a fluidized bed could still be stabilized down to a solid-phase volume fraction of 20%. Shumkov and Ivanov[21] reported that bed porosity became almost uniform along the length of the bed when a magnetic field was applied. Several researchers observed an increase in bubble frequency and decrease in bubble size in the MSFB[22-27]. Stabilization

was also shown to increase the apparent viscosity of the bed[11] and decrease the heat transfer coefficient from that of an unmagnetized fluidized bed[28]. More complete reviews of early studies have been done by Siegell[17] and Liu *et al.*[29]. Almost without exception, the above studies were conducted with time-dependent magnetic fields or fields with high gradients. In the late 1970's researchers began to focus on uniform, D.C. magnetic fields starting the Rosensweig's work on gas-solid systems.

2.2.2 Gas-Solid MSFB

The first comprehensive examination of gas-solid MSFB was conducted by Rosensweig, who was awarded two patents for the magnetically stabilized bed[7,30]. In his first paper[8], he described the response of a gas fluidized bed of nickel particles with and without an applied field. Without a field, gas in excess of the minimum fluidization velocity passed through the bed in the form of bubbles and slugs reducing contacting efficiency. When a uniform, axial D.C. field was applied bubbles did not form, and the bed was free of agitation or solids movement. The bed exhibited characteristics of a liquid: light objects floated and dense objects sank; also the suspension flowed from an orifice easily like a liquid. As the gas velocity increased, this stable regime was found to eventually give way to bubbling. Figure 2-1 shows a phase diagram of a magnetized fluidized bed. The transition from the stable phase to the unstable was described by Rosensweig[8,9] as sharp and reproducible. He also found that the magnetic field had no effect on the minimum fluidization velocity, and that the pressure drop increased linearly with gas velocity until the pressure drop equalled the weight of the

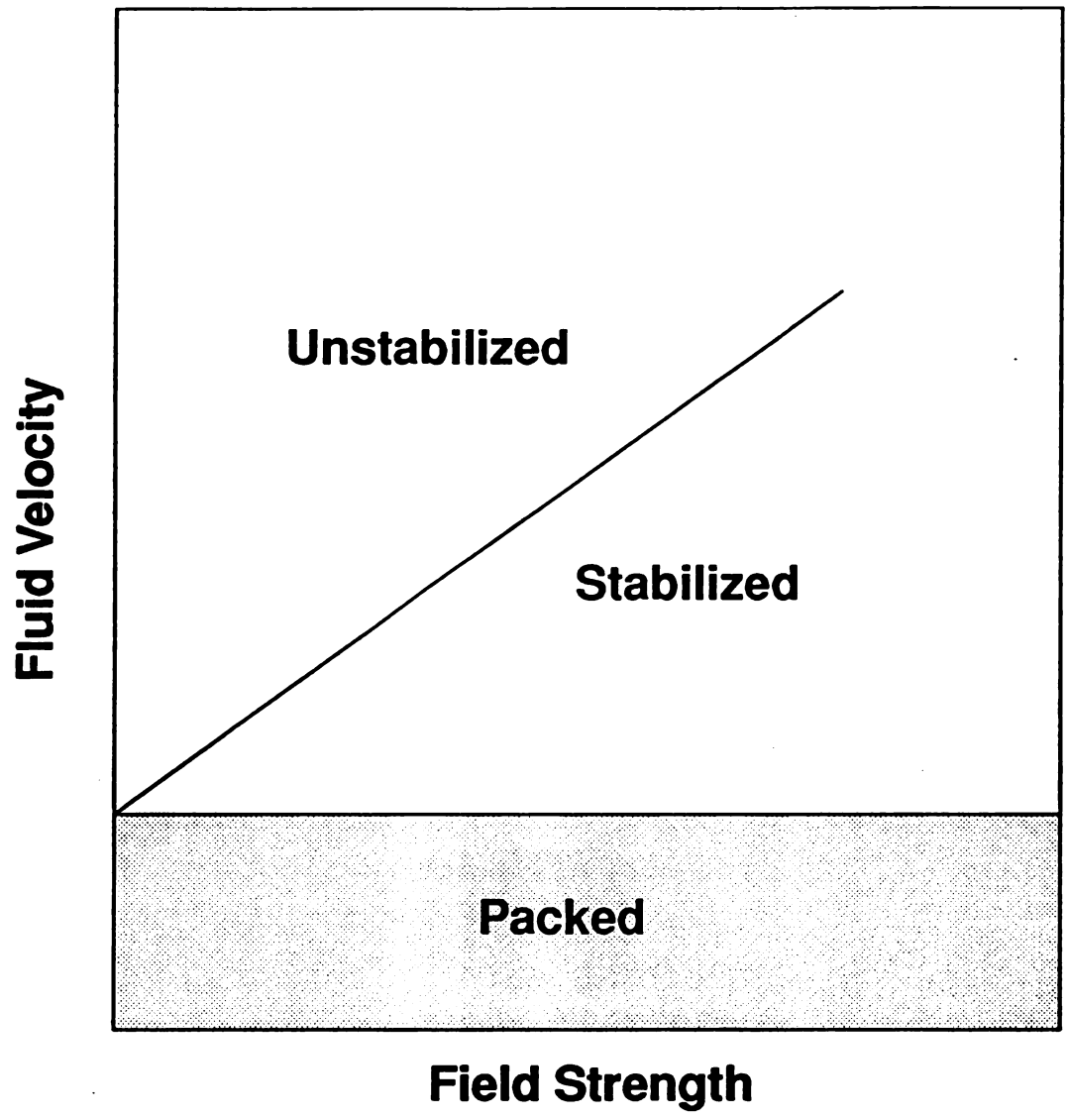

Figure 2-1 Phase Diagram for a Gas-Solid MSFB

bed divided by the cross-sectional area. At this point the bed was fluidized, and the pressure drop remained independent of the flow rate until the bed became unstable. The onset of instability was characterized by fluctuations in pressure drop.

Rosensweig also demonstrated the effects of field orientation on stabilization[8], showing that the transition to bubbling behavior occurred at much lower field strengths for a horizontal field than a vertical one. He demonstrated solids transport without solids mixing by placing bands of colored solids in the bed and removing them sequentially from the bed intact[9]. Later studies by Rosensweig[9] found radial dispersion of the gas to be greatly reduced in a magnetized system, and comparable to that of a packed bed. Heat transfer coefficients were found to be higher in the MSFB than in a packed bed indicating better gas-solid contacting.

Rosensweig established criteria for gas-solid bed stability[31] based on examination of the equations of motion combined with magnetic stresses as shown in Equations 2-1 to 2-5

$$N_m N_v > 1 \quad \textit{Unstable} \tag{2-1}$$

$$N_m N_v = 1 \quad \textit{Marginally Stable} \tag{2-2}$$

$$N_m N_v < 1 \quad \textit{Stable} \tag{2-3}$$

where N_m, the ratio of kinetic to magnetostatic energy, and N_v, the voidage modulus, are defined below:

$$N_m = \frac{\rho_p U^2}{M^2} \tag{2-4}$$

$$N_v = \frac{4\pi(3-2\varepsilon_g)^2}{\varepsilon_g^2(1-\varepsilon_g)}[1+(1-\varepsilon_g)\chi_o-(1-\varepsilon_g)(\chi_o-\hat{\chi}_o)]\cos^2\theta\frac{\cos^2\lambda}{\cos^2\theta} \tag{2-5}$$

In these equations, ρ_p is the particle density (g/mL), U is the superficial gas velocity (cm/s), M is the particle magnetization (gauss), ϵ_g is the void fraction of the bed, χ_o is the chord susceptibility, $\hat{\chi}_o$ is the differential susceptibility, λ is the angle between the magnetic field direction and the disturbance, and θ is the angle between the flow direction and the disturbance. This analysis also showed that magnetism produces an "elastic like restoring force"[31] against the growth of bubbles. Lee[32] examined rheological properties of the MSFB, and found that the MSFB is visco-plastic in behavior. Yield stresses measured in the bed were found to increase with increasing field strength. Solids settled more slowly in a magnetically stabilized bed than an unmagnetized system. Arnaldos *et al.*[33] looked at the effects of mixtures of magnetic and non-magnetic particles and determined that stabilization could be achieved with as low as 10% magnetic material present; however, the range of magnetic field strengths where bed stabilization occurrred was small at percentages lower than 30%. Arnaldos and Casal[34] found that mass transfer of water from humid air was more rapid in a MSFB than either an unmagnetized bed or a packed bed.

2.2.3 Liquid-Solid MSFB

The first recent studies of liquid-solid MSFB were performed in 1987 by Siegell[35] who used water-fluidized beds of steel and composite spheres. He noted four hydrodynamic regimes: packed, stable, roll-cell, and random. The stable regime is similar to that described for gas-solid systems and is characterized by no particle movement. The roll-cell regime is recognized by "gulf streaming", characterized by independent movement of areas of the bed, and the random regime is characterized by random solids movement. The flow regimes were controlled by the field strength, liquid velocity, and, to a lesser extent, the liquid distributor. Siegell also found the pressure drop profile to be independent of magnetic field strength. Axial dispersion in the liquid-solid MSFB was found to be almost identical to that of a packed bed. Graves and Goetz[36] also measured axial dispersion in a liquid-solid MSFB and found results comparable to Siegell. Siegell observed hysteresis in measurements of the bed fraction and bed pressure drop. With increasing liquid flow rate, the bed pressure drop increased linearly until fluidization was achieved and levelled off. As the flow rate was decreased, however, the bed pressure drop was lower than that measured at the same flow rate when the flow rate was increasing. The void fraction was consistently higher for decreasing flow rates than for the identical flow rate when the flow rate was increased. Burns and Graves[37] determined that liquid radial dispersion was much less in the MSFB than in an unmagnetized bed, but still 2-3 times higher than in a packed bed.

2.2.4 Gas-Liquid-Solid MSFB

There are few studies of gas-liquid-solid MSFB in the literature. The first, by Hu and Wu[38] appeared in 1987. Their system consisted of polyacrylamide gel beads containing Mn-Zn ferrite and fluidized by water and air. They reported bed regimes similar to those of Siegell. At low field strength, bed properties typical of an unmagnetized system were observed. At higher strengths, chains of beads formed and aligned with the field lines. At very high field strengths, the bed coalesced into a single mass. Only a slight variation (1%) in void fraction was found with field strengths from 0-500 gauss. Field strength also had little or no effect on radial distributions of gas holdup; however, there was a pronounced increase in solids holdup with the magnetic field due to bed contraction.

Kwauk *et al.*[39] studied bubble size in a three phase MSFB of iron particles fluidized by water and air and found a pronounced decrease in bubble size with increased field strength. They proposed a mechanism for bubble break up, shown schematically in Figure 2-2, in which field lines are "flexed" by a gas bubble. This "flexing" creates a magnetic force in the direction to restore the field lines to their original shape (*i.e.*, toward the center of the bubble). This force, in addition to the gravity and inertial forces of particles above the bubble, destabilize the bubble roof and lead to bubble disintegration. From a force balance on the bubble roof, they were able to calculate the maximum stable bubble size for each field strength. These values agreed quite well with the experimentally determined values.

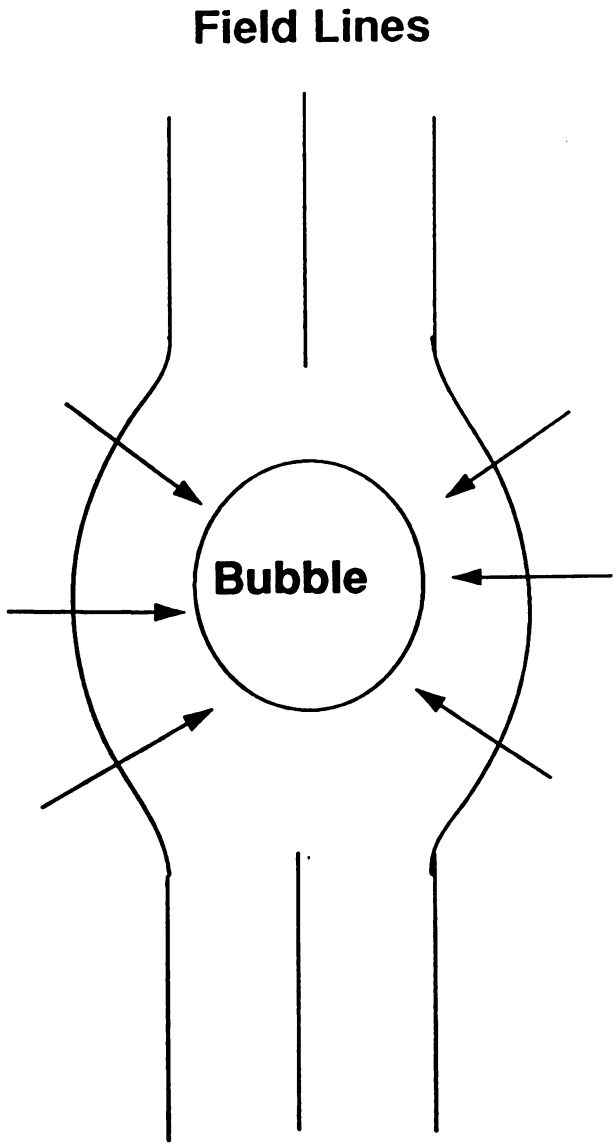

Figure 2-2 Magnetic Forces on a Bubble

2.2.5 Potential Applications of the MSFB

The capability of continuously contacting a dispersed solid phase with a fluid phase without mixing of the solid phase has led to several applications of the MSFB. One such application is filtration of fine particles. An MSFB using magnetite particles of 250-400 μm in diameter showed 99% efficiency in removal of fly-ash particles greater than 4 μm and 95% efficiency for particles less than 2.1 μm[8]. Other uses are the magnetic distributor-downcomer (MDD) , and the magnetic valve for solids (MVS)[40,41]. The MDD controls solids flow in a multistage process by turning on the current to a solenoid to freeze the solids in place and turning off the current to allow solids flow at prescribed intervals. The MVS is an on-off valve for solids flow in a pipe where the solids are frozen into place when the current in on and can move freely when it is off. A circulating magnetically stabilized bed reactor (CMSBR) has been proposed by Pirkle[44]. This reactor would approximate plug flow of both the solid and fluid phases, and computer simulations have shown that temperature profiles could be produced that would eliminate the need for heat exchangers or interstage cooling of reactants. The CMSBR could provide temperature profiles that would optimize reactor conversion in equilibrium-limited, exothermic reactions, and for highly exothermic reactions, the CMSBR is much less sensitive to temperature runaway than conventional reactors. Other uses for the MSFB are continuous adsorptive separation using molecular sieves[45,46]; continuous adsorptive separation for gas purification involving ethylene, cryogenic-plant gas, natural gas, and flue gas[47]; and adsorptive separations of hydrocarbon mixtures[48].

The liquid-solid MSFB has been demonstrated to be very effective in chromatographic separations[49-51]. The MSFB has also been demonstrated to work effectively as a bioreactor[38,52].

2.3 Phase Holdups

2.3.1 Definition and Theory

Volume fraction, also called holdup, is defined as the fraction of bed volume taken up by a particular phase. By definition, the phase holdups in a fluidized bed sum to one as shown in Equation 2-6

$$\varepsilon_s+\varepsilon_L+\varepsilon_g=1 \tag{2-6}$$

where ϵ_s is the solid fraction, ϵ_L is the liquid holdup, and ϵ_g is the gas holdup. Solid holdup can be easily calculated from the bed height, H (cm), and volume of solid particles present, V_p (mL), as shown in Equation 2-7

$$\varepsilon_s=\frac{V_p}{H_B A} \tag{2-7}$$

where A is the cross-sectional area of the bed (cm^2).

2.3.2 Measurement Techniques

Measurement of the static pressure profile of the column is commonly used to determine phase holdups. The differential force balance shown in Equation 2-8[53] relates the static pressure gradient (dP/dz), with units of $g/cm^2 \cdot s^2$, to the phase holdups

$$-\frac{dP}{dz}=(\rho_s\varepsilon_s+\rho_L\varepsilon_L+\rho_g\varepsilon_g)\frac{g}{g_c} \tag{2-8}$$

where ρ_s is the solid density (g/mL), ρ_L is the liquid density (g/mL),

ρ_g is the gas density, g is the acceleration due to gravity (cm/s^2), and g_c is the unit-conversion constant. By solving Equations 2-6 to 2-8 simultaneously, the three phase holdups can be calculated. Another method to measure gas holdup involves simultaneously shutting off the gas and liquid flow rates (the valve technique), and then measuring the distance which the liquid falls in cm (H_g) as the gas bubble escape. The gas holdup is then calculated by Equation 2-9[53,54]

$$\varepsilon_g = \frac{H_g}{H_B} \tag{2-9}$$

where H_B is the total column height (cm).

Tracer techniques[53] can be used to calculate the interstitial velocity of the gas or liquid phases between two points. The gas or liquid holdup is then calculated by Equation 2-10

$$\varepsilon = \frac{U}{U_i} \tag{2-10}$$

where U_i is the interstitial velocity (cm/s), and U is the superficial velocity of the gas or liquid phase calculated by Equation 2-11

$$U = \frac{F}{A} \tag{2-11}$$

where F is the volumetric flow rate (mL/s) of the gas or liquid phase.

Conductivity can be used to measure liquid holdup[55]. It has been found that the liquid holdup is proportional to the bed conductivity as shown in Equation 2-12

$$\varepsilon_L = \frac{\gamma}{\gamma_o} \tag{2-12}$$

where γ is the bed conductivity (ohm) and γ_o is the conductivity of the pure liquid (ohm).

Several optical probes have been described[56-59] that give different responses to gas and liquids. Gas holdup can then be calculated by

$$\varepsilon_g = \frac{t_g}{t} \tag{2-13}$$

where t_g (s) is the length of time the probe detects gas and t is the total time (s).

2.4 Liquid Mixing

2.4.1 Theory

Liquid mixing studies often use one of three common mixing models: well mixed, plug flow, and axially dispersed plug flow. A mass balance on a continuous-flow, well mixed liquid phase is shown in Equation 2-14[60]

$$F(C_o - C_L) = \frac{dC_L}{dt} \tag{2-14}$$

where C_o is the inlet concentration of solute in the liquid phase (g/mL), C_L is the effluent concentration of solute in the liquid phase (g/mL), F is the liquid flow rate (mL/s), and t is time (s).

The plug flow model is shown in Equation 2-15[60]

$$\frac{\partial C_L}{\partial t} = -U\frac{\partial C_L}{\partial z} \tag{2-15}$$

where z is the axial position in the column (cm).

The axial dispersion model is commonly used to describe liquid mixing in fluidized beds. This model is shown in Equation 2-16[61]

$$\frac{\partial C}{\partial t} = D_{ax}\frac{\partial^2 C}{\partial z^2} - U\frac{\partial C}{\partial z} \tag{2-16}$$

where D_{ax} is the axial dispersion coefficient (cm^2/s). This model is based on the assumption that fluid moves in plug flow with a dispersive mixing mechanism superimposed on it. This dispersive mixing mechanism is analogous to diffusion, but occurs on a macroscopic scale. The validity of this model has been challenged by Alvarez-Cuenca and Nerenberg[62] who divided the column into mixing zones, the grid and bulk, where the grid zone was characterized by complete mixing, and the bulk zone exhibited plug flow.

2.4.2 Experimental Methods to Measure Dispersion Coefficients

The axial dispersion coefficient can be measured by monitoring the progression of a tracer as it is carried through the bed by the fluid phase. Two types of tracer methods are commonly used: the one-shot method and the imperfect pulse method. In the one-shot method, a mathematically describable tracer profile is injected into the column, and its shape is measured at a position downstream. In the imperfect pulse method, an arbitrary tracer profile is injected into the column and then measured at two axial positions in the

column. The imperfect pulse method is easier experimentally, since producing a perfect mathematical pulse is difficult, but data analysis is more difficult. Commonly used tracers for both methods are salts[63], dyes[64], acids or bases[65], isotopes[66], and heat[67].

2.4.3 Data Analysis

Wakao and Kaguei[61] reviewed several techniques for determining dispersion coefficients from tracer concentration (C_{expt}) versus time data, and calculated errors associated with each method. In the moment method, the first and second moments of the input and response curves (M_1 and M_2, respectively) are calculated, and the dispersion coefficient and the interstitial velocity are then determined using Equation 2-17 and 2-18[61]

$$M_1^{II} - M_1^{I} = \frac{L}{U} \tag{2-17}$$

$$M_2^{II} - (M_1^{II})^2 - M_2^{I} - (M_1^{I})^2 = \frac{2D_{ax}L}{U^3} \tag{2-18}$$

where the superscripts I and II refer to the input and response curves respectively, and L is the distance between the two measuring points (cm). The n^{th} moment of the tracer data is defined by Equation 2-19[61]

$$M_n = \frac{\int_0^\infty C_{expt} t^n dt}{\int_0^\infty C_{expt} dt} \tag{2-19}$$

The shortcoming of this method is that the tail portion of the curves are weighted heavily by the t^n factor especially for the higher

moments. Thus, measurement errors in the tail portion of the curve are magnified.

The weighted moment method reduces this sensitivity to tailing errors by using a weighting factor exp(-st) that approaches zero both at short and long times. The n^{th} weighted moment is then defined by Equation 2-20[68]

$$m_n^* = \frac{\int_0^\infty C_{exp} t^n e^{-st} dt}{\int_0^\infty C_{exp} dt} \tag{2-20}$$

The transfer function, F(s), of Equation 2-16 describes the relationship between the input and response curves in the Laplace domain. The transfer function is related to the moments as shown in Equations 2-21 and 2-22

$$\frac{m_0^{*II}}{m_0^{*I}} = F(s) \tag{2-21}$$

$$\frac{m_1^{*II}}{m_0^{*II}} - \frac{m_1^{*I}}{m_0^{*I}} = \frac{F'(s)}{F(s)} \tag{2-22}$$

where F(s) and F'(s)/F(s) are defined in Equations 2-23 and 2-24

$$F(s) = \exp\left(\frac{LU}{2D_{ax}}\left[1-(1+4\frac{D_{ax}}{U^2}s)\right]^{\frac{1}{2}}\right) \tag{2-23}$$

$$\frac{F'(s)}{F(s)} = -\frac{L}{U}(1+4\frac{D_{ax}}{U^2}s)^{-\frac{1}{2}} \tag{2-24}$$

The difficulty with this method lies in choosing the optimal s value

to use. The optimal s value may also be different for each moment calculated. Equation 2-25 gives suggested values of s to use[69]

$$s=\frac{n_{highest}}{t_{max\ input}+t_{max\ response}-\Delta t_D} \tag{2-25}$$

where $n_{highest}$ is the higher order moment used in the parameter estimation, Δt_D is the time delay between the input and response curves, and $t_{max\ input}$ and $t_{max\ response}$ are the times when the input and response curves have maximum values, respectively.

The transfer-function-fitting method used Equation 2-26 or 2-27[68].

$$-\{\ln[F(s)]\}^{-1}=\frac{L}{U}s\{\ln[F(s)]\}^{-2}-\frac{LU}{D_{ax}} \tag{2-26}$$

$$\left[\frac{F'(s)}{F(s)}\right]^{-2}=\frac{4U^2}{D_{ax}}s+\left(\frac{L}{U}\right)^{-2} \tag{2-27}$$

In this method either $-\{\ln[F(s)]\}^{-1}$ is plotted versus $s\{\ln[F(s)]\}^{-2}$ or $(F'(s)/F(s))^{-2}$ is plotted versus s, and the slope and intercept yield the desired parameters. However, this method also requires a somewhat arbitrary selection of the optimal s value to use. A range of $2 \leq sL/U \leq 5$ has been recommended[70].

Fourier analysis[71] has also been applied to estimation of D_{ax} and U_i. In this method the input and response signals are assumed to be composed of harmonic components. This analysis evaluates the decay in the amplitude and phase shift of these harmonic components between the input and response curves. Equations 2-28 and 2-29 are

used to convert the experimental data into amplitude and phase shift description.

$$a_\omega = \int_0^\infty C_{expt} \cos(\omega t) dt \tag{2-28}$$

$$b_\omega = \int_0^\infty C_{expt} \sin(\omega t) dt \tag{2-29}$$

Equation 2-30 then relates the phase shifts and amplitudes of the experimental data into a single relationship similar to the transfer function of the previous methods.

$$R_\omega + iI_\omega = \frac{a_\omega^{II} - ib_\omega^{II}}{a_\omega^{I} - ib_\omega^{I}} \tag{2-30}$$

Equations 2-31 to 2-34 define the amplitude, R_ω, and the phase shift, I_ω, in terms of the desired parameters.

$$R_\omega = \exp[\frac{2LU}{D_{ax}} - x \cos y] \cos[x \sin y] \tag{2-31}$$

$$I_\omega = -\exp[\frac{2LU}{D_{ax}} - x \cos y] \sin[x \sin y] \tag{2-32}$$

$$x = [(\frac{LU}{2D_{ax}})^4 + (\frac{L^2\omega}{D_{ax}})^2]^{\frac{1}{4}} \tag{2-33}$$

$$y = \frac{1}{2}\tan^{-1}(\frac{4D_{ax}}{U^2}\omega) \tag{2-34}$$

In the time-domain curve fitting method[61], the input signal is expressed as a Fourier series[61]:

$$C^{I}_{expt}(t)=\frac{a_0}{2}+\sum_{n=1}^{\infty}\left(a_n\cos\left(\frac{n\pi t}{\tau}\right)+b_n\sin\left(\frac{n\pi t}{\tau}\right)\right) \tag{2-35}$$

$$a_n=\frac{1}{\tau}\int_0^{2\tau}C^{I}_{expt}\cos\left(\frac{n\pi t}{\tau}\right)dt \tag{2-36}$$

$$b_n=\frac{1}{\tau}\int_0^{2\tau}C^{I}_{expt}\sin\left(\frac{n\pi t}{\tau}\right)dt \tag{2-37}$$

where 2τ is the period of time required for the tail of the response curve to disappear. The theoretical Fourier coefficients for the response curve can be calculated from Equation 2-38

$$a_n^{*}-ib_n^{*}=(a_n-ib_n)F\left(\frac{in\pi}{\tau}\right) \tag{2-38}$$

where $F(in\pi/\tau)$ is described by Equation 2-23 with s replaced by $in\pi/\tau$. Similarly, the experimental response curve can also be expressed as a Fourier series in Equation 2-39 to 2-41

$$C^{II}_{expt}=\frac{a_0^{*}}{2}+\sum_{n=1}^{\infty}\left(a_n^{*}\cos\left(\frac{n\pi t}{\tau}\right)+b_n^{*}\sin\left(\frac{n\pi t}{\tau}\right)\right) \tag{2-39}$$

$$a_n^{*}=\frac{1}{\tau}\int_0^{2\tau}C^{II}_{expt}\cos\left(\frac{n\pi t}{\tau}\right)dt \tag{2-40}$$

$$b_n^{*}=\frac{1}{\tau}\int_0^{2\tau}C^{II}_{expt}\sin\left(\frac{n\pi t}{\tau}\right)dt \tag{2-41}$$

In this technique D_{ax} and U_i are varied until the root-mean-square error between the calculated and experimental curves is minimized. The root-mean-square error is calculated as

$$\varepsilon=\left\{\frac{2(\frac{a_0^*-a_0^+}{2})^2+\sum_{n=1}^{\infty}[(a_n^*-a_n^+)^2+(b_n^*-b_n^+)^2]}{2(\frac{a_0^*}{2})^2+\sum_{n=1}^{\infty}(a_n^{*2}+b_n^{*2})}\right\} \tag{2-42}$$

Wakao and Kaguei[61] examined each method, and found the time-domain curve fitting method to give the best estimate of the parameters with the Fourier analysis a close second. The worst technique was the moment method with the weighted moment and the transfer function methods intermediate between the two in error.

2.4.4 Interaction of the Tracer with the Solid Phase

In axial dispersion studies, it is conventional to neglect interactions between the tracer molecules and the solid phase, such as adsorption of the tracer onto the solid and diffusion of the tracer into the solid. In the commonly used system of air, water, and glass beads using salts as tracer, these assumptions are usually valid. However, when a tracer adsorbing or porous solid phase is used, one or more of these assumptions may be invalid. Wakao and Kaguei[61] developed an analysis for use in chromatography that includes the effects of adsorption, diffusion, and film mass transfer. The model is shown in Equations 2-43 to 2-46

$$\frac{\partial C_L}{\partial t}=D_{ax}\frac{\partial^2 C_L}{\partial z^2}-U_i\frac{\partial C_L}{\partial z}-\frac{3\varepsilon_p(1-\varepsilon_L)D_e}{R\varepsilon_L}(\frac{\partial C_B}{\partial r})_R \tag{2-43}$$

$$\frac{\partial C_B}{\partial t}=D_e\frac{1}{r^2}\frac{\partial}{\partial r}(r^2\frac{\partial C_B}{\partial r})-\rho_p\frac{\partial C_{ad}}{\partial t} \tag{2-44}$$

$$D_e\frac{\partial C_B}{\partial r}=k_f(C_L-C_B) \tag{2-45}$$

$$\frac{\partial C_{ad}}{\partial t}=k_a(C_B-\frac{C_{ad}}{K_a}) \tag{2-46}$$

where C_B is the tracer concentration in the intraparticle pore volume (g/mL), ϵ_p is the particle porosity, R is the particle radius (cm), r is the radial position in the particle (cm), D_e is the diffusion coefficient (cm^2/s), ρ_p is the particle density (g/mL), C_{ad} is the amount adsorbed on the particle (g/mL), k_f is the film mass transfer coefficient (cm/s), k_a is the adsorption rate constant (s^{-1}), and K_a is the adsorption equilibrium constant. Equation 2-43 is a mass balance on the tracer in the liquid phase, Equation 2-44 is a mass balance on the tracer in the liquid phase of the solid, Equation 2-45 describes transfer of tracer across a liquid film around the solid phase, and Equation 2-46 describes the rate of adsorption of the tracer to the solid phase.

The transfer function for this set of equations is shown in Equations 2-47 to 2-50

$$F(s)=\exp\left[\frac{1}{2}(\frac{LU_i}{D_{ax}}-\hat{\sigma}_B)\right] \tag{2-47}$$

$$\hat{\sigma}_B=\frac{LU_i}{D_{ax}}\left[1+\frac{4D_{ax}}{U_i^2}(s+q)\right]^{\frac{1}{2}} \tag{2-48}$$

$$q=\frac{D_e 3(1-\varepsilon_L)}{\varepsilon_L R^2}\frac{1}{\frac{D_e}{k_f R}+\frac{1}{\phi_a \coth(\phi_a)-1}} \tag{2-49}$$

$$\phi_a=R\left[\frac{s}{D_e}\left(\varepsilon_p+\frac{\rho_p k_a K_a}{K_a s+k_a}\right)\right]^{\frac{1}{2}} \tag{2-50}$$

The techniques discussed in Section 2.4.2 to determine parameters from experimental data are also valid for Equations 2-43 to 2-50. Parameter estimation for this model is also discussed by Wakao and Kaguei[61].

2.5 Gas-to-Liquid Mass Transfer

2.5.1 Theory

There are several potentially rate-limiting mass transfer steps in three phase fluidized beds: gas-to-liquid, liquid-to-solid, and possibly gas-to-solid. The gas-to-liquid mass transfer step is generally rate-limiting when sparingly soluble gases like oxygen are used, and is consequently the most studied. The flux of a gas from the bulk gas phase to the liquid phase can be described using either gas-phase or liquid-phase mass transfer coefficients[60]:

$$flux=k_g(C_g-C_{gi})=k_L(C_{Li}-C_L) \tag{2-51}$$

where C_g is the concentration in the bulk gas (g/mL), C_L is the concentration of dissolved gas in the bulk liquid (g/mL), C_{gi} is the concentration of gas at the gas-liquid interface (g/mL), C_{Li} is the concentration of dissolved gas at the liquid-gas interface (g/mL), k_g is the gas-phase mass transfer coefficient (cm/s), and k_L is the liquid-phase mass transfer coefficient (cm/s). Since it is difficult to

experimentally measure the interfacial concentrations, the mass tranfer expression is rewritten in terms of an overall mass transfer coefficient and a measurable, overall concentration driving force as shown in Equation 2-52[60]

$$flux = K_L(C_L^* - C_L) \tag{2-52}$$

where K_L is the overall mass transfer coefficient (cm/s), and C_L^* is the liquid phase concentration which is in equilibrium with the gas phase (g/mL). Henry's law is commonly used to calculate C_L^* for sparingly soluble gases[60]:

$$HC_L^* = C_g \tag{2-53}$$

where H is the Henry's law constant. An expression relating the overall mass transfer coefficient to the gas and liquid phase mass transfer coefficients can be developed from Equations 2-51 to 2-53

$$\frac{1}{K_L} = \frac{1}{k_L} + \frac{1}{Hk_g} \tag{2-54}$$

However, for gases which are sparingly soluble, such as oxygen, H is large, and k_g is considerably larger than k_L; therefore, K_L is approximately equal to k_L. The rate of gas mass transfer per unit bed volume, Q, can then be defined as

$$Q \approx k_L(C_L^* - C_L)\frac{A}{V} \approx k_L a(C_L^* - C_L) \tag{2-55}$$

where A/V, or a, is the gas-liquid interfacial area per unit liquid volume.

2.5.2 Measurement Techniques for k_La

2.5.2.1 Dynamic Method

In the dynamic method, unsteady-state oxygen concentration data are compared to an appropriate mathematical model to determine k_La. The data are obtained by sparging a degassed liquid with the gas of interest while using a probe to monitor the change in gas concentration with time. A mass balance on the gas dissolved in the liquid phase of a well-mixed reservoir is shown in Equation 2-56

$$F(C_0-C_L)+k_La V_L(C_L^*-C_L)=V_L\frac{dC_L}{dt} \tag{2-56}$$

where F is the liquid flow rate (mL/s), C_o and C_L are the inlet and outlet dissolved gas concentrations, respectively, and V_L is the liquid volume. Equation 2-56 is derived in Appendix A.1 using several assumptions: the concentration change in the gas phase is negligible, the pressure in the system is constant, and the liquid-phase mass transfer resistance is rate controlling. When the liquid is free of dissolved gas, the appropriate solution is shown in Equation 2-57 which is derived in Appendix A.1.

$$C_L(t)=\frac{\frac{FC_o}{V_L}+k_La C_L^*}{\frac{F}{V_L}+k_La}\left[1-e^{-(\frac{F}{V_L}+k_La)}\right] \tag{2-57}$$

Problems with this method arise when the time constant of the probe response, which is defined as the time it takes the probe to achieve 63.2% of its steady state response following a step input, is not much smaller than $1/k_La$. Under these conditions, the probes' output lags behind the actual change in concentration. The time

constant of the probe is controlled by the rate of gas diffusion to the probe surface through a stagnant liquid layer and diffusion through the probe membrane. A first order dynamic model of a probe is shown in Equation 2-58[72]

$$\frac{dP_E}{dt}=\frac{C_L H-P_E}{\tau_E} \tag{2-58}$$

where P_E is the partial pressure of gas at the electrode and τ_E is the time constant of the probe. Other more complex probe models also have been proposed[73-76]. Van't Riet[77] has shown that the probe dynamics can be ignored if the response time of the probe is less than about 2 seconds.

Another source of error in this type of measurement arises from neglecting changes in the gas phase composition especially when the gas used is highly soluble or when long bubble residence times are used. The well-mixed model for the gas phase is shown in Equation 2-59[72]

$$\frac{d(V_g C_g)}{dt}=F_g(C_{go}-C_g)-k_L a V_L(C_L^*-C_L) \tag{2-59}$$

where V_g is the gas volume (mL), C_{go} is the inlet gas concentration (g/mL), and F_g is the gas flow rate (mL/s). Van't Riet[77] has determined that the gas-phase dynamics can be ignored when the gas phase residence time is much smaller than $1/k_L a$. Equations 2-57 to 2-59 are commonly used in stirred tank systems, where the assumption of complete liquid mixing is usually valid. However, this assumption may not be valid for fluidized-bed systems unless

recycle is used or there is a high degree of agitation. The dynamic method is not generally used for other mixing models, such as the plug flow or dispersed plug flow because of the difficulty of solution.

2.5.2.2 Steady State Method

In the steady-state method, both degassed liquid and gas are fed continuously to the reactor until steady-state is achieved. The gas concentration of the liquid phase is then measured at one or more locations in the reactor. The well mixed model for this method is shown in Equation 2-60 and derived in Appendix A.2

$$F(C_o - C_L) + k_L a V_L (C_L^* - C_L) = 0 \qquad (2\text{-}60)$$

Using this equation $k_L a$ can be calculated directly from the inlet and outlet dissolved gas concentrations.

The plug flow model is shown in Equation 2-61

$$-U\frac{\partial C_L}{\partial z} + k_L a (C_L^* - C_L) = \varepsilon_L \frac{\partial C_L}{\partial t} \qquad (2\text{-}61)$$

When the dissolved gas concentration at the reactor inlet is zero, the following solution is

$$C_L(z) = C_L^* \left(1 - e^{-\left(\frac{k_L a}{U} z\right)}\right) \qquad (2\text{-}62)$$

Equations 2-61 and 2-62 are derived in Appendix A.3. Experimentally measured gas concentration profiles can be fit to Equation 2-62 using non-linear regression techniques.

The dispersed plug flow model is shown in Equation 2-63

$$D_{ax}\varepsilon_L\frac{\partial^2 C_L}{\partial z^2}-U\frac{\partial C_L}{\partial z}+k_L a(C_L^*-C_L)=\varepsilon_L\frac{\partial C_L}{\partial t} \tag{2-63}$$

The following the boundary conditions are used with this differential equation

$$\begin{aligned} z=0 \qquad & C_L=C_o+\frac{D_{ax}}{U}\frac{dC_L}{dz} \\ z=L \qquad & \frac{dC_L}{dz} \end{aligned} \tag{2-64}$$

The significance of the first boundary condition is discussed by Eroglu and Dogu[78]. The solution to Equations 2-63 with boundary conditions of Equation 2-64 is given in Equations 2-65 to 2-68

$$C_L=A_1e^{n_1z}+A_2e^{n_2z}+C_L^* \tag{2-65}$$

$$n_{1,2}=\frac{U}{2D_{ax}}\left(1\pm\sqrt{1+\frac{4k_LaD_{ax}}{U^2}}\right) \tag{2-66}$$

$$A_1=\frac{(C_L^*-C_o)n_2e^{n_2}}{n_1^2e^{n_1}-n_2^2e^{n_2}} \tag{2-67}$$

$$A_2=\frac{-(C_L^*-C_o)n_1e^{n_1}}{n_1^2e^{n_1}-n_2^2e^{n_2}} \tag{2-68}$$

Equation 2-63 and its solution are derived in Appendix A.4.

Another method introduced by Alvarez-Cuenca and Nerenberg[61]

combines the well mixed and the plug flow models by assuming that the bottom of the column near the gas sparger is well mixed, while the top of the column is in plug flow. These models do not account for changes in gas phase concentration, changes in system pressure, and changes in the physical properties along the length of the reactor.

Deckwer *et al.*[79] included an equation to describe the change in static system pressure along the column.

$$P=P_T[1+\alpha(1-\frac{z}{L})] \tag{2-69}$$

$$\alpha=\frac{(\rho_g\varepsilon_g+\rho_L\varepsilon_L+\rho_s\varepsilon_s)gL}{P_T} \tag{2-70}$$

The pressure variation along the column in turn affects the equilibrium concentration of dissolved gas, C_L^*, as shown below:

$$C_L^*=\frac{Px_{O_2}}{H} \tag{2-71}$$

where x_{O2} is the mole fraction in the gas phase.

Tang and Fan[80] determined that phase holdups are not constant along the length of the column, particularly for light particle systems, and used an empirical equation to describe this effect. If the concentration of the gas phase changes significantly across the column, this effect must also be considered, as described in Section 2.5.2.1.

Chapter III: Materials and Methods

3.1 Fluidized Bed

3.1.1 Construction

The reactor, shown schematically in Figure 3-1, consisted of two pieces of glass pipe 5 cm in diameters that were joined by a threaded fitting. The top piece was 81 cm long and had four 5 mm ports placed at 15 cm intervals for probe access. The top of the column utilized a liquid-overflow system to allow disengagement of the gas and liquid phases. The bottom piece was 26 cm in length and contained the gas sparger; it also served as a calming region to reduce turbulence at the entrance. Ten mesh wire screen was placed just below the gas sparger to support the solid particles in the bed. The two pieces were connected by a threaded nylon cylinder the same diameter as the column and O-rings were used to seal the joints. This configuration was designed to facilitate interchange of different types of gas spargers.

3.1.2 Liquid Phase

The reverse osmosis (RO) water used in all studies was pumped from a holding tank by a 1.5 horsepower centrifugal pump (Dayton Electric, Chicago IL) capable of delivering 220 mL/s through this system. The water was metered with a rotameter into the bottom of the column through a 9 mm tube and entered the 26 cm long calming region. Upon exiting the top of the column, the water was returned to the 55 gallon holding tank. Liquid flowrates of 101, 126, and 148 mL/s were used in this study.

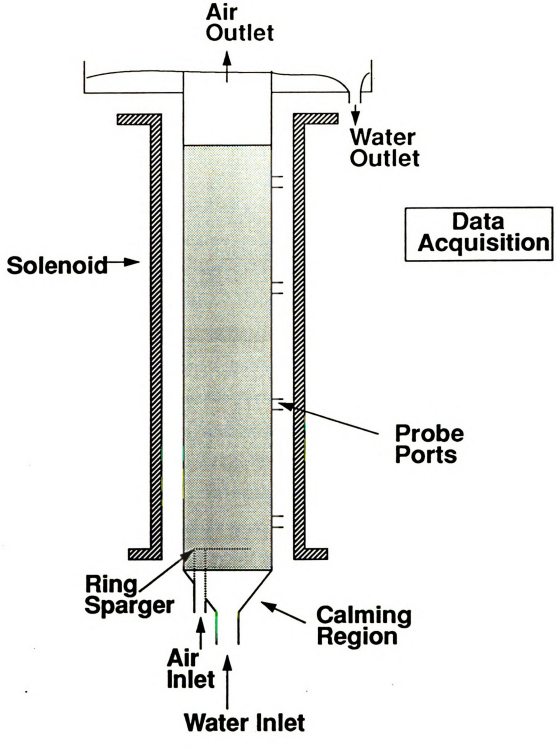

Figure 3-1 Schematic of experimental apparatus.

3.1.3 Gas Phase

Compressed air was metered into the column with a rotameter. It was sparged through a stainless steel ring 3.5 cm in diameter with 0.2 mm holes spaced at 5 mm intervals around the ring. Gas flow rates used in this study (measured at 25°C and a one atmosphere pressure) were 11.8, 21.6, and 39.2 cm^3/s.

3.1.4 Solid Phase

The solid phase consisted of 4 mm composite beads made from a calcium alginate and powdered magnetite (Fe_3O_4). The beads were produced by mixing equal weights of two percent by weight, aqueous, low viscosity sodium alginate (Sigma, St. Louis MO) and magnetite powder (Aldrich, Milwaukee WI). The resulting mixture was dripped through a 3 mm tube into a solution of 0.2 M calcium chloride and allowed to harden for 48 hours. To prevent leakage of magnetite, the beads were then coated with an additional layer of alginate. The coating procedure involved blotting excess water from the beads' surfaces. then shaking the beads in a plastic bag containing sodium alginate powder. After shaking off excess powder, the beads were placed on wax paper for 15 minutes to allow partial dissolution of the sodium alginate powder with water from bead pores. The beads were then cured in 0.2 M calcium chloride for 48 hours, and washed twenty times with a volume of RO water equal to twice the bead volume to remove the excess calcium chloride before being stored in RO water.

3.2 Solenoid

3.2.1 Design

The design equations for a finite solenoid are shown in Equations 3-1 to 3-3[81].

$$H_z(z,0)=H_o\frac{a^3}{(a^2+z^2)^{3/2}} \tag{3-1}$$

$$H_o=\frac{NI}{a_1}\frac{1}{2\beta Hxlpha-1)}F(\alpha,\beta) \tag{x3-2}$$

$$F(\alpha,\beta)=\frac{4\pi\beta}{10}\ln\left[\frac{\alpha+(\alpha^2+\beta^2)^{1/2}}{1+(1+\beta^2)^{1/2}}\right] \tag{3-3}$$

z is the axial position (cm), $H_z(z,0)$ (gauss) is the field strength along the center line of the solenoid, H_o (gauss) is the maximum field strength, $F(\alpha,\beta)$ is the field factor, N is the number of turns of wire, I (amps) is the current, the parameters a_1, α, and β are defined in Figure 3-2 and a (cm) is the average of a_1 and a_2. The solenoid length and diameter, length of wire, the current, and power comsumption had to be specified in the design. The solenoid length was limited to approximately 80 cm, due to the size of the fluidized bed column. The solenoid inner diameter had to be at least 6.5 cm to accomodate the fluidized bed. A maximum field strength of 300 gauss was chosen based on previous results[38]. Then, based on simulations using Equations 3-1 to 3-3, values for the current, power consumption, and wire length were chosen to be 5 amps, 350 watts, and 1000 meters respectively. The computer programs used in these simulations are listed in Appendix B. These chosen values were somewhat arbitrary, since several combinations of current and wire

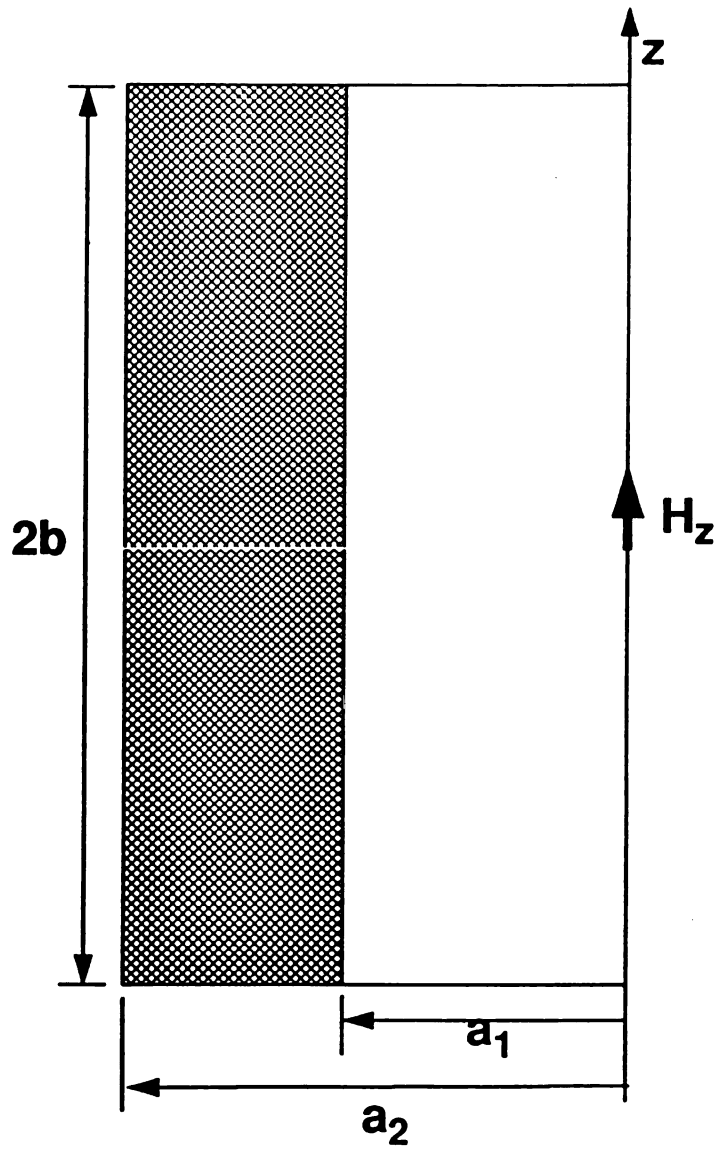

a_1 is the inner radius of the solenoid
a_2 is the outer radius including wire
2b is the length of the solenoid

$\alpha = a_2/a_1$
$\beta = b/a_1$

Solenoid Wire

Figure 3-2 Solenoid parameters

length would have given a field strength of 300 gauss. When examining commercially available power supplies, one was found capable of producing 5 amps and 350 watts, so that particular set of parameters was chosen. The solenoid was designed with an internal water jacket as described below, to remove excess heat.

3.2.2 Construction

A cross-section of the solenoid is shown schematically in Figure 3-3. The solenoid consisted of 1000 m of 17 gauge coated copper wire (MWS Wire Industries, Westlake Village CA) wrapped around an 82 cm long copper cylinder having a 10 cm outer diameter and 0.25 cm wall thickness. Inside this cylinder was a second, concentric copper cylinder having a 7.5 cm outer diameter and wall thickness of 0.25 cm. The cylinders were held in place with two square Teflon endpieces that were secured by four aluminum rods, one in each corner of the Teflon piece. Fittings were mounted into the Teflon endpieces to allow flow of cooling water through the annular region between the two cylinders. Power for the solenoid was provided by a 100 volt, 5 amp D.C. power supply (Kepco, Flushing NY). This unit provided magnetic field strengths from 0-300 gauss, as measured by a Gaussmeter (Magnetic Instrumentation Inc., Indianapolis IN). Tap water at approximately 10°C was pumped through the solenoid to remove the heat generated.

3.3 Gas Void Fraction

3.3.1 Probe construction

Gas void fraction was measured using a fiber-optic probe[43-46], shown schematically in Figure 3-4. The probe was constructed by bending an acrylic optical fiber (Edmund Scientific, Barrington NJ)

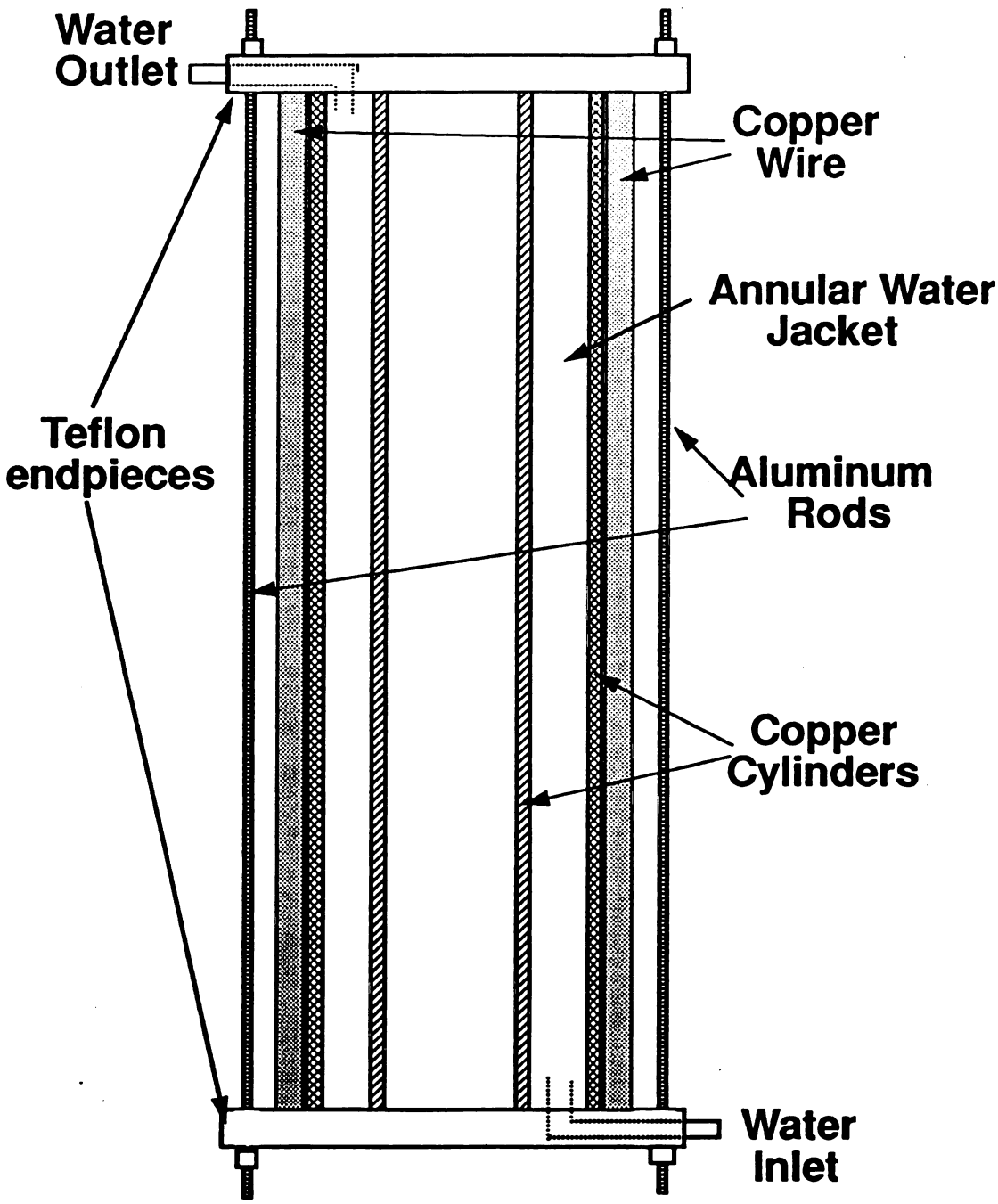

Figure 3-3 Schematic of solenoid cross-section.

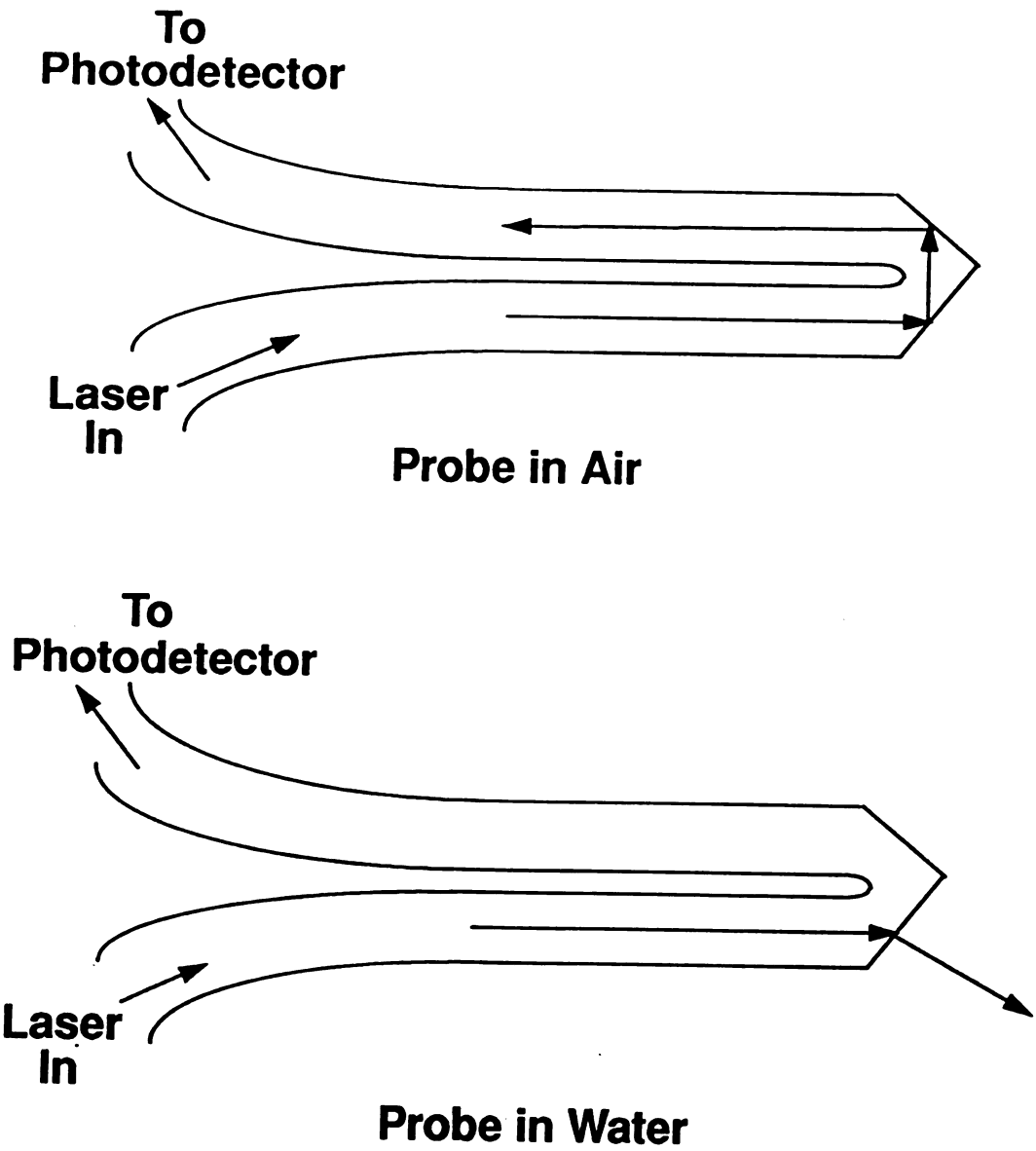

Figure 3-4 Schematic of gas void fraction probe

250 microns in diameter into a U shape and pulling the ends through a stainless steel tube 570 microns in diameter and 2.5 cm long until approximately 1 mm of the U remained outside the tube. The probe tip was then ground with 1 micron grit aluminum oxide paper to form a 90° included angle. Monochromatic light from a HeNe laser (Newport Corporation, Fountain Valley CA) was focused onto one end of the fiber with a microscope lens. A silicon photodetector (Newport Corporation) measured the light from the emitted from the other end. The operation of the probe is based on Snell's Law[45], which can be applied at the interface between the probe and the fluid:

$$n \sin(i) = n_o \sin(i_o) \qquad (3\text{-}4)$$

where n_o is the refractive index of the probe, i_o is the angle of incidence, n is the refractive index of the medium surrounding the probe, and i is the angle of refraction. For the fiber used, n_o= 1.495, and for the probe geometry shown in Figure 3-4, i_o = 45°. Thus, when n is less than 1.06, the light rays should be reflected back into the probe, and when n is greater than 1.06, the light should be reflected out of the probe. Water and air have refractive indices of 1.33 and 1.00 respectively, and can thus be discriminated by the probe.

3.3.2 Calibration and Data Analysis

The probe tip was centered radially at an axial position 45 cm above the gas sparger in a horizontal position. The photodetector output was sampled by a data acquisition system (Labtech Notebook, Wilmington VA) at 200 Hz for 45 seconds for each void fraction

determination, and five replicates were measured for each set of conditions.

The gas void fraction was calculated as the time the probe spent in the gas phase divided by the total time. The time in the gas phase was taken to be the sum of the peak widths. However, as shown in Figure 3-5, some of the peaks are triangular, and the correct width to use (W, cm) is not clear. The appropriate width was determined by calibrating the probe. Figure 3-6 shows the calibration apparatus. Liquid was metered into a 3 mm inner diameter vertical tube with two optical fiber probes spaced 6.5 cm apart, and a bubble was injected at the bottom of the tube. Due to the small diameter of the tube, the bubble filled the entire cross-section, so the probe could not miss the bubble. A 35 mm camera was used to take a picture of each bubble, and a ruler was placed next to the tube to provide a scale for the bubble length. The cross-correlation function of the two signals was calculated as follows:[82]

$$R_{xy}(\tau)=\frac{1}{T}\int_0^T x(t)y(t+\tau)dt \qquad (3\text{-}5)$$

where $R_{xy}(\tau)$ is the cross-correlation function, x is the signal from the first probe, y is the signal from the second probe, and T (sec) is the total time. The value of τ that maximizes R_{xy}, designated τ_{max}, is the time the bubble requires to travel between the two probes. The bubble velocity, U_B (cm/s), was then calculated from Equation 3-6.

$$U_B=\frac{6.5}{\tau_{max}} \qquad (3\text{-}6)$$

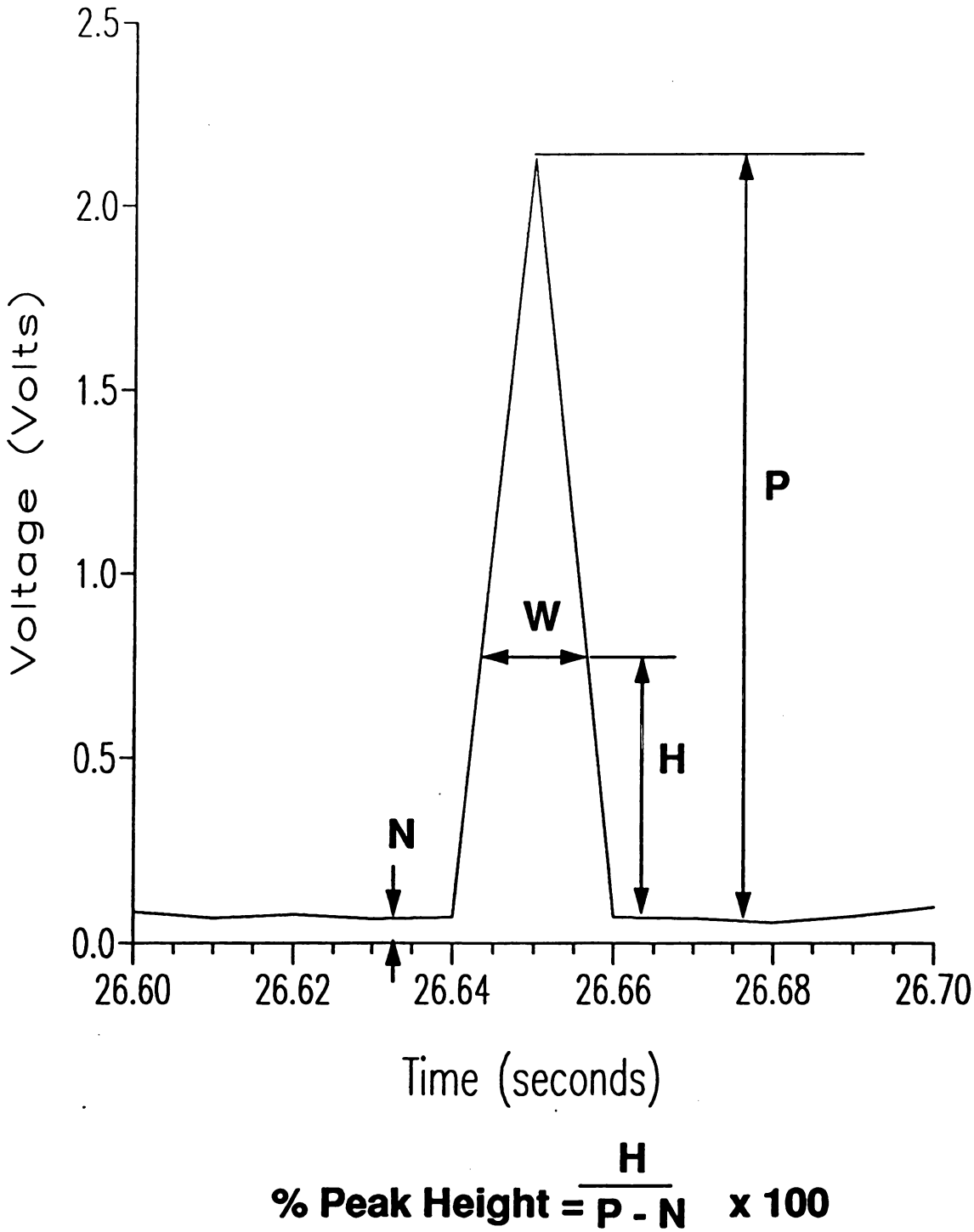

Figure 3-5 Experimental Data from One Bubble

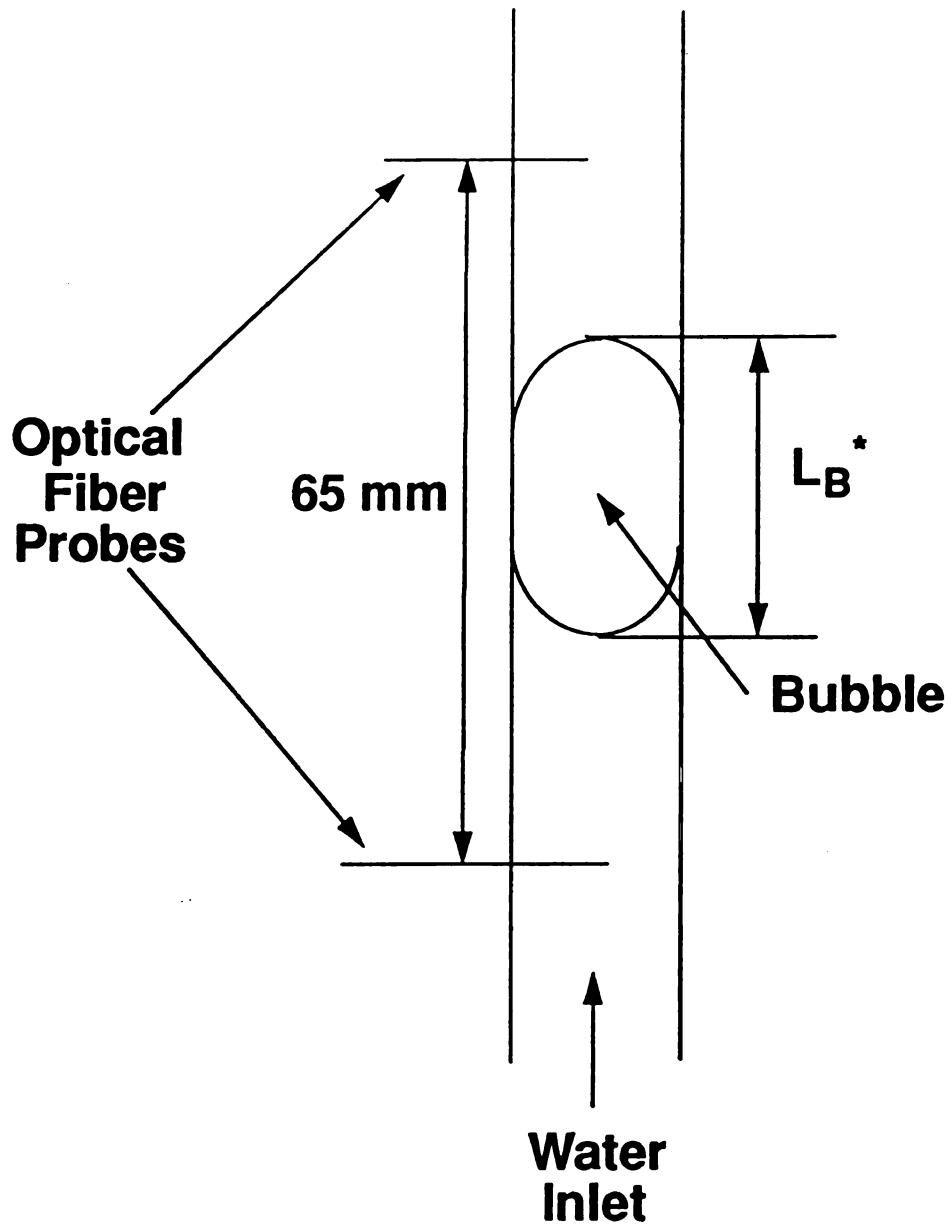

* Not Drawn to Scale

Figure 3-6 Calibration Apparatus for Optical Probe

The bubble length, L_B (cm), was measured from the photo of the bubble, and the time the bubble required to travel across the probe, t_B (sec), was calculated from this length and the bubble velocity using Equation 3-7.

$$t_B = \frac{L_B}{U_B} \tag{3-7}$$

The appropriate width of the probe signal was then determined, as a percent of the peak height as shown in Figure 3-5. A value of 10% was found to be optimal for all the liquid velocities used in this study. The computer program used to calculate void fraction from experimental data is listed in Appendix B. Measurements of gas void fraction using the valve technique (Section 2.3.2) were also conducted to determine how the local gas void fraction compared with the averaged gas void fraction.

3.4 Liquid Phase Dispersion

Liquid-phase dispersion coefficients were determined using the imperfect pulse method. In this method a pulse of tracer is injected at the bottom of the column, and its progress is followed by probes at two different axial positions in the column. For this study, a calcium chloride tracer and conductivity probes were used.

3.4.1 Probe Construction and Calibration

The conductivity probes were constructed by placing a 1 mm diameter brass rod inside a 2 mm I.D. brass tube with a 0.5 mm thick plastic non-conducting spacer in between, as shown in Figure 3-7. The tip of the probe was ground flat with emery paper. Wires were soldered to the inner rod and the outer cylinder and then connected

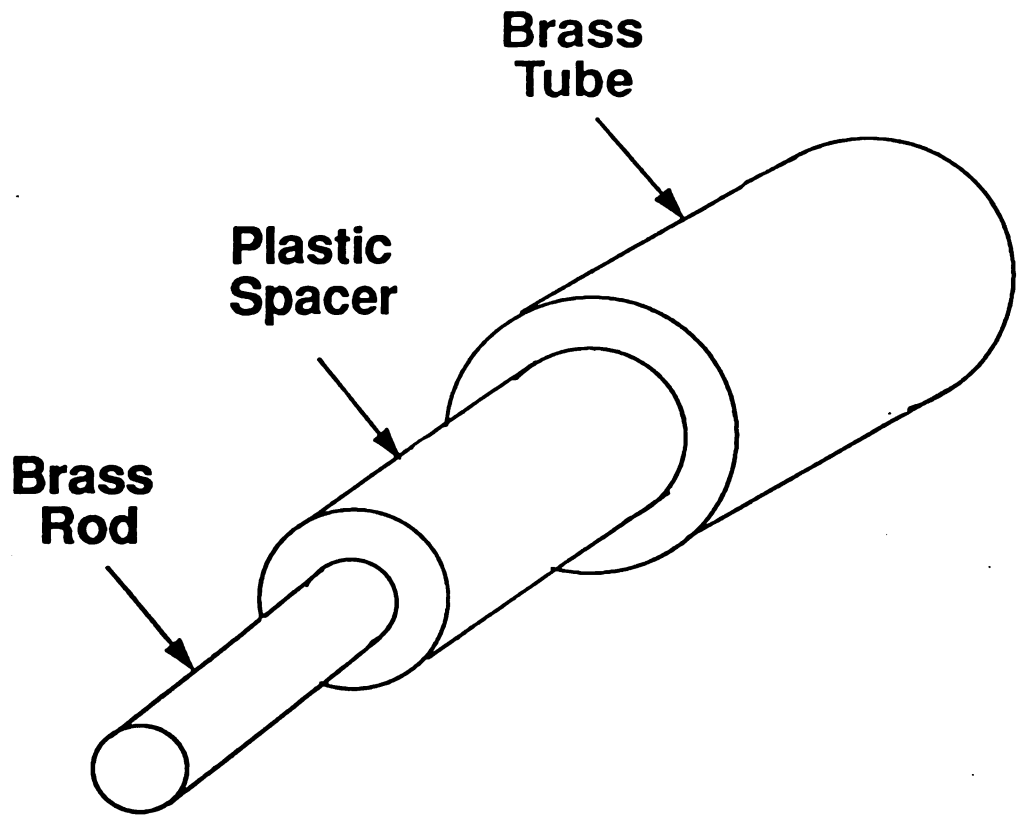

Figure 3-7 Schematic of Conductivity Probe

to a six pin plug compatible with the conductivity meter (Cole Parmer, Chicago IL). These probes were placed at axial positions 30 and 60 cm above the gas sparger and connected to conductivity meters. Because ground loops formed in the column, both signals had to be isolated using a voltage isolator (Metrabyte, Taunton MA). The conductance of each probe was calibrated using known concentrations of aqueous calcium chloride. The conductance versus concentration curves were curve fit using linear regression and generally had correlation coefficients of 0.999. The calibration curves changed as the probes aged, making it necessary to repeat the calibration every few days. For each experiment, 2 mL of 100 g/L calcium chloride was injected at the bottom of the column. The output of each conductivity meter was recorded by the data acquisition system Labtech Notebook at 20 Hz. Five replicates were done for each set of conditions.

3.4.2 Data Analysis

An unsteady-state mass balance on the salt tracer in the liquid phase is shown in Equation 3-8 along with the appropriate boundary and initial conditions[61]

$$\frac{\partial C_L}{\partial t} = D_{ax}\frac{\partial^2 C_L}{\partial z^2} - U_l\frac{\partial C_L}{\partial z}$$

$$\begin{array}{lll} t=0 & z=0 & C_L=C_o \\ t>0 & z=0 & C_L=0 \\ t>0 & z=\infty & C_L=0 \end{array} \qquad (3\text{-}8)$$

where C_L (g/L) is the tracer concentration in the liquid phase, t (sec) is time, D_{ax} (cm^2/s) is the dispersion coefficient, x (cm) is the axial

position, and U_i (cm/s) is the interstitial liquid velocity. This model assumes that the salt tracer exists only in the liquid phase, that the salt concentration is uniform in the radial direction, and that there is no adsorption or diffusion of tracer into the solid phase of the system. However, in the system studied, the solid phase is highly porous, and diffusion into the bead pores is likely. To account for this effect Equation 3-8 must be modified to include tracer diffusion. An unsteady-state mass balance on tracer in the liquid phase that includes disappearance of tracer by diffusion is shown in Equation 3-9. This equation is coupled to the unsteady state mass balance on tracer in the solid phase shown in Equation 3-10[61]

$$\frac{\partial C_L}{\partial t}=D_{ax}\frac{\partial^2 C_L}{\partial z^2}-U_i\frac{\partial C_L}{\partial z}-\frac{3(1-\epsilon_L-\epsilon_g)D_e\epsilon_p}{\epsilon_L R}\left(\frac{\partial C_B}{\partial r}\right)_{r=R} \qquad (3\text{-}9)$$

where ϵ_L is the liquid void fraction, ϵ_g is the gas void fraction, ϵ_p is the bead porosity, D_e (cm^2/s) is the diffusion coefficient, C_B (g/L) is the concentration in the solid phase, R (cm) is the bead radius and r (cm) is the radial position in the bead[61]. The boundary and initial conditions are the same as those listed for Equation 3-8.

$$\frac{\partial C_B}{\partial t}=D_e\frac{1}{r^2}\frac{\partial}{\partial r}\left[r^2\frac{\partial C_B}{\partial r}\right]$$

$$\begin{aligned} t&=0 \quad & C_B&=0 \\ r&=R \quad & C_B&=K_p C_L \\ r&=0 \quad & \frac{\partial C_B}{\partial r}&=0 \end{aligned} \qquad (3\text{-}10)$$

The partition coefficient, K_p, of the tracer between the liquid and solid phases, was assumed to be 1.0 in this study. The assumptions

made in deriving Equations 3-9 and 3-10 were that film mass-transfer resistance was negligible, transport into the beads occurred only by Fickian diffusion, (*i.e.* convection into the beads was negligible) and no adsorption of tracer onto the beads occurred.

Equations 3-8, and 3-9 and 3-10 were solved using the Laplace transforms shown in Equations 3-11 and 3-12 and 3-13, respectively[61]

$$F(s)=\frac{\int_0^\infty C^{II}_{expt} e^{-st}dt}{\int_0^\infty C^{I}_{expt} e^{-st}dt}=e^{\frac{Pe}{2}\left[1-\left(1+\frac{4D_{ax}s}{U_i^2}\right)^{1/2}\right]} \tag{3-11}$$

$$F(s)=\frac{\int_0^\infty C^{II}_{expt} e^{-st}dt}{\int_0^\infty C^{I}_{expt} e^{-st}dt}=e^{\frac{Pe}{2}\left(1-\left[1+\frac{4D_{ax}}{U_i^2}(s+q)\right]^{\frac{1}{2}}\right)} \tag{3-Hx}$$

$$q=\frac{3s\varepsilon_p(1-\varepsilon_L-\varepsilon_g)}{\varepsilon_L R}\left[\coth\left(\frac{Rs\varepsilon_p}{D_e}\right)-1\right] \tag{3-13}$$

where C^{I}_{expt} (g/L) and C^{II}_{expt} (g/L) are the experimental tracer curves from the first and second probes, respectively, and Pe, the Peclet number based on the bead radius (R) is defined as RU_i/D_{ax}.

A computer program developed by Wakao and Kaguei[61] coupled with the optimization program PATERN[83], was used to determine the optimal values of the dispersion coefficient and the interstitial liquid velocity for each set of tracer data. The program of Wakao and Kaguei converted the experimental tracer curves into Fourier series and calculated a predicted tracer curve using the Fourier series of the data from the first probe as an input function and the above transfer functions. The optimization program, PATERN[83], was then

used to vary the dispersion coefficient and the interstitial velocity until the mean square error between the predicted and experimental curves was minimized. These programs are listed in Appendix B.

3.4.3 Diffusion Coefficient

3.4.3.1 Experimental Technique

An experimental technique was developed to measure the effective diffusion coefficient for use in Equations 3-9 and 3-10. A 250 mL beaker was filled with 100 mL of 10 g/L calcium chloride. Fifty mL of beads were measured by displacement in a graduated cylinder, and the excess water was removed by blotting the beads with paper towels. The beads were placed in the calcium chloride solution and agitated on a gyratory shaker at 200 rpm for one hour. The liquid conductivity was measured using a conductivity probe and sampled by Labtech Notebook once a minute. The conductivity probe was calibrated in concentrations of 1, 5, 8, 10, and 12 g/L calcium chloride while agitating at 200 rpm. Several experiments were done at rpm values from 0-300 to ensure that film mass transfer was not controlling.

3.4.3.2 Data Analysis

The unsteady state mass balance on the solid phase assuming that both film mass transfer and adsorption were negligible is given in Equation 3-10. However, different boundary and initial conditions are appropriate for this system[84,85]:

$$\begin{aligned} t=0 \quad & C_B=0 \\ r=R \quad & V_L\frac{\partial C_L}{\partial t}=K_p A_s D_e \frac{\partial C_B}{\partial r}\Big|_R \\ r=0 \quad & \frac{\partial C_B}{\partial r}=0 \end{aligned} \tag{3-14}$$

where A_s (cm^2) is the surface area of the beads. The solution of Equation 3-10 with the boundary and initial conditions given in Equation 3-14 yields Equation 3-15[84,85].

$$C_B=\frac{C_o\alpha}{1+\alpha}\left[1+\sum_{n=1}^{\infty}\frac{6(1+\alpha)e^{\left(\frac{-D_A q_n^2 t}{R^2}\right)}}{9+9\alpha+q_n^2\alpha^2}\frac{R\sin\left(\frac{q_n r}{R}\right)}{r\sin(q_n)}\right] \tag{3-15}$$

The variable α is defined in Equation 3-16,

$$\alpha=\frac{V_L}{K_p V_B} \tag{3-16}$$

where V_L (mL) is the liquid volume in the beaker, V_B (mL) is the bead volume accessible to tracer. The n^{th} root of Equation 3-17 is q_n.

$$\tan(q_n)=\frac{3q_n}{3+\alpha q_n^2} \tag{3-17}$$

If experimental conditions are such that the liquid film around the beads is negligible then the concentration at the surface of the bead is equal to the concentration in the bulk liquid. For that situation at r=R, C_B in Equation 3-15 can be substituted with C_L, and Equation 3-18 results[83,84].

$$C_L=\frac{C_o\alpha}{1+\alpha}\left[1+\sum_{n=1}^{\infty}\frac{6(1+\alpha)e^{\frac{-D_A q_n^2 t}{R^2}}}{9+9\alpha+q_n^2\alpha^2}\right] \tag{3-18}$$

PATERN was used to vary the the effective diffusion coefficient until the mean square error between the theoretical and experimental

curves was minimized. Five replicates were measured to determine the effective diffusion coefficient. The program used to calculate diffusion coefficients from experimental data is listed in Appendix B.

3.4.3.3 Solute Exclusion Technique to Determine Pore Structure

Alginate beads consist of a three dimensional structure of crosslinked β-D-mannuronic and α-L-guluronic acids[86]. The cross links define water-filled pores having a distribution of pore diameters. The solute exclusion technique of Stone and Scallan[87,88] was used to determine this distribution of pore diameters. Because a molecule can only enter pores larger than the molecule's diameter, all pores smaller than this diameter will be inaccessible to the molecule. Thus, by using a range of molecules with different diameters, it is possible to measure the fraction of pores that is inaccessible to a given molecule size and construct a pore size distribution. In the technique, a known mass of aqueous solute solution is equilibrated with a known mass of porous beads. The change in concentration of the diffusing solute is measured by optical rotation, and the volume of inaccessible pores is calculated from a solute balance before and after contacting, as shown in Equation 3-19[89]

$$\delta_i p=(w+q)-w\frac{C_i}{C_f} \qquad (3\text{-}19)$$

where δ_i is the specific mass of pores inaccessible to a solute of size i (g of inaccessible water/g of beads), w (g) is the mass of solute solution added, q (g) is the mass of water in the beads, p (g) is the

dry weight of the beads, C_i (g/mL) is the initial concentration of solute, and C_f (g/mL) is the final concentration after equilibration corrected for minor water soluble compounds in the beads. The volume of inaccessible pores per unit volume can be calculated as shown in Equation 3-20

$$V_i = \delta_i \frac{\rho_B}{\rho_w} \tag{3-19}$$

where V_i (mL of inaccessible water/mL of beads) is the specific volume of pores inaccessible to a solute of size i, ρ_w is the density of water, and ρ_B is the bead density.

Nine linear dextrans were used in this study, ranging in molecular weight from 6000 to 2 million g/mole, in addition to three carbohydrates ranging from 180 to 504 g/mole. Linear dextrans have been shown to behave as hydrated spheres in aqueous solution[88]; this allows a direct correlation between solute diameter and pore width. Diameters of the carbohydrates and dextrans in solution are calculated from their diffusion coefficients according to the Stokes-Einstein formula[88]; values used here have been taken from Weimer and Weston[90] and are listed with their molecular weights in Table 3-1.

Solute concentrations of 2% were prepared by dissolving 2 g of anhydrous solute in 100 mL of distilled water. A mass of beads with a volume of approximately 10 mL was weighed into a 20 mL polyethylene scintillation bottle with leakproof caps, and solute solution was added until the bottle was full. Three replicates were used per solute. Three bottles containing only distilled water and

Table 3-1 Molecular Probes Used in the Solute Exclusion Technique[89]

Solute	Vendor	M_w[a]	M_w/M_n[a]	Estimated Diameter[c] Å
Glucose	Sigma	180	1.0	8
Fructose	Sigma	180	1.0	8
Maltose	Fisher	342	1.0	10
Raffinose	Sigma	504	1.0	12
Dextran 6K	Fluka	6,000	N.A.[b]	38
Dextran T10	Pharamacia	10,500	1.74	51
Dextran 15-20K	Polysciences	17,500*	N.A.	61
Dextran T40	Pharmacia	38,800	1.60	90
Dextran T70	Pharmacia	72,200	1.88	118
Dextran 200-300K	Polysciences	2.5×10^{5}*	N.A.	204
Dextran T500	Pharmacia	5.07×10^{5}	2.16	270
Dextran T2000	Pharmacia	2.0×10^{6}	N.A.	560

a Obtained from vendor's lot analysis except where indicated by (*), where M_w is calculated as the midpoint of the molecular weight range reported.

b N.A. = Not Available

c Probe diameters estimated using the values given in the original work by Stone and Scallan[87,88] and from Weimer and Weston[90].

beads were also prepared as blanks, to determine the effects of water soluble materials that diffuse out of the beads on the measured dextran concentration. The bottles were allowed to equilibrate overnight with occasional shaking. Ten mL of the liquid were withdrawn, filtered with a 0.45 μm acrodisc, and placed into a 10 cm polarimeter sample tube of an Autopol III Automatic Polarimeter (Rudolph Research, Flanders NJ). The remaining liquid was removed, and the bottles, still containing beads, were filled with distilled water and allowed to sit for 30 minutes. The water was replaced with fresh distilled water and this process was repeated 9 times to remove most of the solute from the beads. The beads were then dried to constant weight at 105°C and their dry weight recorded.

The optical rotations measurements were corrected for water soluble materials originally contained in the beads by subtracting out the averaged optical rotation of the three blanks as shown in Equation 3-21.

$$O_{f,c}=O_f-p\left(\frac{O_f}{p}\right)_{blank} \qquad (3\text{-}21)$$

where $O_{f,c}$ is the corrected optical rotation reading, O_f is the optical rotation reading of the sample, p (g) is the dry weight of the sample, $(O_f/p)_{blank}$ is the averaged optical rotation readings of the blanks divided by the dry weight of the blanks. The solute molecules were assumed to be spheres in solution[88]; thus a pore that was inaccessible to a solute was assumed to have a diameter smaller than the diameter of the spherical solute molecule. Pore size distributions were

measured for beads containing only alginate, beads containing 5% by weight magnetite, and beads containing 50% by weight magnetite. The pore size distributions for the 0 and 5% beads were empirically fit to Equation 3-22

$$\delta_i = \frac{a_o}{1+e^{a_1-a_2x^2}} + a_3x - a_4 \qquad (3\text{-}22)$$

where x is defined as $\log_{10}[D] - \log_{10}[4]$, D (Å) is defined as the molecular diameter, and a_0, a_1, a_2, a_3, and a_4 are empirical constants. Water has a diameter of 4 Å, and it is assumed that all pores in the material are accessible to water; therefore, the value of δ_i corresponding to 4 Å is zero. The logarithm of 4 Å was subtracted from the logarithm of the molecule diameter to give the variable x a lower bound of zero. The pore size distributions for the 50% beads were fit to Equation 3-23

$$\delta_i = \frac{a_o}{1+e^{a_1-a_2x^2}} + \frac{a_3x}{0.5+x^2} - a_4 \qquad (3\text{-}23)$$

The forms of Equations 3-22 and 3-23 were chosen solely on their ability to fit the experimental data. The values of the constants were determined using Peakfit (Jandel Scientific, San Rafael CA).

3.5 Gas To Liquid Mass-Transfer

3.5.1 Experimental Procedure

Figure 3-8 shows the experimental apparatus for the mass-transfer experiment. The 55 gallon holding tank contained reverse-osmosis water that was continually sparged with nitrogen gas until the oxygen concentration was approximately 0-4 % of the air saturation value.

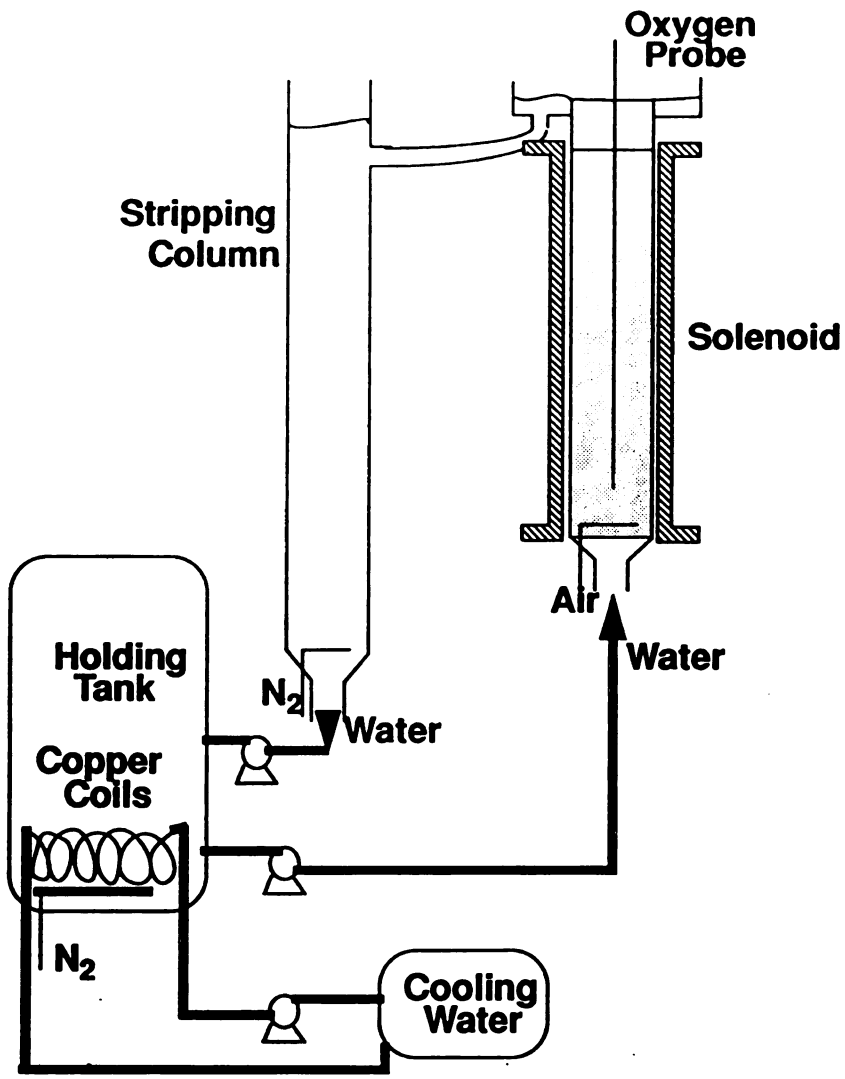

Figure 3-8 Schematic of Experimental Apparatus for Measuring Mass Transfer Coefficients

The oxygen concentration in the tank was continuously measured with a dissolved oxygen probe (YSI, Yellowsprings OH). Water was pumped from this tank, through a rotameter, and into the column, where it was sparged with air. Water leaving the top of the column was gravity fed to the top of a glass stripping column 5 cm in diameter and 137 cm long, where it was countercurrently contacted with nitrogen sparged through a glass frit. Water exiting this column was pumped back into the holding tank. The combination of nitrogen sparging in both the stripping column and the holding tank was sufficient to keep the dissolved oxygen concentration in the holding tank within 5% of the desired value. Water at 0°C was pumped through a copper cooling coil submerged in the holding tank to remove heat generated by the pumps. The temperature in the holding tank was controlled at 25°C ± 0.2°C using this method. The temperature was measured using a thermocouple (Cole Parmer, Chicago IL).

The oxygen concentration in the column was measured with a Clark style dissolved oxygen microprobe (Diamond General, Ann Arbor MI) with a tip diameter of 2 mm connected to a chemical microsensor (Diamond General, Ann Arbor MI). The probe was calibrated in 25°C RO water. The water was sparged with air through a glass frit for 15 minutes, at which time the reading on the microsensor was adjusted to 100%. The water was then sparged with nitrogen for 15 minutes, and the reading was adjusted to 0%. This procedure was repeated until the microsensor gave the correct reading after sparging 15 minutes with either air or nitrogen. The probe was then placed in the column at a position 5 cm above the

sparger. The output of the microsensor was sampled by Labtech Notebook for two minutes at a rate of 1 Hz. This process was repeated for positions 15, 30, 45, 60, and 75 cm above the sparger. Three replicates were performed for each set of conditions studied.

3.5.2 Data Analysis

The steady state method was used to calculate the gas-to-liquid mass-transfer coefficient (k_La). A steady-state mass balance on the liquid in the column is shown in Equation 3-24[79].

$$\frac{1}{Pe}\frac{d^2C_L}{dz^2}-\frac{dC_L}{dz}+St(C_L^*-C_L)=0 \qquad (3\text{-}24)$$

where Pe and St are defined as

$$Pe=\frac{U_L L}{D_{ax}\epsilon_L} \qquad St=\frac{(k_La)L}{U_L} \qquad (3\text{-}25)$$

where C_L (mg/L) is the concentration of oxygen in the water, C_L^* (mg/L) is the concentration of oxygen in the water that would be in equilibrium with the oxygen in the gas phase, z (axial position divided by the column length) is the axial position, U_L (cm/s) is the superficial liquid velocity, D_{ax} (cm^2/s) is the liquid dispersion coefficient, ϵ_L is the liquid void fraction, L (cm) is the column length, and k_La (s^{-1}) is the mass transfer coefficient. Equation 3-24 was derived assuming that axial liquid mixing in the column can be described as a dispersed plug flow model and that the mole fraction of oxygen in the gas phase does not change appreciably across the column. The value of C_L^* can be defined as follows from Henry's law[79]:

$$C_L^* = \frac{P x_{O_2}}{H} \tag{3-26}$$

where P (atm) is the total pressure at a given position in the column, x_{O2} (mole O_2/mole gas) is the mole fraction of oxygen in the gas phase, and H (atm mole O_2/mole gas) is the Henry's law constant for oxygen in water. The pressure in the column varies as described in Equation 3-27[79,80]

$$P = P_T[1+\alpha(1-z)]$$
$$\alpha = \frac{(\rho_s \varepsilon_s + \rho_L \varepsilon_L + \rho_g \varepsilon_g) gL}{g_c P_T} \tag{3-27}$$

where ρ_s is the solid density (kg/m^3), ρ_L is the liquid density (kg/m^3), ρ_g is the gas density (kg/m^3), ϵ_s is the solid fraction, g (m/s^2) is the acceleration due to gravity, and P_T (Pa) is the pressure at the top of the column. Combining Equations 3-24 through 3-27 yields the following differential equation[79]

$$\frac{1}{Pe}\frac{d^2C_L}{dz^2} - \frac{dC_L}{dz} - StC_L = -St(a+bz)$$
$$a = \frac{P_T x_{O_2}(1+\alpha)}{H} \qquad b = \frac{-P_T x_{O_2} \alpha}{H} \tag{3-28}$$

with the following boundary conditions:

$$z=0 \qquad C_L = C_i + \frac{1}{Pe}\frac{dC_L}{dz}$$
$$z=1 \qquad \frac{dC_L}{dz} = 0 \tag{3-29}$$

where C_i (mg/L) is the inlet oxygen concentration. The analytical solution to Equation 3-28 is given by 3-30 to 3-35[79]

$$C_L = A_1 e^{r_1 z} + A_2 e^{r_2 z} + a - \frac{b}{st} + bz \tag{3-30}$$

where

$$r_{1,2} = \frac{Pe}{2}\left(1 \pm \sqrt{1 + \frac{4St}{Pe}}\right) \tag{3-31}$$

$$A_1 = \frac{(Br_2 e^{r_2} - br_1)}{N} \tag{3-32}$$

$$A_2 = \frac{(-Br_1 e^{r_1} + br_2)}{N} \tag{3-33}$$

$$B = [a - C_i - \frac{b}{St}]Pe - b \tag{3-34}$$

$$N = r_1^2 e^{r_1} - r_2^2 e^{r_2} \tag{3-35}$$

The experimental data were fit using PATERN to find the value of k_La which minimized the mean square error between the experimental data and the theoretical curve given by Equations 3-30 through 3-35. The computer program used to calculate the mass-transfer coefficient is listed in Appendix B.

Chapter IV: Fluidized Bed Model

Determination of dispersion coefficients using the conventional dispersion model (Equation 3-8) is much more convenient than using the model including intraparticle diffusion of the tracer (Equations 3-9 and 3-10). However, there are no established criteria with which to judge whether intraparticle diffusion can be neglected. Additionally, when intraparticle diffusion is significant, it would be convenient to be able to correct the apparent dispersion coefficient determined using Equation 3-8 for the effect of diffusion. For these reasons, a mathematical model of a fluidized bed was developed that could predict the effect of diffusion on the apparent axial dispersion coefficient. The modelling results were used to calculate a dispersion correction factor (η), defined in Equation 4-1, that is analogous to the catalyst effectiveness factor.

$$\eta = \frac{D_{ax,app}}{D_{ax}} \tag{4-1}$$

where $D_{ax,app}$ is the apparent dispersion coefficient calculated from Equation 3-8, and D_{ax} is the true dispersion coefficient calculated from Equations 3-9 and 3-10. Development of the model is described below.

4.1 Derivation

The stirred tanks in series model have been widely used to describe fluid mixing in flow systems. In this model, the effluent from the first tank is assumed to be the feed to the second tank, and so forth, for all the tanks in series. By increasing the number of tanks, the system behavior asymptotically approaches plug flow. At

the other extreme, a single stirred tank describes a perfectly mixed system. Equation 4-2 is an unsteady-state mass balance on the liquid phase of a stirred tank containing gas, liquid and solid phases. This equation is derived in Appendix A.5

$$UA(C_i-C_L)=V_L\frac{\partial C_L}{\partial t}+\frac{\varepsilon_p(1-\varepsilon_L-\varepsilon_g)V_L}{\varepsilon_L}\frac{\partial C_B}{\partial t} \qquad (4\text{-}2)$$

where A (cm^2) is the cross-sectional area of the stirred tank; C_i (g/L) is the inlet concentration of tracer to the tank; U (cm/s) is the superficial liquid velocity; C_L (g/L) is concentration of tracer in the tank; V_L (mL) is the tank volume; ϵ_g, ϵ_L, and ϵ_p are the gas volume fraction, liquid volume fraction and the particle porosity, respectively; and C_B (g/L) is the concentration of tracer in the beads.

The term $\partial C_B/\partial t$ coupled Equation 4-2 to the unsteady state mass balance on tracer concentration in the solid phase given in Equation 3-10. The boundary and initial conditions given in Equation 4-3 are appropriate for this case.

$$\begin{array}{ll} t=0 & C_B=0 \\ r=R & C_B=C_L \\ r=0 & \dfrac{\partial C_B}{\partial r}=0 \end{array} \qquad (4\text{-}3)$$

A solution to Equation 3-10 when C_L is constant with time was developed by Carslaw and Jaeger[91]. By applying Duhamel's theorem to this solution for C_B as a function of time and radial position in the bead, an expression can be obtained for C_B as a function of time[92]:

$$C_B(r,t)=2D_e\sum_{n=1}^{\infty}\left\{(-1)^{n+1}\frac{n\pi}{R}\frac{\sin(\frac{n\pi r}{R})}{r}\int_0^t C_L e^{\frac{-D_e n^2\pi^2(t-\lambda)}{R^2}}d\lambda\right\} \quad (4\text{-}4)$$

where λ is a dummy variable of integration. The concentration in the beads, C_B, must be averaged over the bead volume as shown in Equation 4-5

$$C_B(t)=\frac{3}{R^3}\int_0^R C_B(r,t)r^2dr \quad (4\text{-}5)$$

Combining Equation 4-4 and 4-5 and changing the order of integration and summation yields Equation 4-6[93].

$$C_B=\frac{6D_e}{R^2}\sum_{n=1}^{\infty}\left\{\int_0^t C_L e^{\frac{-D_e N^2\pi^2(t-\lambda)}{R^2}}d\lambda\right\} \quad (4\text{-}6)$$

Taking the derivative of C_B with respect to time, and integrating by parts gives Equation 4-7[91].

$$\frac{\partial C_B}{\partial t}=\frac{6D_e}{R^2}\sum_{n=1}^{\infty}\left\{\int_0^t \frac{\partial C_L}{\partial \lambda}e^{\frac{-D_e n^2\pi^2(t-\lambda)}{R^2}}d\lambda\right\} \quad (4\text{-}7)$$

Combining Equations 4-2 and 4-7, taking the Laplace transform and rearranging yields Equation 4-8

$$\frac{\overline{C_L}}{\overline{C_i}}=\left[1+\frac{V_L}{UA}s+\frac{V_L\varepsilon_p(1-\varepsilon_L-\varepsilon_g)6D_e}{UA\varepsilon_L R^2}\sum_{n=1}^{\infty}\frac{s}{s+\frac{D_e n^2\pi^2}{R^2}}\right]^{-1} \quad (4\text{-}8)$$

where $\overline{C}_L$ and $\overline{C}_i$ are the Laplace transforms of C_L and C_i, respectively.

4.2 Simulation

For each simulation, the input concentration to tank one was a pulse described by a gamma density function[94] shown in Equation 4-9. The gamma density function was chosen due to its resemblance to a real pulse.

$$C_i = \frac{\lambda^\alpha}{\Gamma(\alpha)} t^{\alpha-1} e^{-\lambda t} \qquad (4\text{-}9)$$

$$\Gamma(\alpha) = \int_0^\infty u^{\alpha-1} e^{-u} du$$

The values of λ and α were arbitrarily chosen as 5 and 15, respectively. The output from tank one was then calculated from Equation 4-8 using the computer program developed by Wakao and Kaguei[61]. The output of the first tank, C_L, then became the input to the second tank and so on through each of the n tanks in series. The output of the tanks corresponding to axial positions of 30 and 90 cm were saved and used to calculate dispersion coefficients for each simulation using Equation 3-8 and Equations 3-9 and 3-10. A computer program capable of predicting the effects of both axial dispersion and solid phase diffusion was developed to calculate the correction factor as a function of the system variables and is listed in Appendix B. Table 4-1 shows the parameter values used to simulate the dispersion experiments.

Table 4-1 Values Used in Parametric Studies

Column Length, L_c	1 m
Column Diameter, d_c	5 cm
Superficial Liquid Velocity, U	3.0-10.0 cm/s
Bead Radius, R	0.25-4.0 cm
Bead Porosity, ϵ_p	0.05-0.98
Liquid Fraction, ϵ_L	0.3-0.99
Diffusion Coefficient, D_e	0.1×10^{-9}-5.0×10^{-9} m^2/s
Number of Stirred Tanks, N	10-1000

4.3 Dimensional Analysis

Dimensional analysis is frequently applied in engineering analysis because it minimizes the number of independent variables needed to describe the system and gives insight into the physical processes that control the systems's behavior. The system variables included in the governing material balance equations were the dispersion coefficient, diffusion coefficient, liquid velocity, gas volume fraction, liquid volume fraction, bead void fraction, and bead radius. The Buckingham Pi method[95] was used to determine the important dimensionless groups of these parameters. All possible dimensionless permutations of these variables were examined, and the one that best correlated the computed correction factor results is

$$\Phi = \frac{D_e D_{ax,app} \varepsilon_p^2 (1-\varepsilon_L-\varepsilon_g)^2}{R^2 U^2} \tag{4-10}$$

Another important dimensionless group is the Peclet number defined in Equation 4-11

$$Pe = \frac{L_C U}{D_{ax,app}} \tag{4-11}$$

where L_C (cm) is the column length.

Chapter V: Results

5.1 Solenoid

The magnetic field strength was measured as a function of current at the center of the column with a Gaussmeter. The results are shown in Figure 5-1 along with the theoretical values predicted by Equations 3-1 to 3-3. The experimental values agree quite well with the theoretical prediction. Figure 5-2 shows the predicted and experimental axial variation of the magnetic field at the radial center of the solenoid. The magnetic field was almost constant over the central 80% of the solenoid length and dropped off rapidly to one half the maximum field strength at the ends of the solenoid. Measurements of the magnetic field were also conducted while the magnetite impregnated beads were in the column, and there was no measurable difference in the field strength from the empty column case. Solenoid heat generation was investigated by measuring the temperature of the cooling water as it entered and exited the solenoid. For currents above 1.5 amps there was a noticeable rise in the cooling water temperature. A water flow rate of 650 mL/s at 10°C was adequate to keep the outside surface of the solenoid at room temperature for the highest current (5 amps) used in the study.

5.2 Bed Regimes

The bed structure was observed at two positions in the column: at the center of the column, where the field strength was maximum (up to 300 gauss) and at the top of the solenoid, where the field strength was one half of maximum. The field of view at the center was limited to a square centimeter allowed by the periscope. Although observations at the top of the solenoid were limited to field

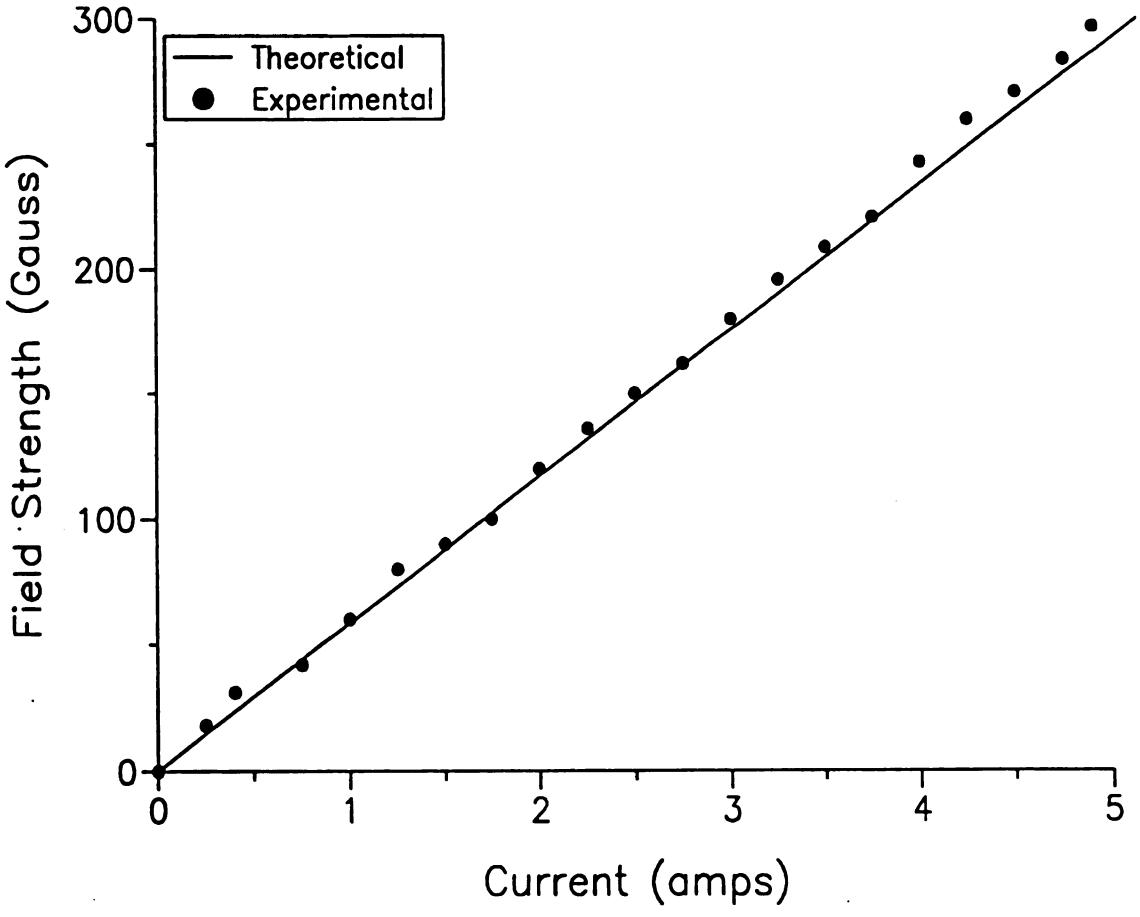

Figure 5-1 **Magnetic Field Strength versus Current: Experimental and Theoretical Values**

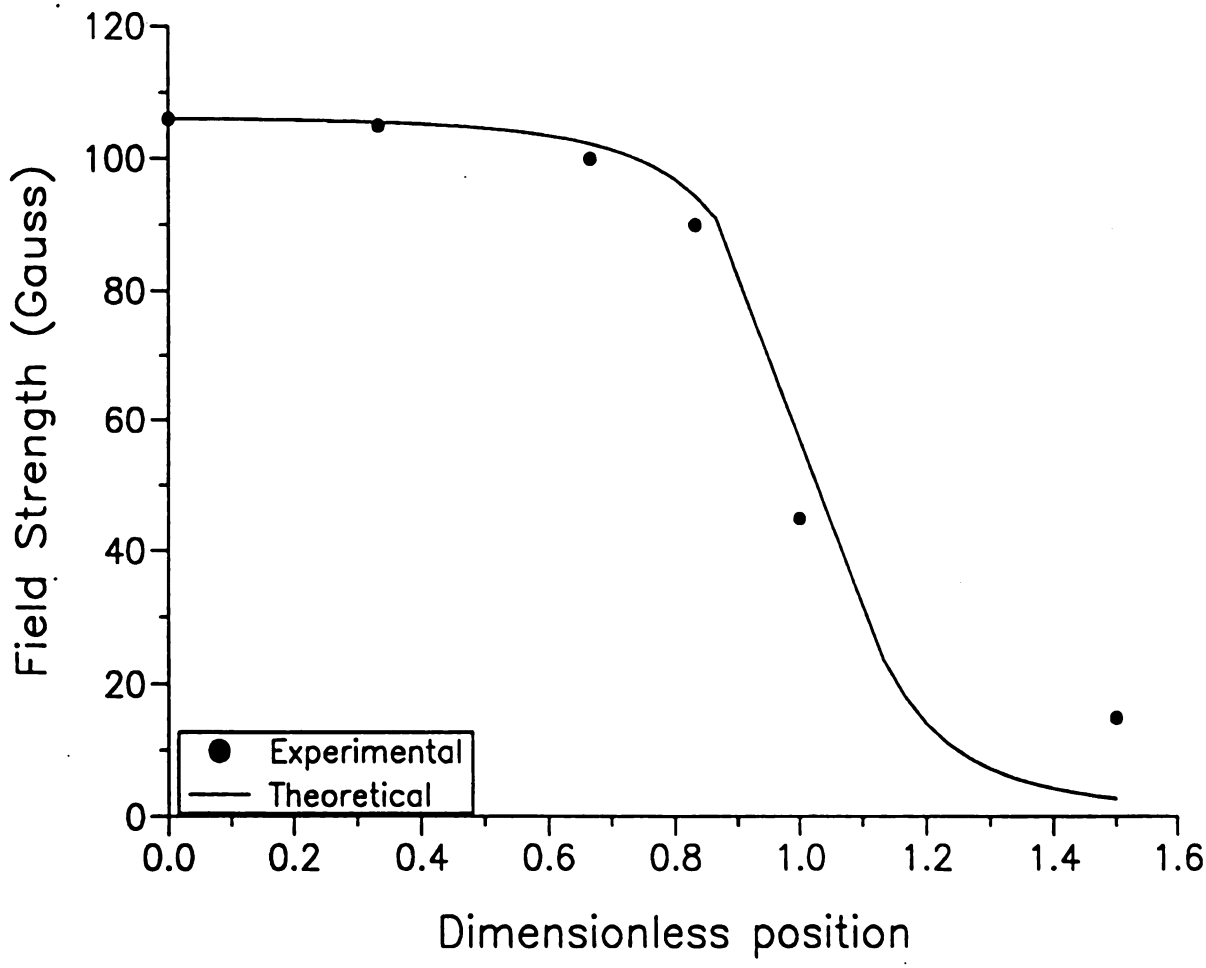

Figure 5-2 Axial Variation of Magnetic Field: Experimental and Theoretical Values

strengths of 150 gauss or less, more accurate observations were possible because of the wider field of view. The bed regimes observed over the range of 0-300 gauss and gas velocities from 0.6 to 2.0 cm/s are shown in Figures 5-3 to 5-5 for liquid velocities of 5.15, 6.44, and 7.71 cm/s. The experiments were performed by setting the liquid and gas flow rates and then increasing the magnetic field strength from 0 to 300 gauss. When the experiments were repeated while decreasing the magnetic field strength, no hysteresis was observed.

Six basic bed regimes were observed: random, chain, chain-channel, destabilized, channel, and frozen. The random regime, observed at the lowest field strength, was characterized by solid particles in completely random motion. Bubble size ranged from 1 mm diameter to small slugs up to 2 cm in diameter. Random bed behavior was typical of a non-magnetized bed. In the chain regime, the solid particles formed chains 3-4 particles in length as the magnetic field strength induced significant magnetic dipoles in the particles. In the chain-channel regime, small chains coalesced into a three-dimensional mesh structure that contained voids or channels. These structures were not permanent, but shifted periodically. In the destabilized regime, channels were too narrow to accomodate bubble slugs. As a result these slugs often broke up the three dimensional meshes into small clumps of 10-20 particles. Within each clump, particles were arranged in a rosette structure, where the particle in the center was surrounded by six particles. In the channel regime, the bubble slugs could no longer break up the mesh, and the channels described previously remained fixed. Bubbles rose through

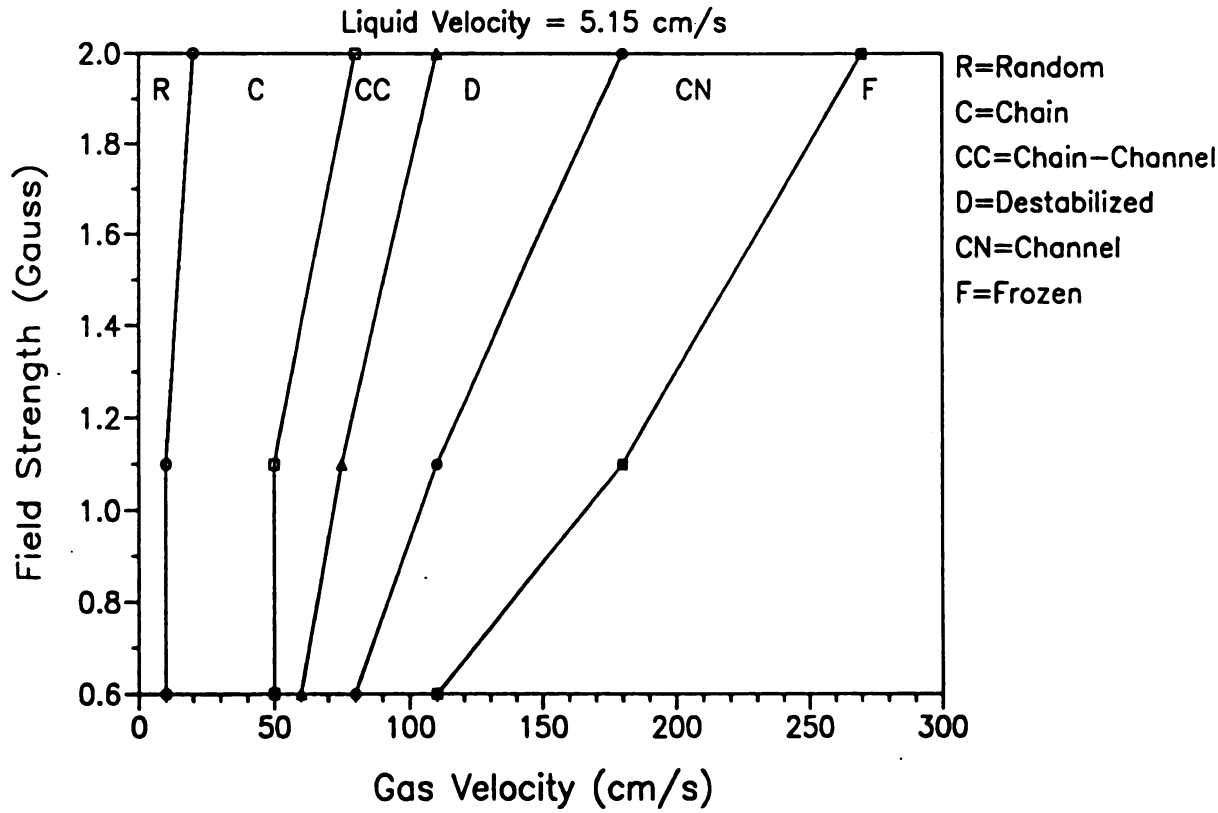

Figure 5-3 Bed Regimes For a Liquid Velocity of 5.15 cm/s

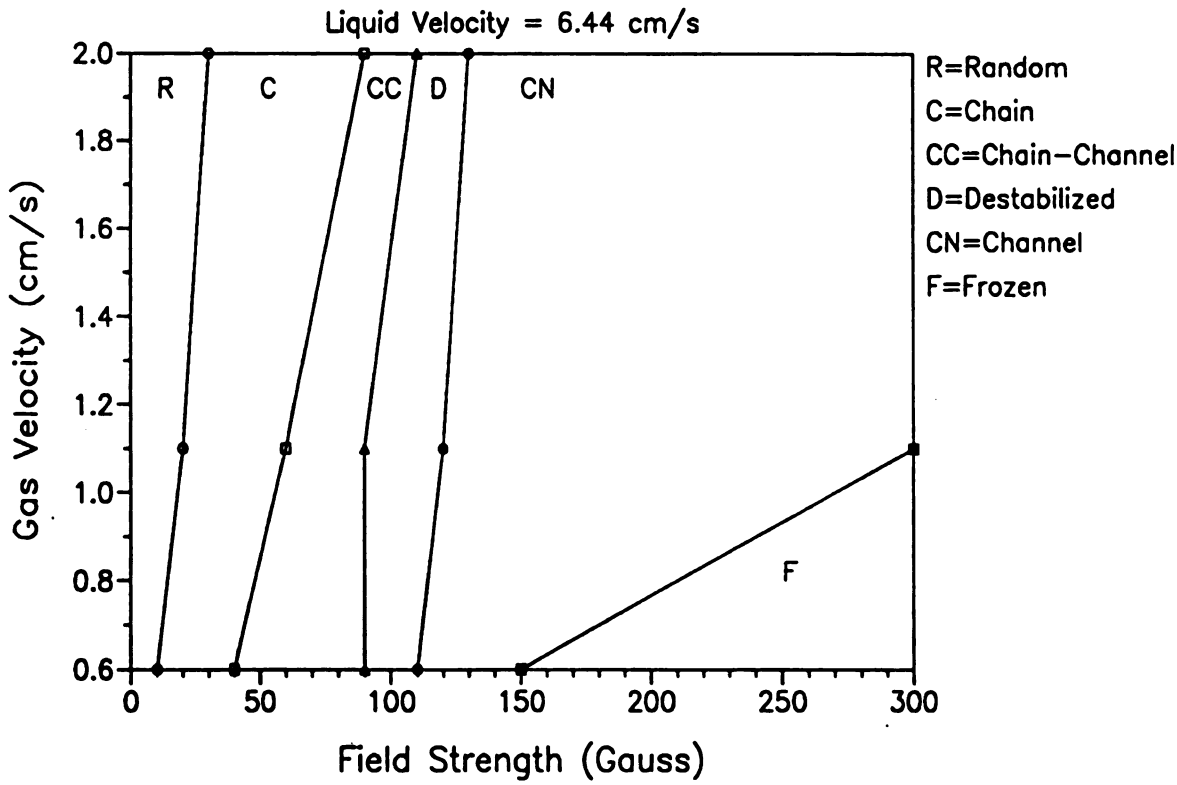

Figure 5-4 Bed Regimes for a Liquid Velocity of 6.44 cm/s

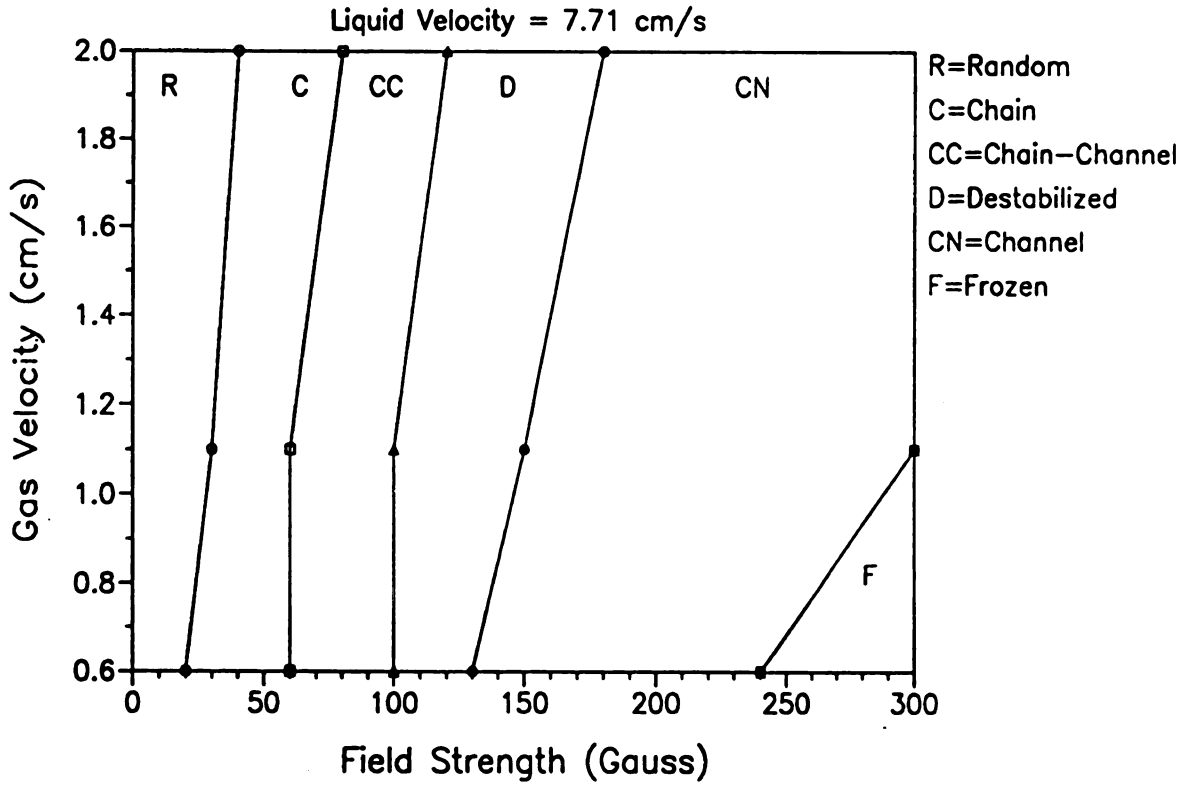

Figure 5-5 Bed Regimes for a Liquid Velocity of 7.71 cm/s

these channels, but the slugs observed in the previous structures were absent. Significant numbers of bubbles were also observed to travel next to the column wall. The only solid motion observed was particle vibration. In the frozen regime, even the particle vibrations stopped. The entire bed behaved as a single mass that was fluidized by the liquid and gas in the column.

The observed bubble sizes did not change in the chain, chain-channel and destabilized regimes from those observed in the random regime. In the channel and frozen regimes, no bubble slugs were observed, indicating that they may have been broken up by the bed structure. In addition, at a liquid velocity of 5.15 cm/s and gas velocities of 0.6 and 1.1 cm/s, small bubbles (1-2 mm in diameter) became entrapped in the three-dimensional mesh structure of the chain-channel regime and were held in place for several seconds. This behavior was observed to a lesser extent for a liquid velocity of 6.44 cm/s and a gas velocity of 0.6 cm/s and not at all at the highest liquid velocity.

5.3 Gas Void Fraction

Figure 5-6 shows a sample of the optical probe's output. Each peak represents a bubble contacting the probe tip. Calibration of the probe was described in Section 3.3.2. The percentage of peak height as defined in Figure 3-6 was found to be 10%.

The effects of magnetic field strength and gas velocity on gas void fraction are shown in Figures 5-7 to 5-9 for liquid velocities of 5.15, 6.44, and 7.71 cm/s, respectively. These same data are shown with their 95% confidence levels in Figures 5-10 to 5-12. Figure 5-7 shows that for a liquid velocity of 5.15 cm/s, gas void fraction

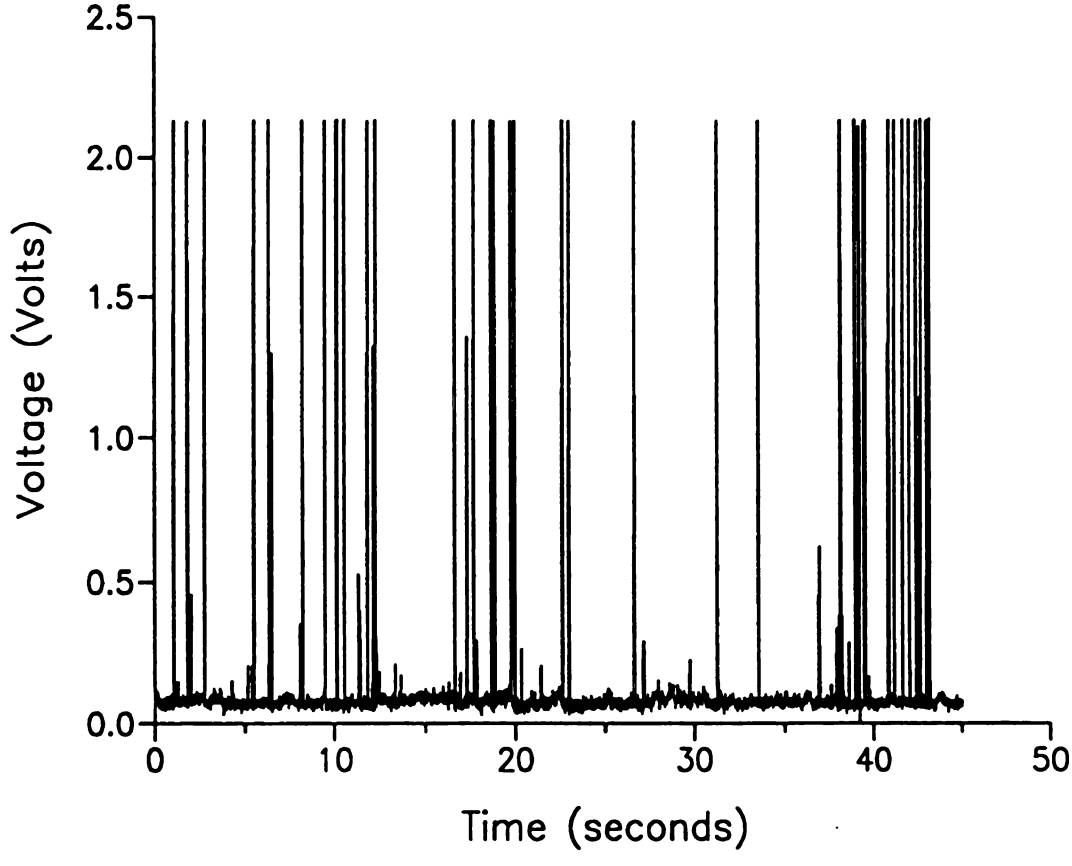

Figure 5-6 Experimental Data from Optical Probe

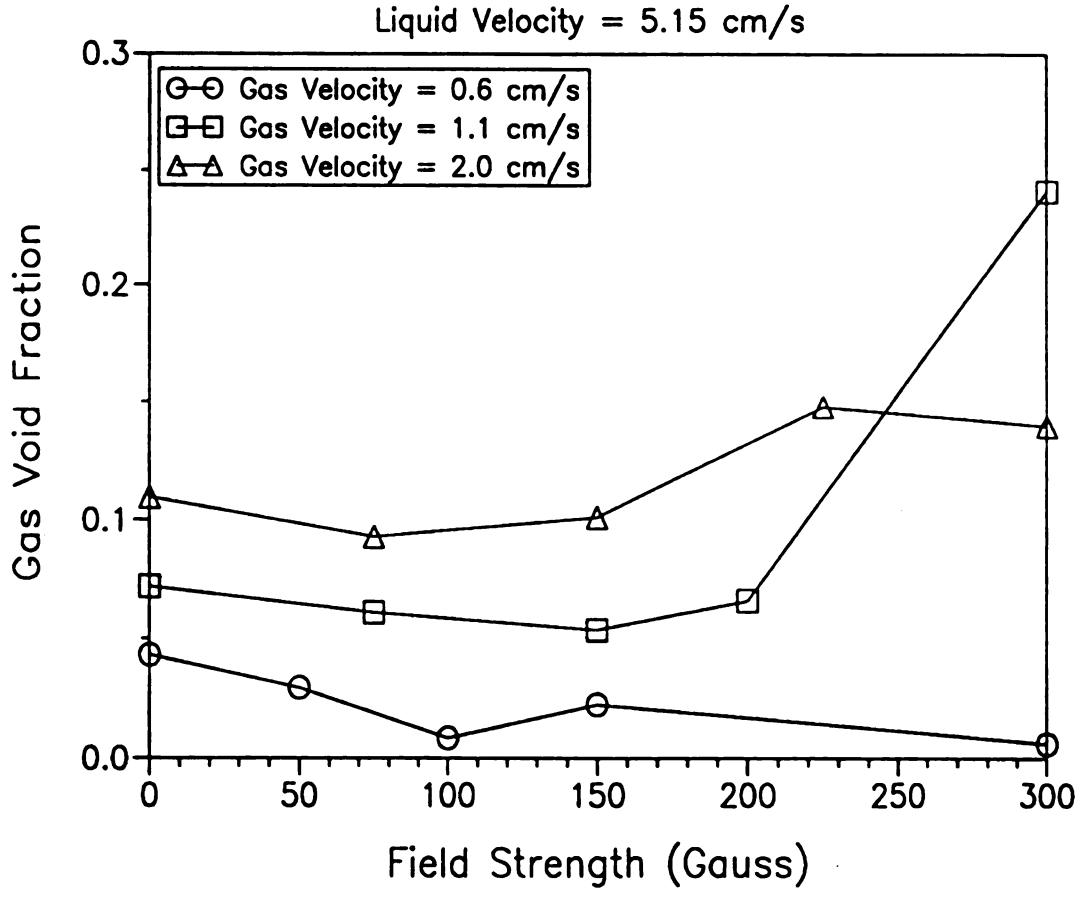

Figure 5-7 **Gas Void Fraction Data as a Function of Magnetic Field Strength for a Liquid Velocity of 5.15 cm/s and Gas Velocities of 0.6, 1.1, and 2.0 cm/s**

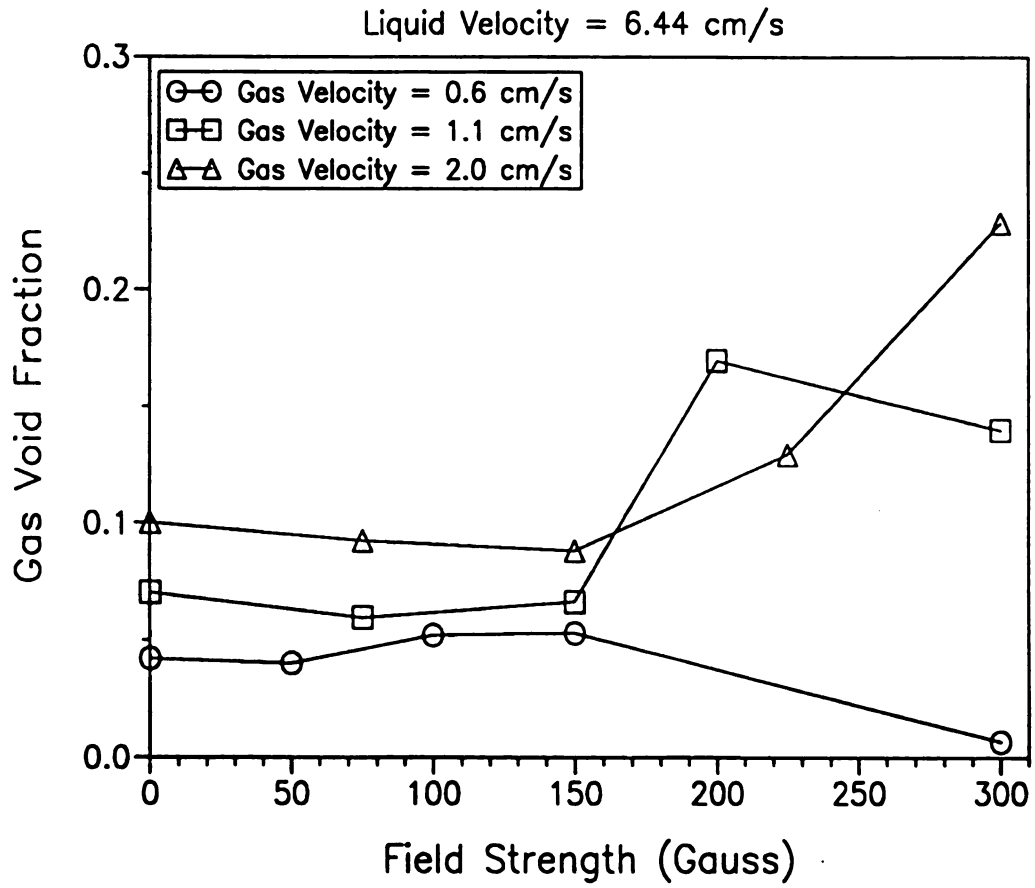

Figure 5-8 **Gas Void Fractions as a Function of Magnetic Field Strength for a Liquid Velocity of 6.44 cm/s and Gas Velocities of 0.6, 1.1, and 2.0 cm/s**

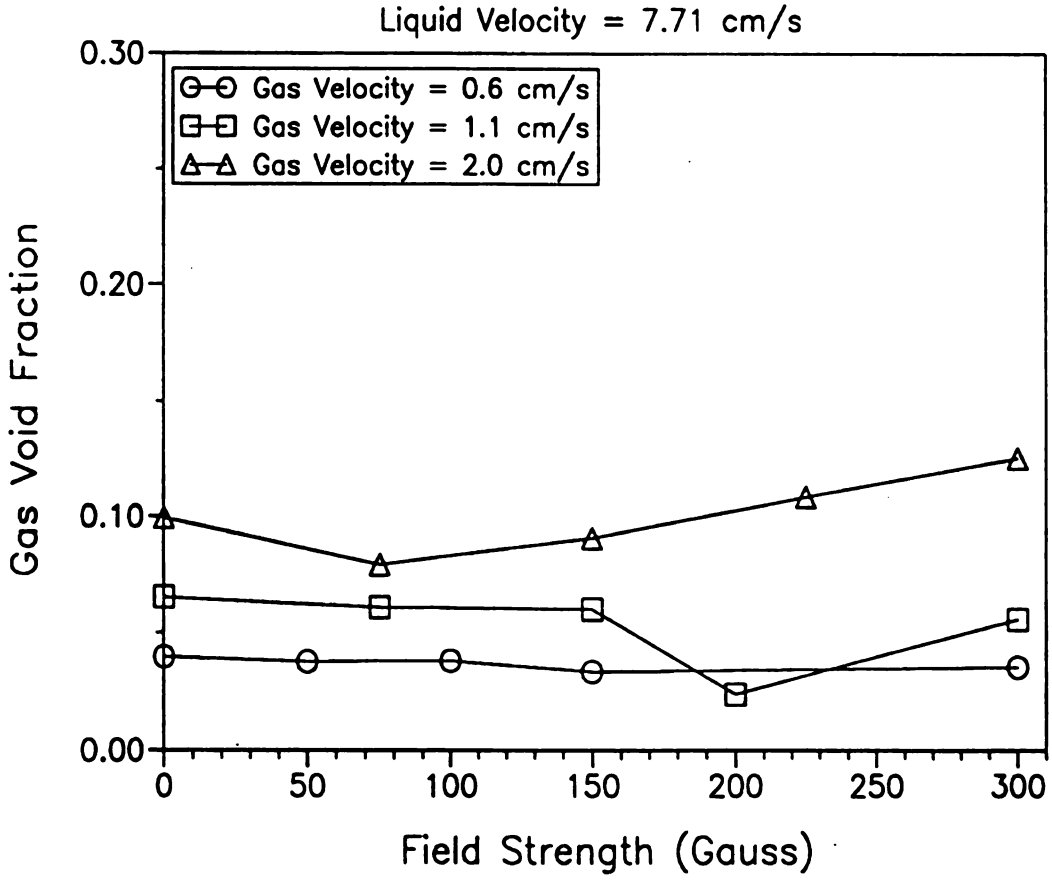

Figure 5-9 **Gas Void Fractions as a Function of Magnetic Field Strength for a Liquid Velocity of 7.71 cm/s and Gas Velocities of 0.6, 1.1, and 2.0 cm/s**

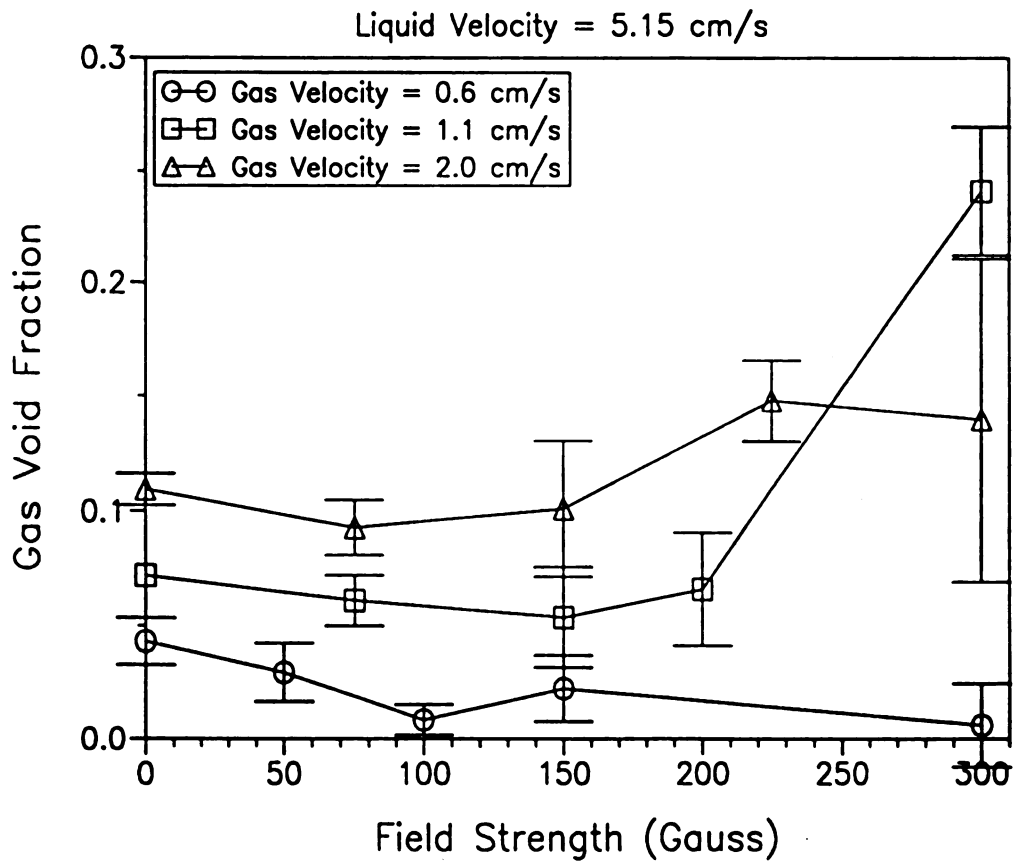

Figure 5-10 95% Confidence Intervals for Gas Void Fraction Data in Figure 5-7

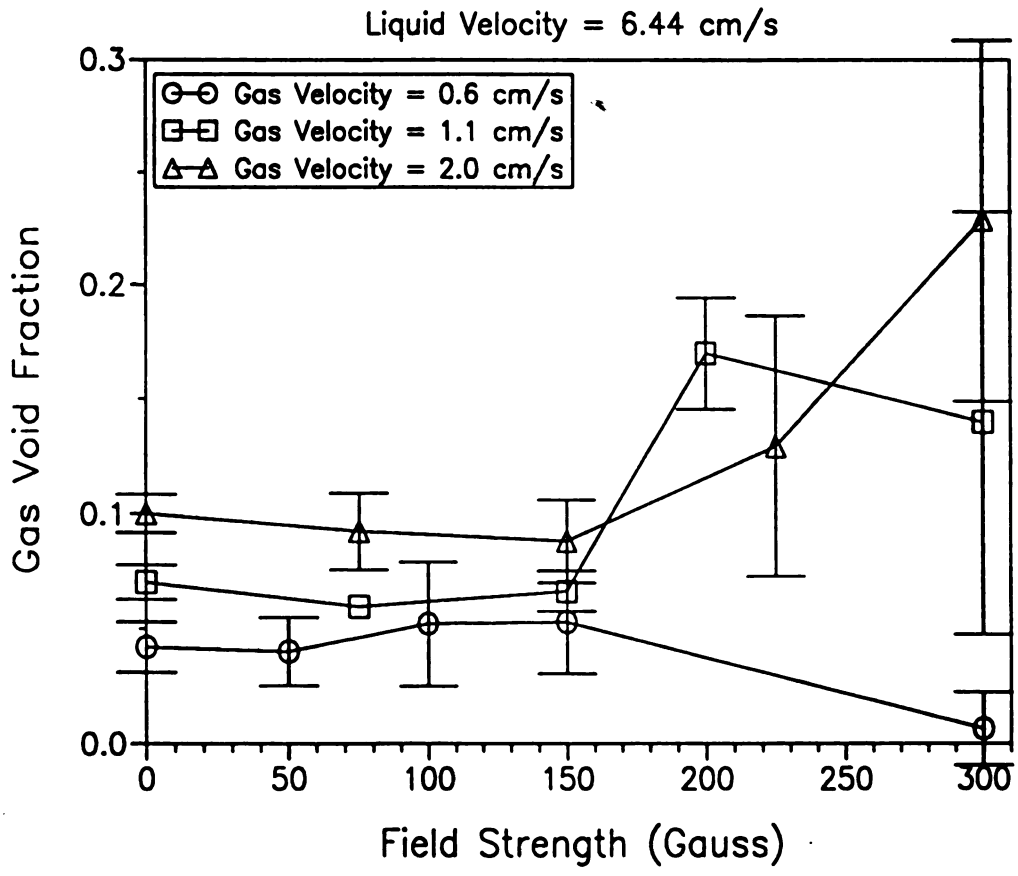

Figure 5-11 95% Confidence Intervals for Gas Void Fraction Data in Figure 5-8

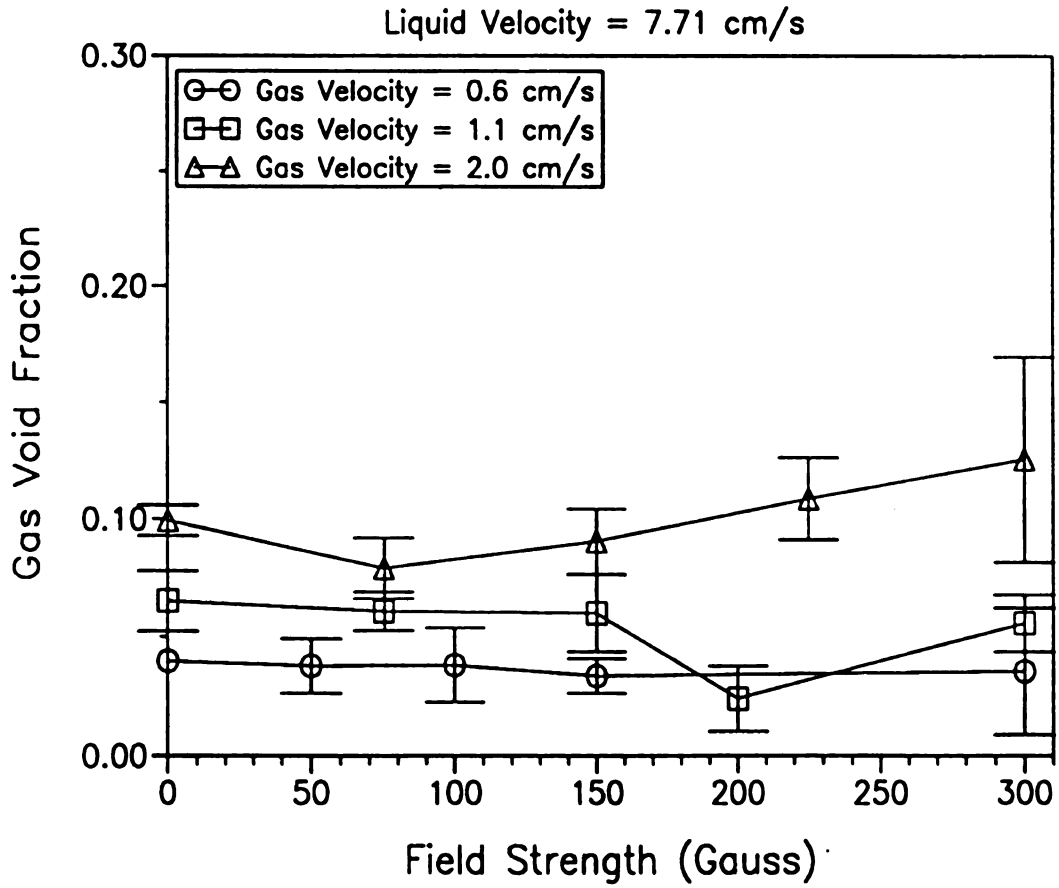

Figure 5-12 95% Confidence Intervals for Gas Void Fraction Data in Figure 5-9

increases with field strength for the two higher gas velocities, but decreases slightly for the lowest gas velocity. The gas void fraction for 1.1 cm/s is higher than the void fraction for 2.0 cm/s at the highest field strength of 300 gauss. Both the decrease in void fraction at the lowest gas velocity and the increase in void fraction at the higher two gas velocities occur in the frozen regime. The 95% confidence intervals indicate much greater variation in the data at high field strengths.

Figure 5-8 shows similar trends for a liquid flow rate of 6.44 cm/s. The gas void fraction increases for gas velocities of 1.1 and 2.0 cm/s and decreases for a gas velocity of 0.6 cm/s. Also, the scatter in the data increases with magnetic field strength. The gas void fraction is higher for a gas velocity of 1.1 cm/s at a field strength of 200 gauss than for a gas velocity of 2.0 cm/s. However, for this liquid velocity, the increase in void fraction for the two higher gas velocities occurs in the channel regime rather than the frozen regime. The decrease in gas void fraction at the lowest gas velocity does occur in the frozen regime though.

Figure 5-9 shows that for a gas velocity of 2.0 cm/s there is a slight increase in void fraction with magnetic field strength but no effect of magnetic field strength for gas velocities of 1.1 and 0.6 cm/s. In this case, the confidence intervals are unaffected by field strength.

A comparison of the gas void fraction measured with the valve technique (average measurement) to the void fraction measured with the optical probe (local measurement) is shown in Figure 5-13 for a magnetic field strength of 0 and 275 gauss. There is a strong

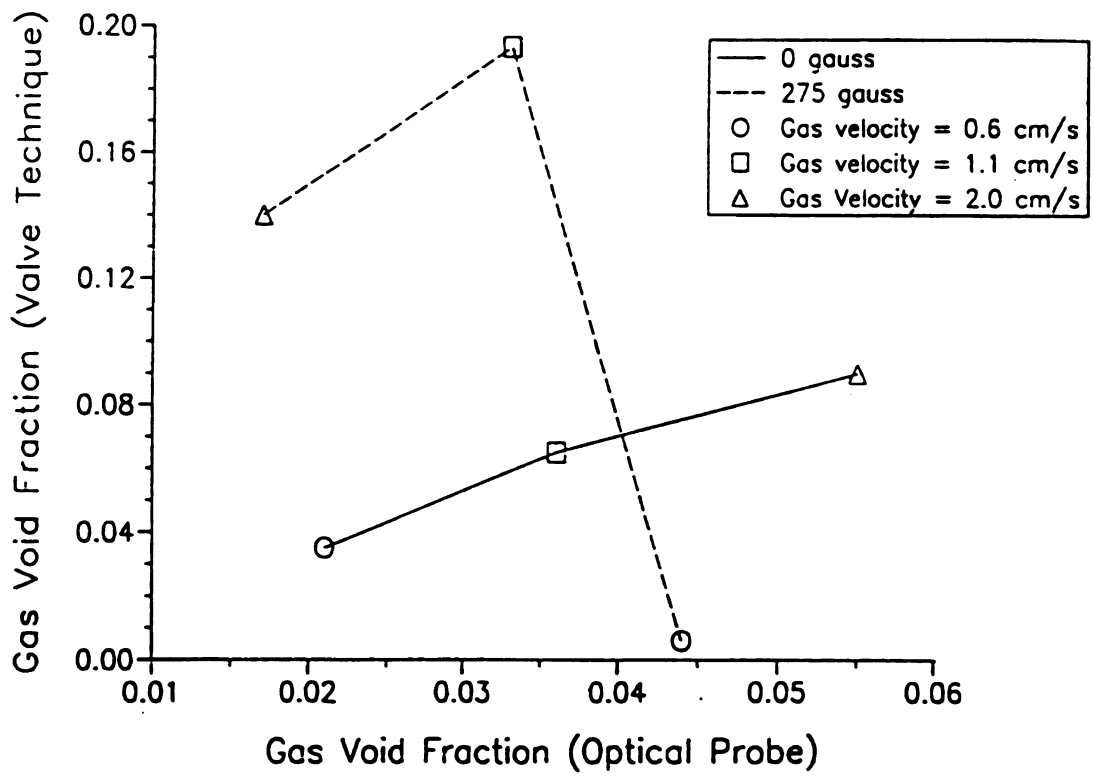

Figure 5-13 Comparison of the Valve Technique and the Optical Probe Technique for Field Strengths of 0 and 275 Gauss

correlation between the two methods for zero magnetic field, while there is essentially no correlation at the high field strength. Since the high field strength corresponds to the frozen regime, this finding suggests that local void fraction measurements do not accurately reflect the average void fraction when there are preferential channels for bubble migration.

5.4 Liquid Dispersion

5.4.1 Conductivity Probe Performance

Care was taken to make the two conductivity probes as identical as possible, and the initial calibration curves (probe output voltage versus tracer concentration) for the probes were found to be identical. In addition, the calibration curves were linear over the range from 0 to 10 g/L with a correlation coefficient of 0.999. Figure 5-14 shows the output from both probes during a typical tracer run. After several days of operation, the probe surfaces corroded significantly, and a loss of signal was noticed. The probes were regenerated by grinding off the corrosion. However, this procedure affected the probe response, so it was necessary to recalibrate the probes after regeneration.

5.4.2 Diffusion Coefficients

Diffusion coefficients were determined as described in Section 3.4.3. Equation 3-14 was fit to the experimentally measured diffusion data by both a one and two parameter fit. In the one parameter fit, the diffusion coefficient was varied until the mean square error between the model and the experimental data was minimized, and in the two parameter fit, both the diffusion coefficient and the parameter α were optimized simultaneously. As

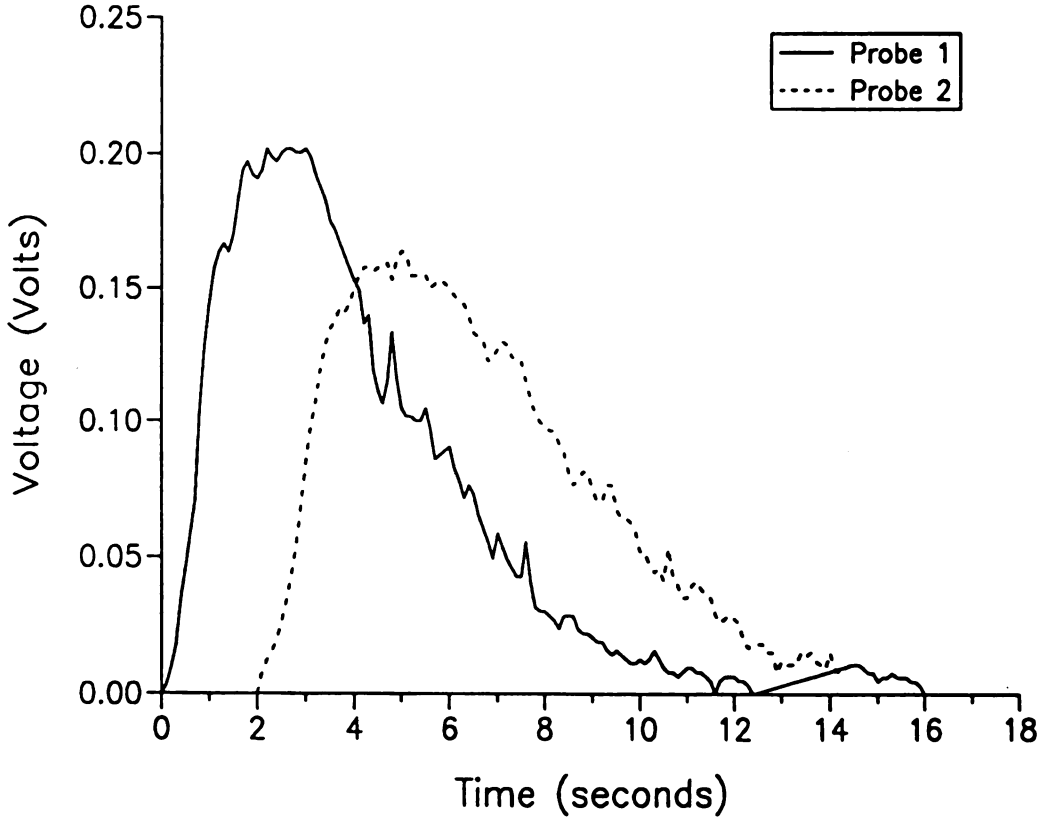

Figure 5-14 Experimental Data from Conductivity Probes in a Tracer Experiment

shown in Figure 5-15, the two parameter approach gave a much better fit. As described in Chapter 6, two parameters are needed to account for the volume of the beads obstructed by the magnetite.

One assumption made in developing the model used to calculate diffusion coefficients was that film mass transfer resistance was negligible. An experiment was conducted to determine the conditions under which this assumption was valid. Figure 5-16 shows the effect of agitation rate on the apparent diffusion coefficient. The measured coefficient increased with agitation rate up to about 100 rpm. Table 5-1 shows the values of the diffusion coefficient and the parameter α that best fit Equation 3-14 to the experimental data for alginate beads containing 0, 5, and 50% by weight magnetite. The effective diffusion coefficient decreased with increasing magnetite concentration, while the parameter α increased with increasing magnetite concentration.

5.4.3 Pore Volume Distributions

Figure 5-17 shows the void volume distributions of alginate beads containing 0, 5, and 50% by weight magnetite. Table 5-2 lists the empirical constants used to fit Equations 3-22 and 3-23 to these data. The asymptotic values of the curves, which correspond to the total void volume of the solid, decrease as the percentage of magnetite increases. From these data, the bead porosity may be determined as a function of the tracer diameter by finding the difference between the asymptotic value of the curve and the excluded void volume for the particular molecular diameter. Figure 5-18a shows a plot of the bead porosity as a function of the diameter of the diffusing molecule. The 0, 5, and 50% magnetite beads have

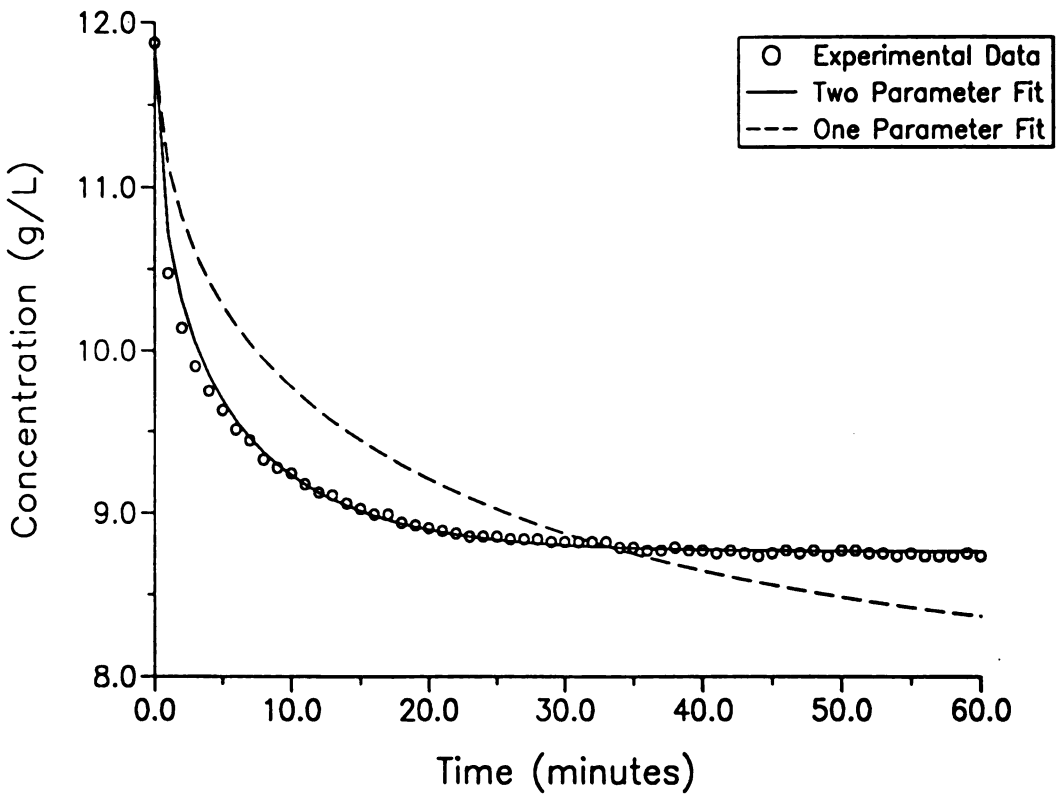

Figure 5-15 Experimental Diffusion Data with One and Two Parameter Fits

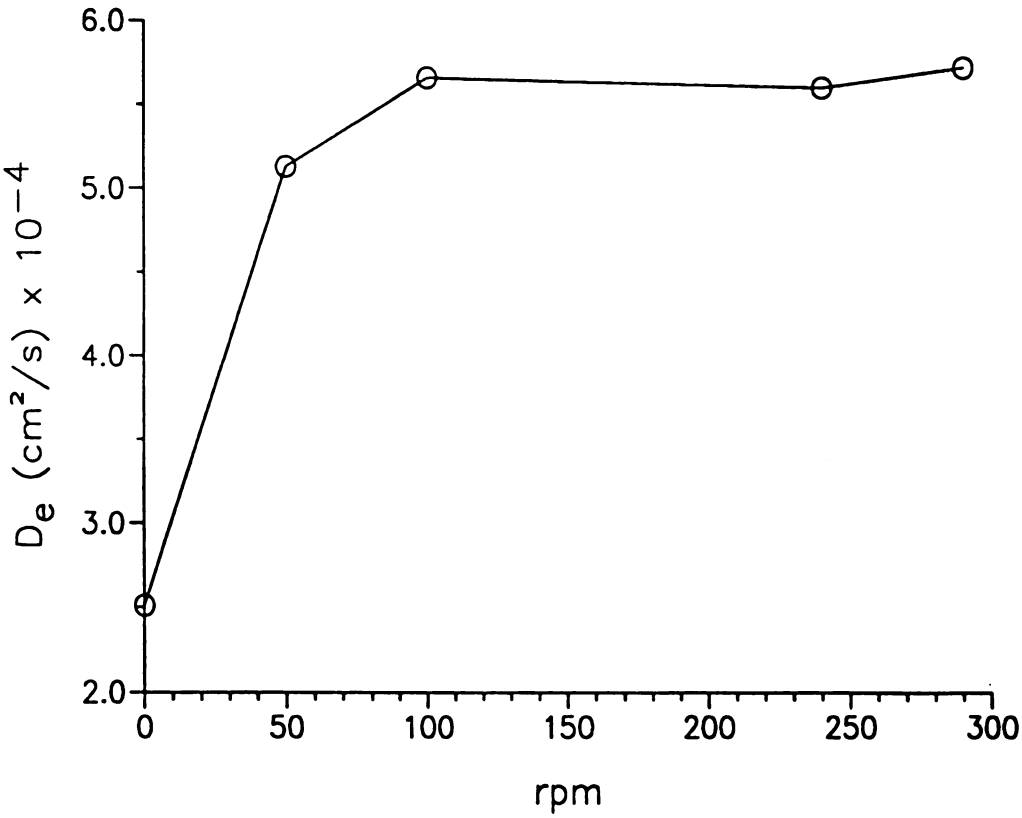

Figure 5-16 Effect of Agitation Rate on Measured Diffusion Coefficient

Table 5-1 Values of D_e and α from Curve Fits of Experimental Data

% Magnetite	Diffusion Coefficient (cm^2/s)	α
0	5.40×10^{-4}	2.23
5	5.41×10^{-4}	2.26
50	4.30×10^{-4}	2.55

Table 5-2 Curve Fits for Pore Size Distributions

% Magnetite	A_0	A_1	A_2	A_3	A_4	M.S.E.
0	0.94	3.33	1.82	0.015	0.03	0.000588
5	0.82	3.59	1.71	0.030	0.02	0.000216
50	0.50	3.56	1.52	0.059	0.015	0.000175

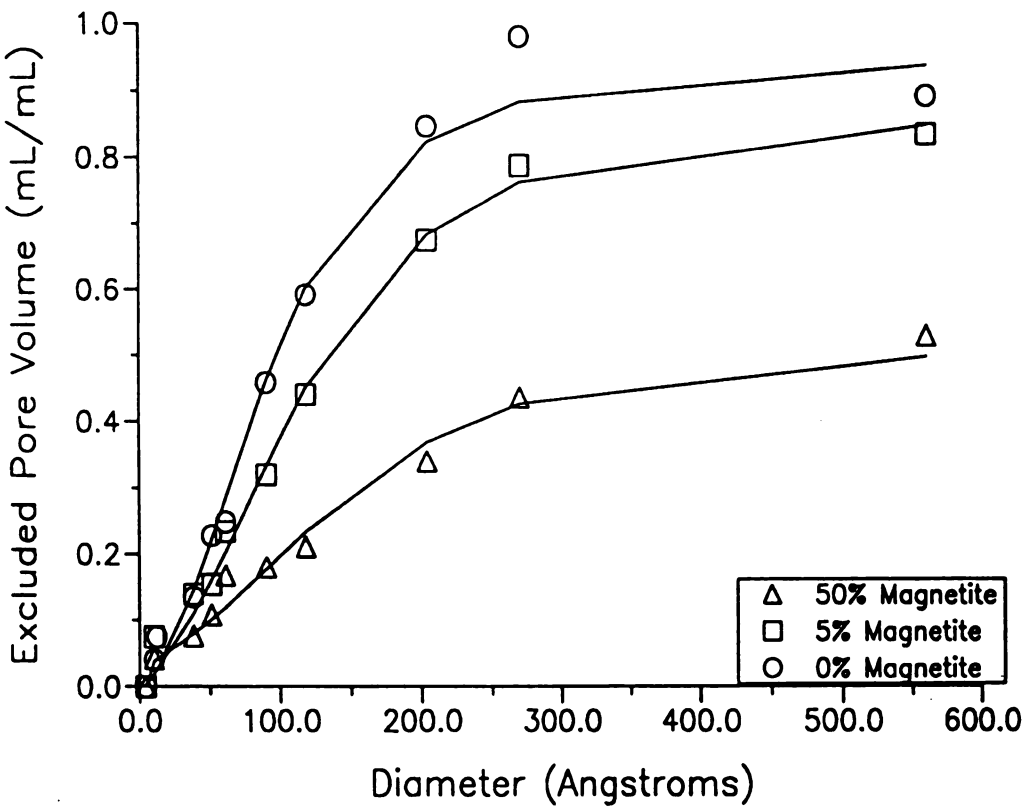

Figure 5-17 Pore Size Distributions and Curve Fits for 0, 5, and 50% by Weight Magnetite Alginate Beads

a.)

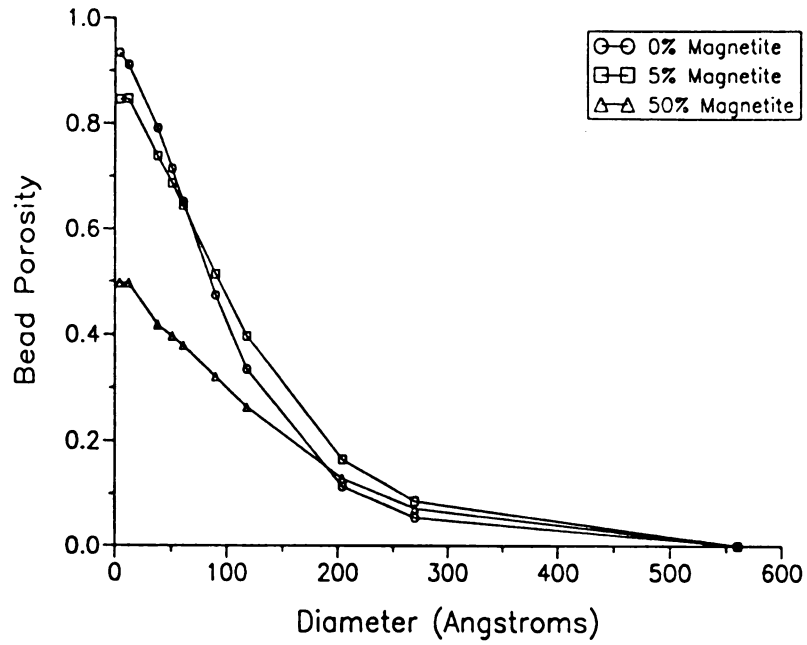

b.)

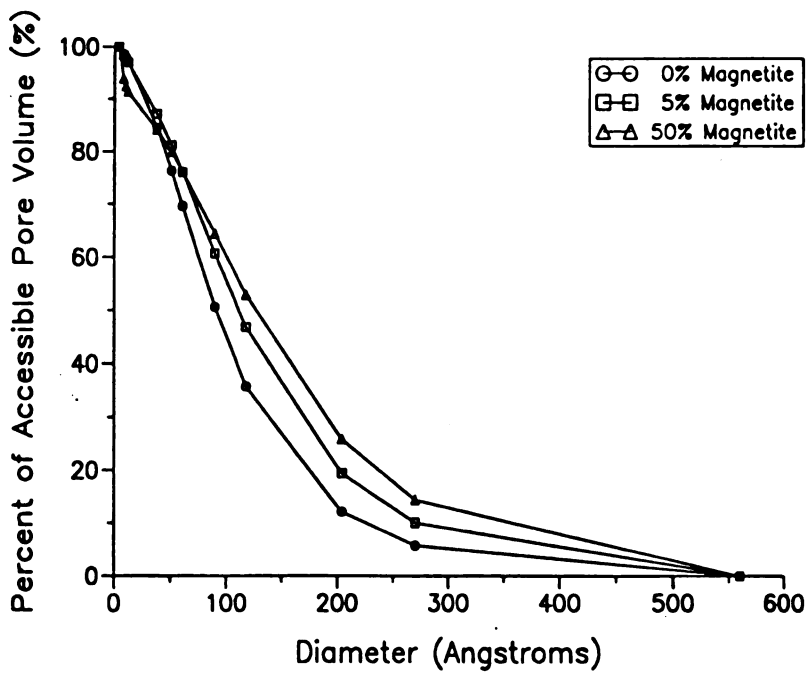

Figure 5-18 a). Bead Porosities for 0, 5, and 50% by Weight Magnetite Alginate Beads versus Molecular Diameter

b). Percentage of Total Accessible Bead Volume Available for Diffusion versus Molecular Diameter

approximately 93%, 83%, and 50%, respectively of their volume accessible to molecules with diameters of 10 Å (the approximate diameter of the calcium chloride tracer in solution as described in Chapter 6). Figure 5-18b shows a plot of the percentage of total accessible bead volume as a function of molecular diameter of the diffusing molecule. The percentage of total accessible bead volume is calculated by dividing the bead porosity by the asymptotic value of the curve.

5.4.4 Dispersion Coefficients

Predicted tracer profiles were calculated as described in Section 3.4.2 by fitting both the dispersion coefficient and the interstitial velocity to the experimental data. The predicted and experimental tracer concentration curves are compared in Figure 5-19 for a typical run. Figure 5-20 compares the Peclet numbers (U_iR/D_{ax}) calculated both neglecting intraparticle diffusion (Equation 3-8) and including it (Equations 3-9 and 3-10). Peclet numbers calculated including the effect of diffusion are higher (thus dispersion coefficients are lower) than when diffusion is ignored, indicating that diffusion contributes to spreading of the tracer curves. Figures 5-21 to 5-23 show the effects of magnetic field strength and gas velocity on the measured Peclet number for liquid velocities of 5.15, 6.44, and 7.71 cm/s, respectively. For the lowest liquid velocity (Figure 5-21), there was a sharp increase in Peclet number at 100 gauss for a gas velocity of 0.6 cm/s, and smaller increases at 150 gauss for a gas velocity of 1.1 cm/s and at 75 gauss for a gas velocity of 2.0 cm/s. The Peclet number curves peaked at the boundary of the chain-channel and destabilized regimes for gas

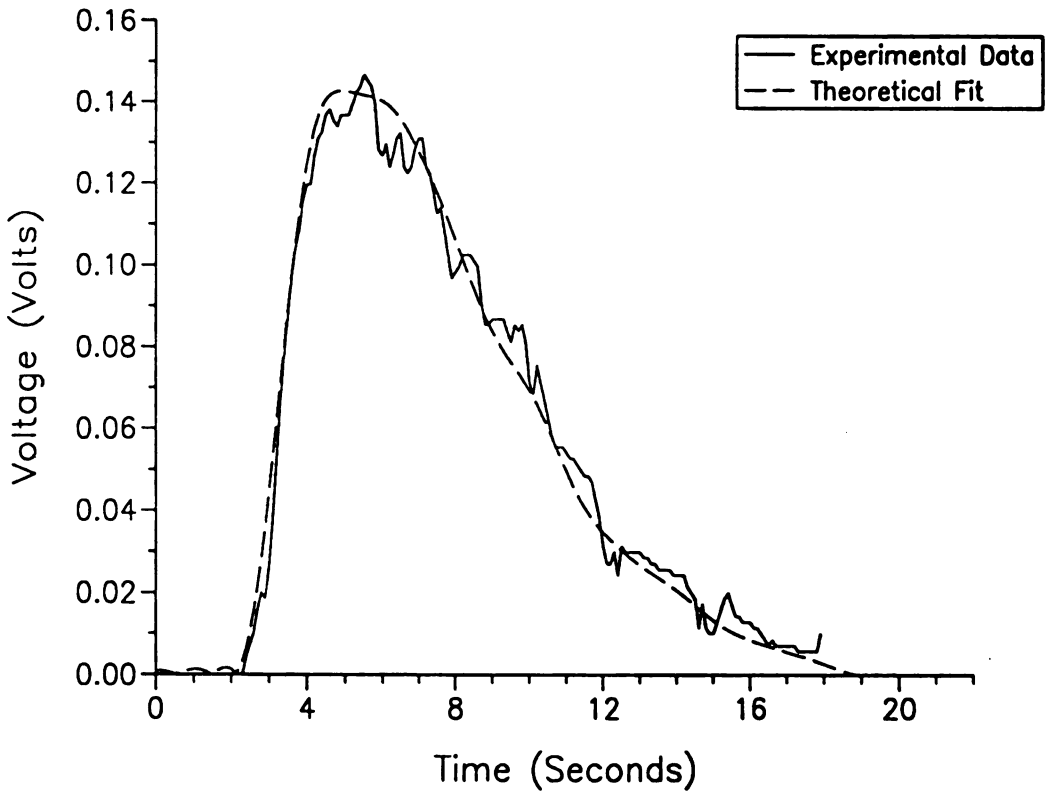

Figure 5-19 Theoretical Fit of Experimental Tracer Data

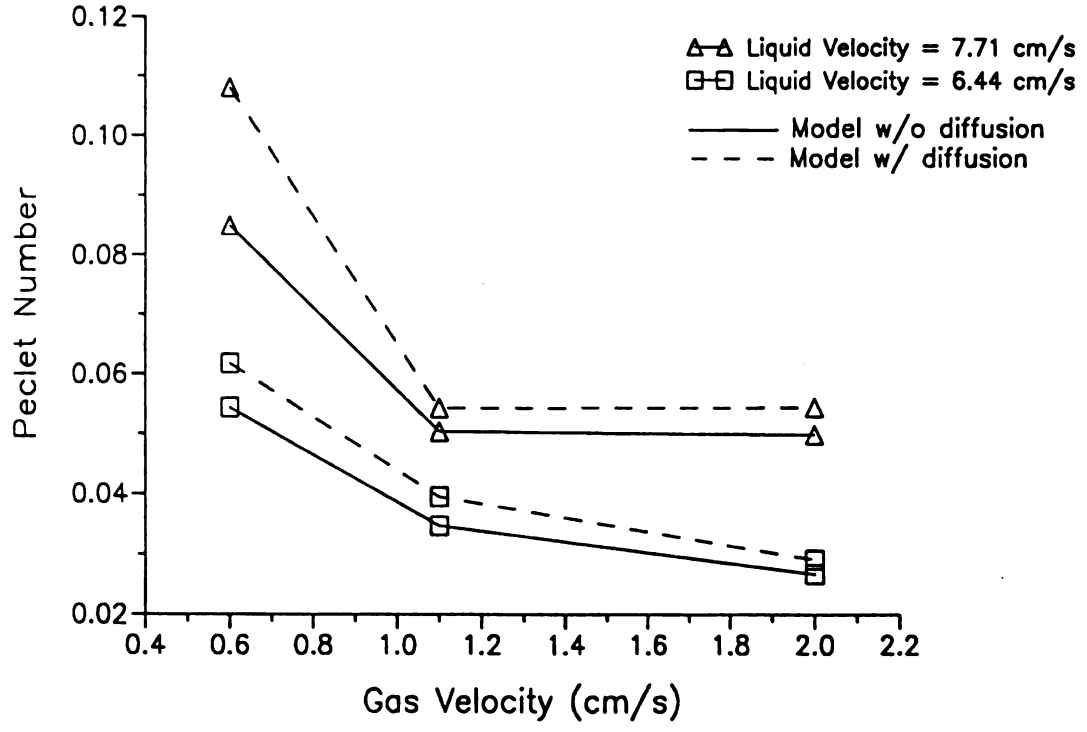

Figure 5-20 Comparison of Peclet Numbers Calculated From Dispersion Models with and without the Effect of Tracer Diffusion Included

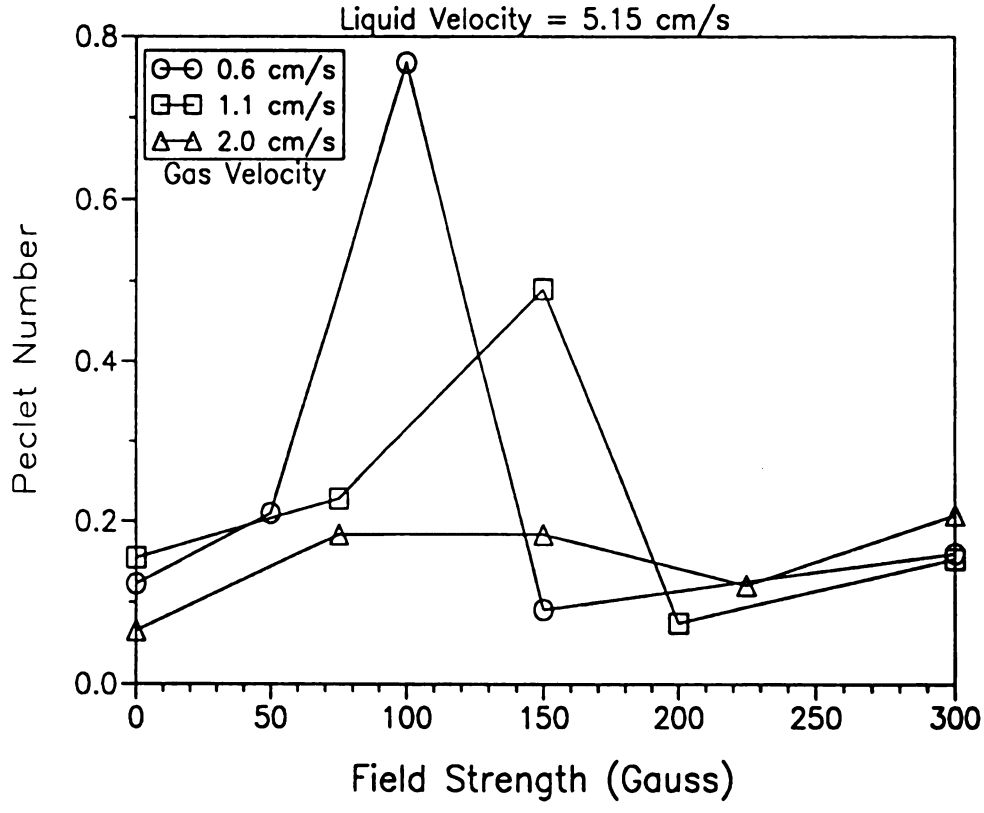

Figure 5-21 Peclet Numbers as a Function of Magnetic Field Strength for a Liquid Velocity of 5.15 cm/s and Gas Velocities of 0.6, 1.1, and 2.0 cm/s

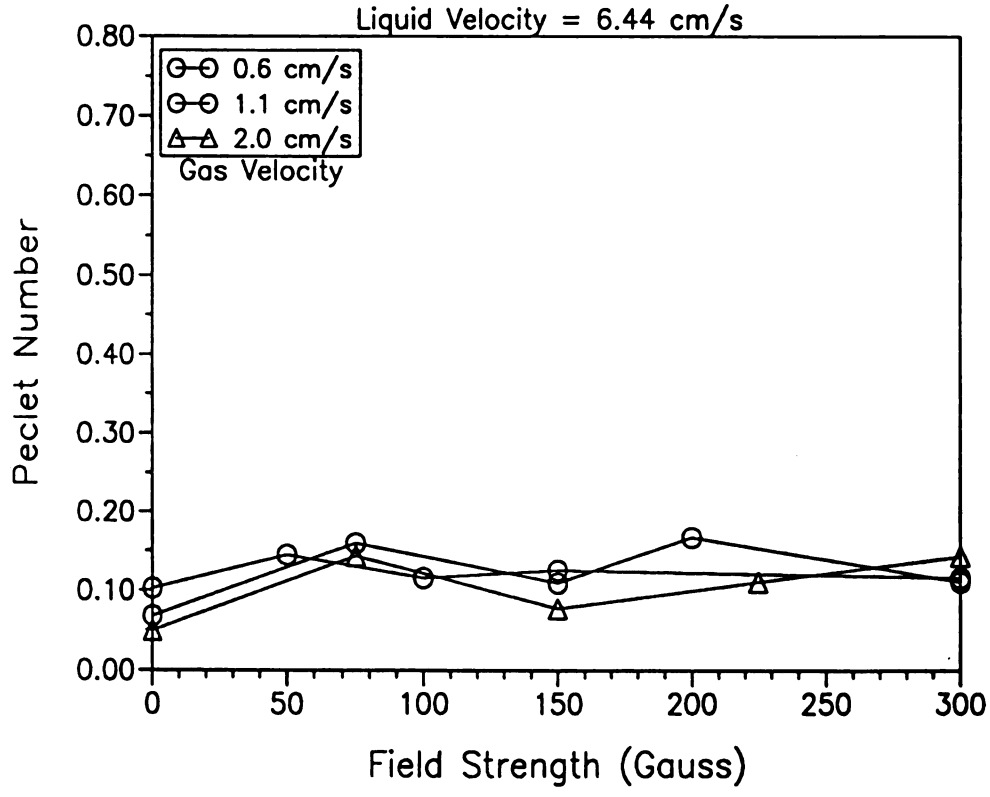

Figure 5-22 Peclet Numbers as a Function of Magnetic Field Strength for a Liquid Velocity of 6.44 cm/s and Gas Velocities of 0.6, 1.1, and 2.0 cm/s

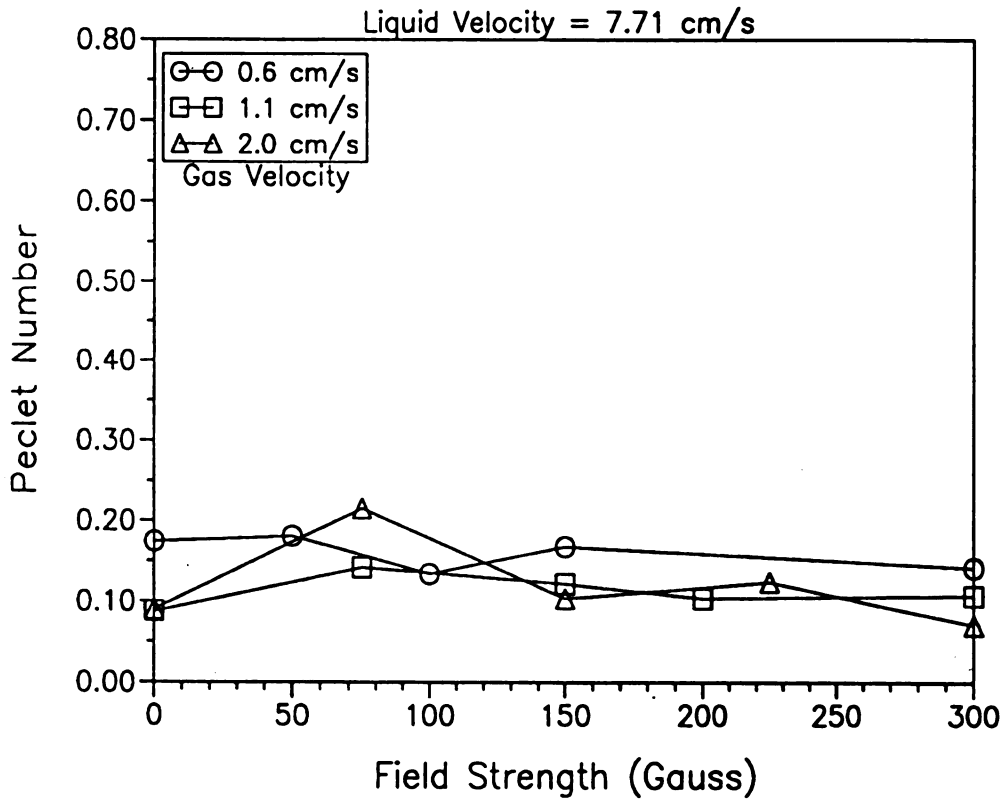

Figure 5-23 Peclet Numbers as a Function of Magnetic Field Strength for a Liquid Velocity of 7.71 cm/s and Gas Velocities of 0.6, 1.1, and 2.0 cm/s

velocities of 0.6 and 2.0 cm/s, and in the channel regime for a gas velocity of 1.1 cm/s. Figures 5-22 and 5-23 show that neither magnetic field strength nor gas velocity significantly affected Peclet number for the two higher liquid velocities. Figures 5-24 to 5-26, which show the 95% confidence intervals for the data shown in Figures 5-21 to 5-23 respectively, indicate that reproducibility was least for field strengths between 50 and 150 gauss, where the decrease in mixing was observed. Regardless, the increases in Peclet number for gas velocities of 0.6 and 1.1 cm/s, in Figure 5-21 were shown to be statistically valid using a two level analysis of variance[94]. Thus, magnetization can significantly reduce axial mixing in three-phase fluidized beds.

5.5 Gas to Liquid Mass Transfer

The agreement between the predicted and experimental oxygen concentration profiles was excellent, as is shown in Figure 5-27. A one parameter fit (the overall mass transfer coefficient, k_La) of Equations 3-36 to 3-41 was used along with the dispersion coefficient data from Section 5-4. Figures 5-28 to 5-30 show the effect of magnetic field strength and gas velocity on the overall mass transfer coefficient for liquid velocities of 5.15, 6.44, and 7.71 cm/s, respectively. Figure 5-28 shows that k_La peaked at approximately 75 gauss for all gas velocities, but the peak was most pronounced for the highest gas velocity. All of the peaks occurred in the chain-channel regime. As shown in Figure 5-29, there was no effect of magnetic field strength on k_La for the intermediate liquid velocity. However, Figure 5-30 shows that there was again an effect of field strength at the highest liquid velocity for gas velocities of 1.1 and

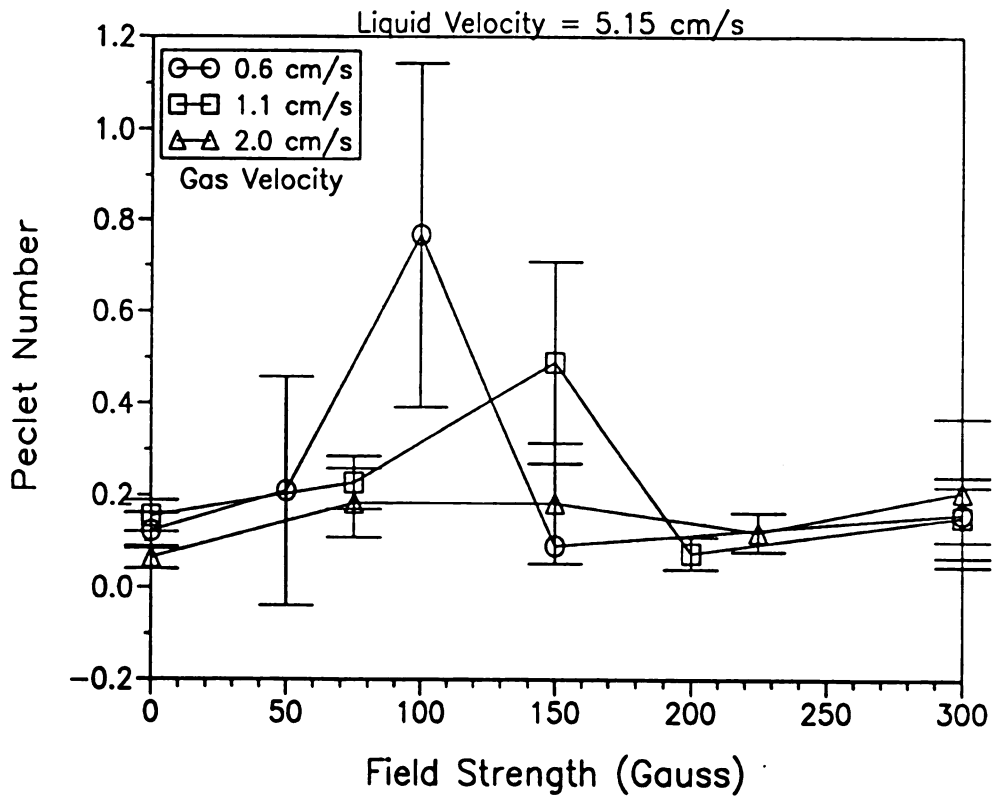

Figure 5-24 95% Confidence Intervals for Peclet Number Data in Figure 5-21

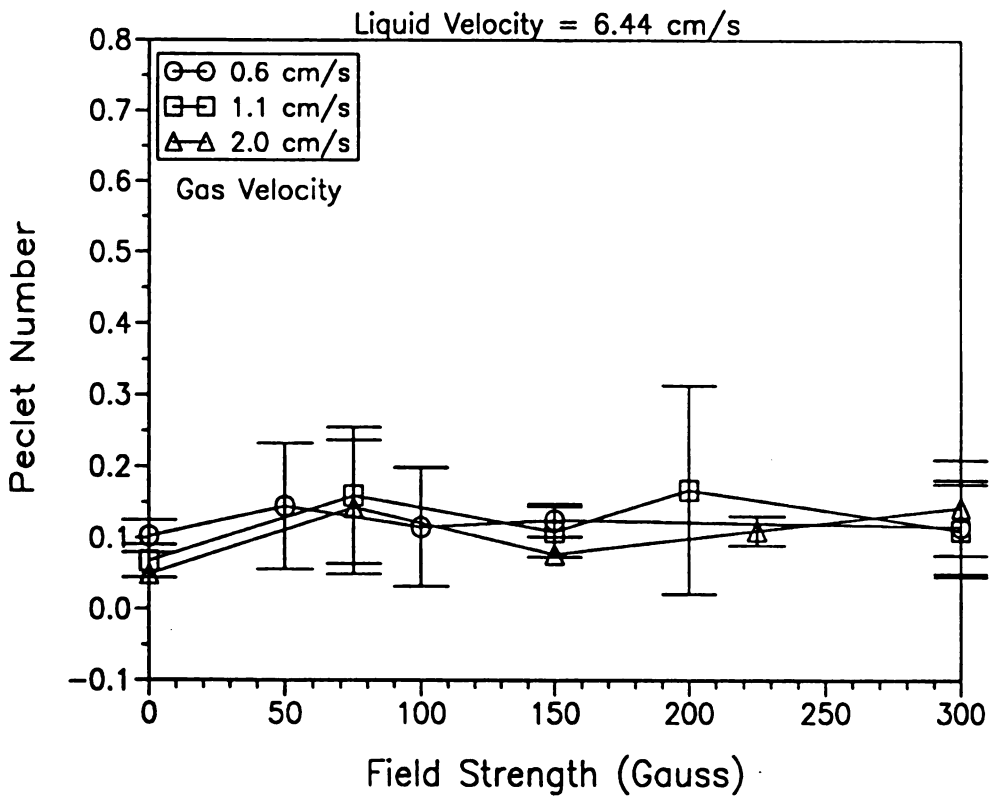

Figure 5-25 95% Confidence Intervals for Peclet Number Data in Figure 5-22

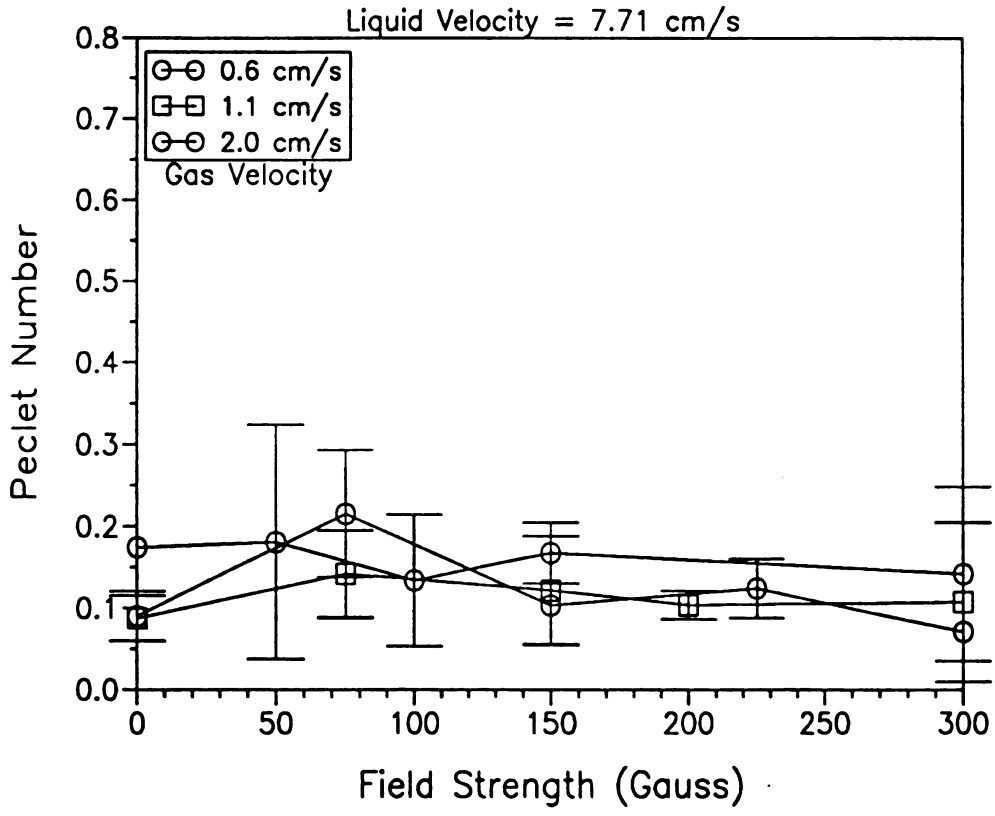

Figure 5-26 95% Confidence Intervals for Peclet Number Data in Figure 5-23

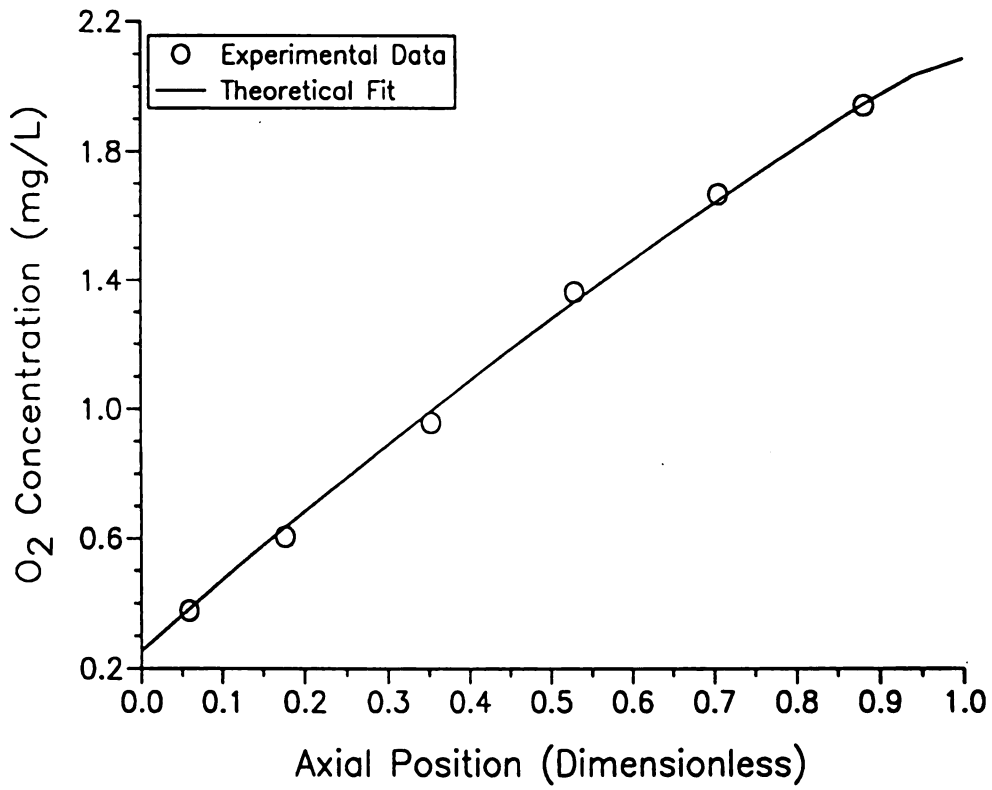

Figure 5-27 Experimental and Theoretical Oxygen Profiles

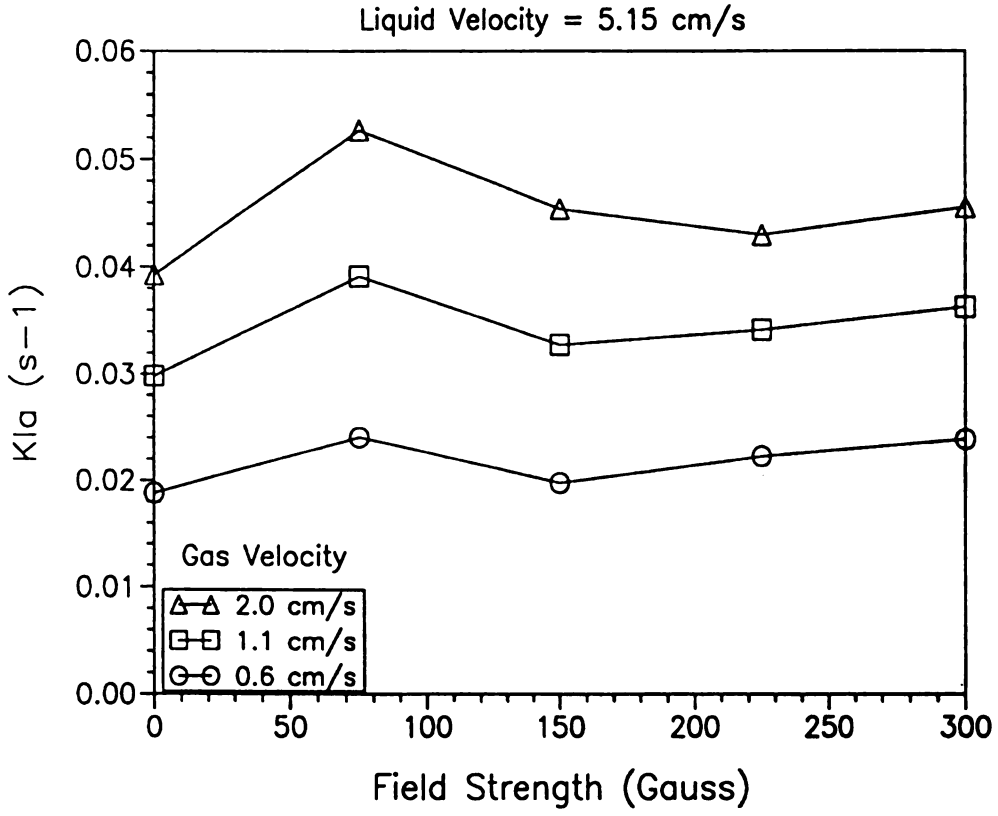

Figure 5-28 **Mass Transfer Coefficients as a function of Magnetic Field Strength for a Liquid Velocity of 5.15 cm/s and Gas Velocities of 0.6, 1.1, and 2.0 cm/s**

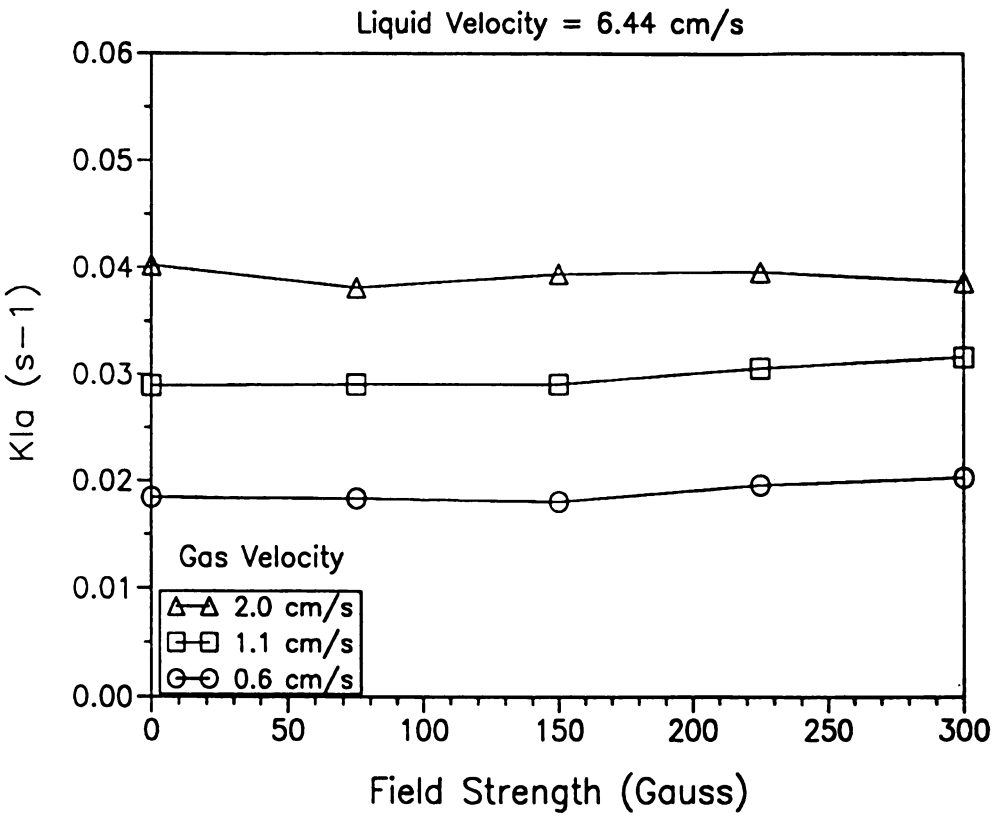

Figure 5-29 **Mass Transfer Coefficients as a function of Magnetic Field Strength for a Liquid Velocity of 6.44 cm/s and Gas Velocities of 0.6, 1.1, and 2.0 cm/s**

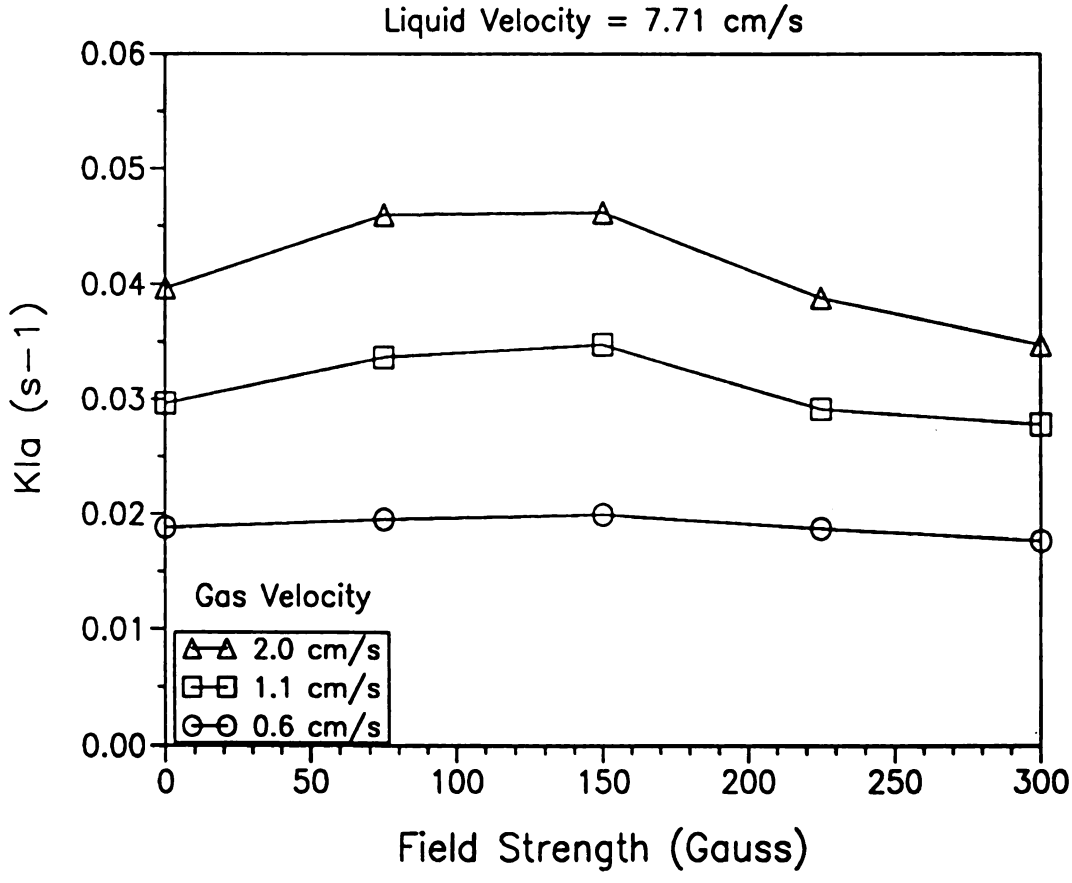

Figure 5-30 **Mass Transfer Coefficients as a function of Magnetic Field Strength for a Liquid Velocity of 7.71 cm/s and Gas Velocities of 0.6, 1.1, and 2.0 cm/s**

2.0 cm/s, although the effect was not as pronounced as those in Figure 5-28. The maximum k_La values occurred in the chain-channel and the destabilized regimes for this liquid velocity. Figures 5-31 to 5-33, which show the 95% confidence intervals for these data, indicate that the reproducibility of the oxygen mass transfer coefficients was much greater than for the gas void fraction and liquid dispersion measurements.

5.6 Dimensional Analysis of the Fluidized Bed Model

Dimensional analysis was used to correlate the model results using dimensionless groups of the important variables of the system. These variables are L, the distance between measuring points; R, the particle radius; U, the superficial liquid velocity; D_e, the diffusion coefficient; and D_{ax}, the dispersion coefficient. The particle porosity (ϵ_p), and the liquid void fraction (ϵ_L) were also included, but they are already dimensionless. Since it was not known what dimensionless groups would be important, all possible types of dimensionless groups were determined. The resulting dimensionless groups are listed in Equation 5-1

$$\frac{R}{L} \quad \frac{D_e}{D_{ax}} \quad \frac{RU}{D_{ax}} \quad \frac{RU}{D_e} \quad \frac{LU}{D_{ax}} \quad \frac{LU}{D_e} \quad \frac{\epsilon_L}{\epsilon_p} \tag{5-1}$$

It was hypothesized that all values of the parameters could be graphically correlated as a function of two independent dimensionless groups. One criterion for the dimensionless groups was that they contain all the above variables, with the exception of L, because the liquid dispersion coefficient should not be a function of the distance between the measuring points. The variable L was

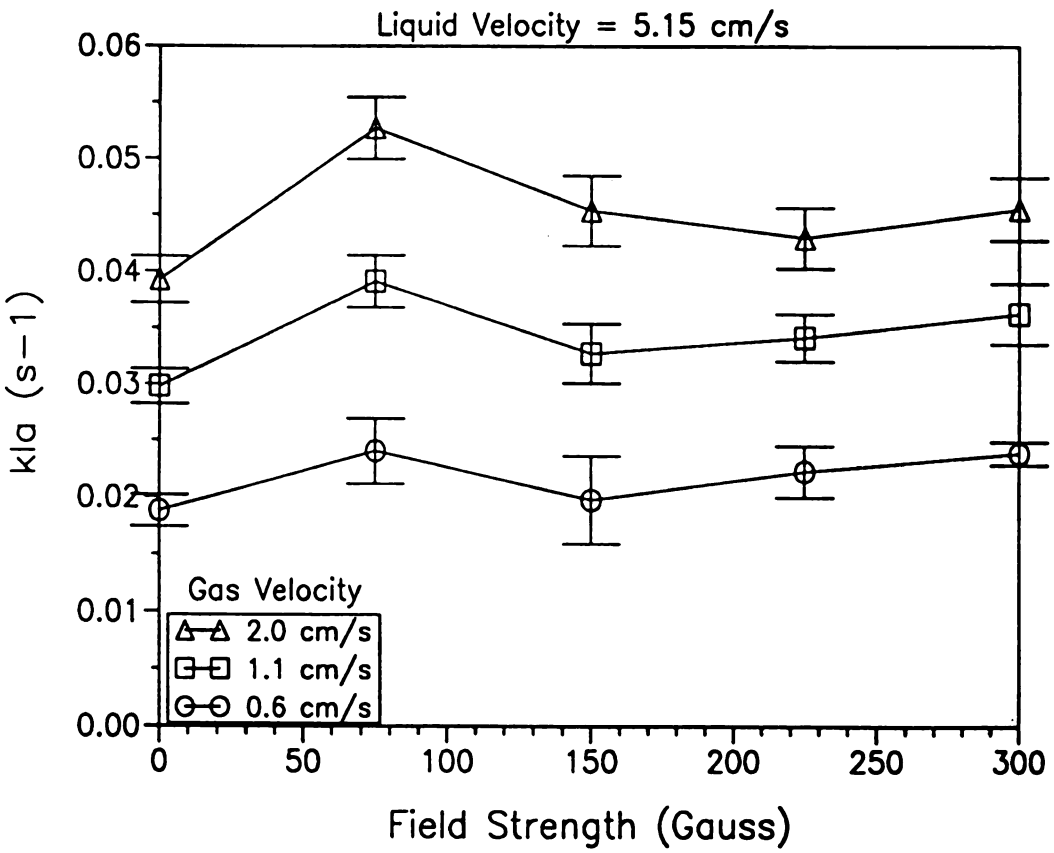

Figure 5-31 95% Confidence for Mass Transfer Coefficients in Figure 5-28

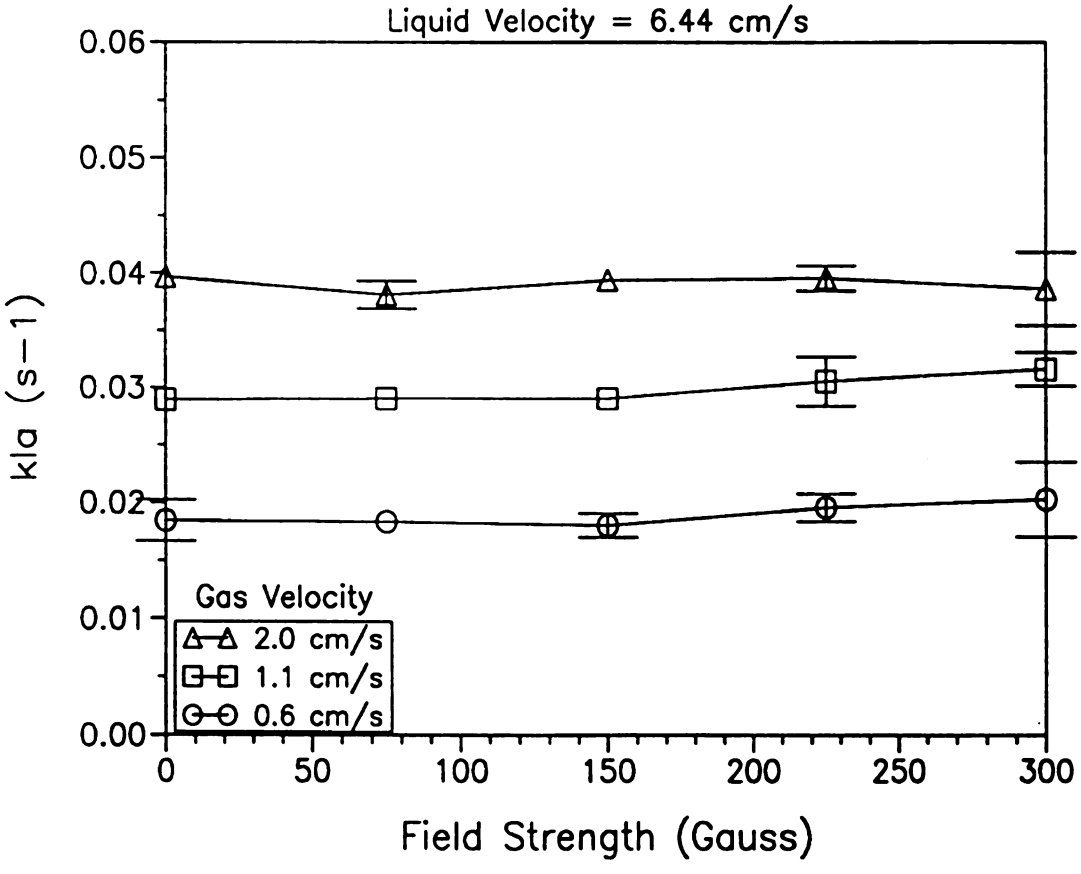

Figure 5-32 95% Confidence for Mass Transfer Coefficients in Figure 5-29

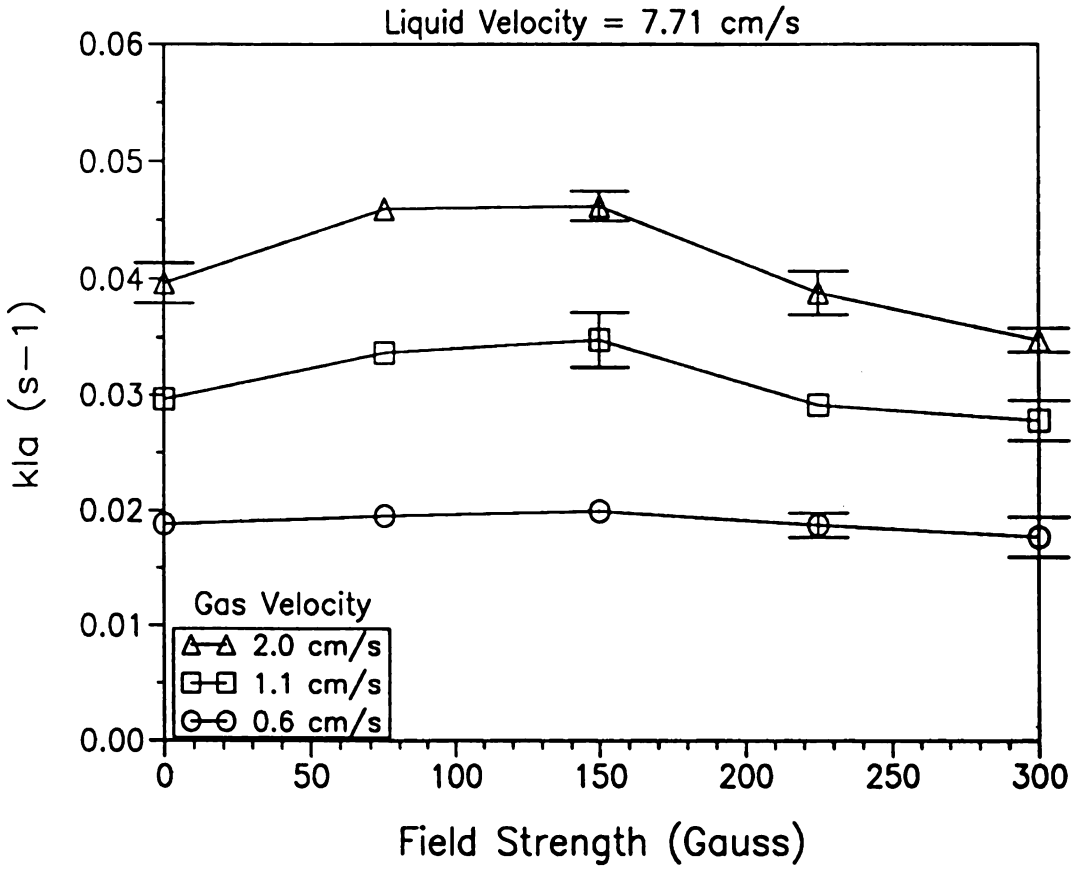

Figure 5-33 95% Confidence for Mass Transfer Coefficients in Figure 5-30

still considered important in the analysis, since it was required to non-dimensionalize the variable R. Examination of the dimensionless groups in Equation 5-1 shows that at least four of these groups are needed to include all of the variables. The number of possible permutations of the dimensionless groups in Equation 5-1 is 35. Fifteen of the 35 possibilities resulted in L not cancelling out, and were eliminated from consideration. The correction factor (η), the ratio of the true axial dispersion coefficient to the apparent one, was calculated for each of the parametric studies described in Chapter 3 and plotted versus each of the remaining 20 possibilities. Within each possibility there were additional 16 combinations since the reciprocal of each dimensionless group in Equation 5-1 could also be used. Two dimensionless groups (Φ and Pe) were found that could correlate all the parametric studies. Using the Peclet number based on the column length a family of curves was obtained. The definitions of Φ and the Peclet number are given in Equation 5-2.

$$\Phi = \frac{D_e D_{ax,app} \varepsilon_p^2 (1-\varepsilon_I)^2}{R^2 U^2} \qquad Pe = \frac{L_C U}{D_{ax}} \tag{5-2}$$

The correction factor η is plotted versus the dimensionless group Φ in Figure 5-34. The usefulness of this plot was limited since the Peclet number contains the true dispersion coefficient, which cannot be obtained without solving the mathematical model that includes the effects of intraparticle diffusion (Equations 3-9 and 3-10). By contrast, the apparent dispersion coefficient can be simply calculated using Equation 3-8. Although an iterative method could be used to obtain an estimate of the true disperison coefficient from

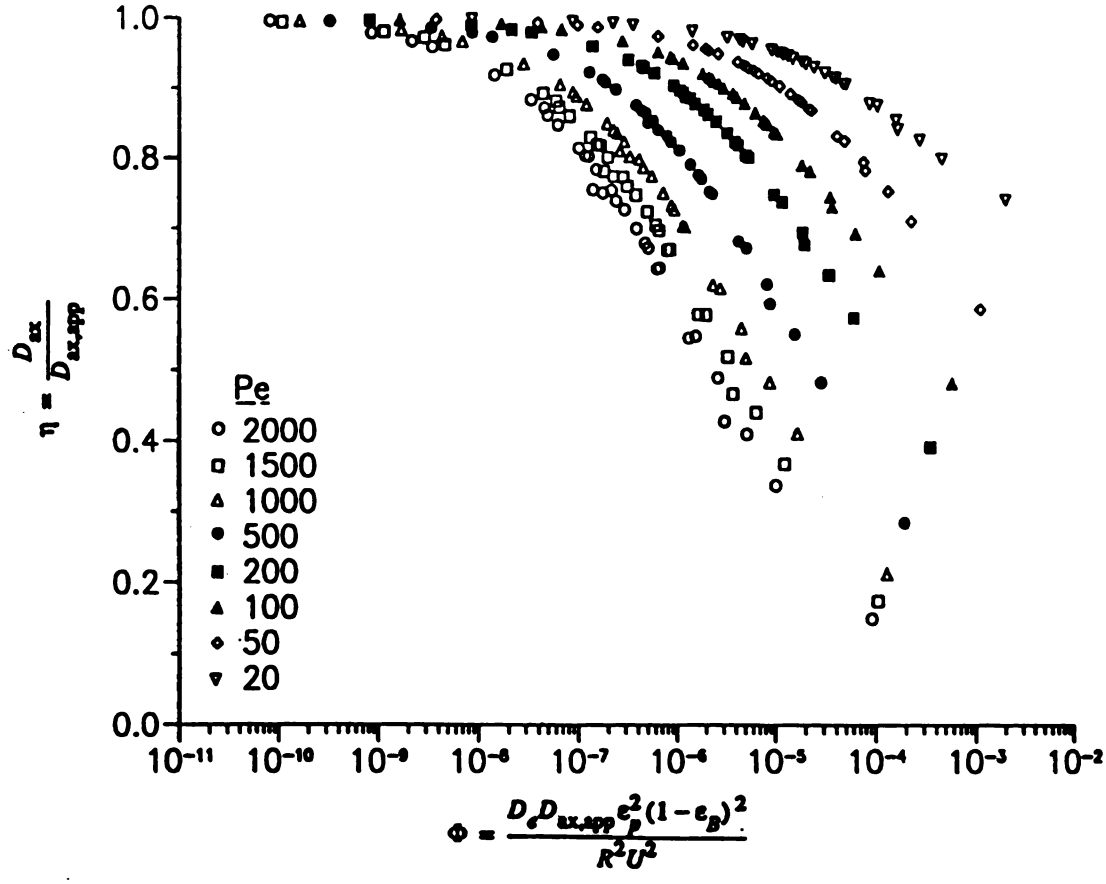

Figure 5-34 Correction Factor, η, versus ϕ as a function of Pe_{true}

the apparent value, this method is time consuming. Thus, for simplicity, the results were cast in terms of the measurable variables, Pe_{app} and Φ, which are defined in Equation 5-3.

$$\Phi_{app}=\frac{D_e D_{ax,app} \epsilon_p^2 (1-\epsilon_l)^2}{R^2 U^2} \qquad Pe_{app}=\frac{L_C U}{D_{ax,app}} \tag{5-3}$$

Unfortunately, the families of curves shown in Figure 5-34 do not map directly into these new coordinates (Pe_{app}, Φ). To correlate the results, each value of η was tabulated as a function of Φ and Pe_{app}, thus generating a three-dimensional surface, $\eta(\Phi, Pe_{app})$. This surface was then curve fit using the empirical expression shown in Equation 5-4.

$$\eta = a_0 + a_1 x + a_2 z + a_3 x^2 + a_4 z^2 + a_5 xz + a_6 \sqrt{z} + a_7 x^3 + a_8 x^2 z + a_9 x^2 \sqrt{z} + a_{10} x \sqrt{z}$$
$$x=\log_{10}\Phi \qquad z=\frac{Pe_{ax,app}}{1000} \tag{5-4}$$

Table 5-3 shows the empirical constants obtained in the fit. The form of this expression was varied by trial and error until the average deviation of the empirical fit from the data points was less than 5%. For the equation given in Equation 5-4 the average deviation was 1.5%. Isocurves showing η as a function of Φ for constant values of Pe_{app} were then calculated from Equation 5-3 for different values of Pe_{app}.

Figure 5-35 shows the family of isocurves. Figure 5-36 shows the effect of the parameters on the correction factor. Particle radius appears to have the strongest affect, and the diffusion coefficient also has a strong effect.

Table 5-3 Curve Fit of η versus ϕ Data

Constant	Value
A_1	.09429
A_2	-.6706
A_3	3.327
A_4	-.1337
A_5	.0493
A_6	1.026
A_7	-9.962
A_8	-.00789
A_9	.0717
A_{10}	-.1760
A_{11}	-2.688

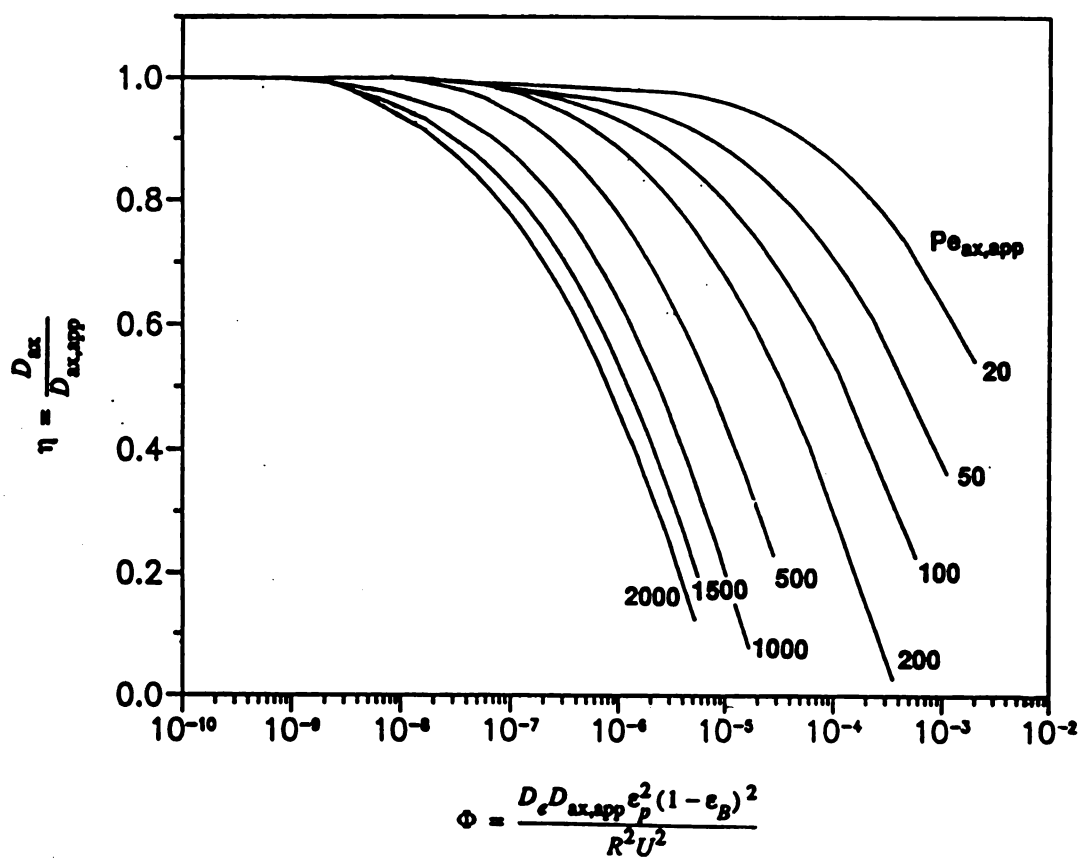

Figure 5-35 Correction Factor, η, versus ϕ_{app} as a Function of Pe_{app}

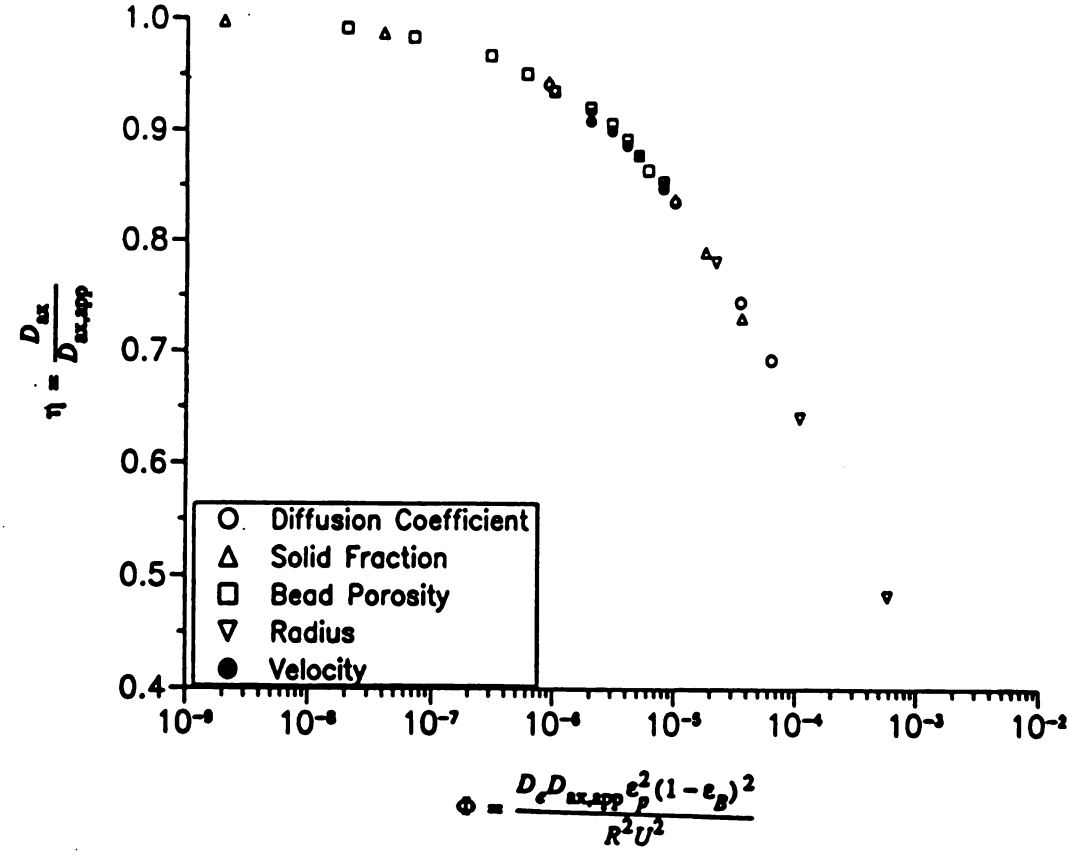

Figure 5-36 Effect of System Parameters on the Correction Factor, η

Chapter VI: Discussion

6.1 Bed Regimes

The unstabilized and frozen regimes observed in this study are comparable to the random and frozen regimes described by Rosensweig[29,30]; however, there was no regime in this study similar to the stabilized regime described by Rosensweig. His stabilized regime was characterized by both the absence of solids movement and an expanded fluidized bed. The chain regime observed in this study approached the stabilized state, but still had significant solids motion. Siegell[35] described an additional regime in his studies of a liquid-solid MSFB, the roll-cell regime, which was characterized by gulf streaming motion. None of the regimes found in this study resembled the roll-cell regime.

Hu and Wu[38] reported three bed regimes in a three phase MSFB: the particulate regime that exhibits behavior of an unmagnetized fluidized bed, the chain-fluidized bed where chains of particles form, and the magnetically aggregated bed where the particles aggregate into a single unit. The counterparts of these regimes found in this study are the random, chain, and frozen regimes, respectively. However, Hu and Wu make no mention of other bed regimes or the role that the gas phase plays in the formation of bed regimes. The results of this study indicate that the gas phase stongly influences the bed behavior. As will be discussed in later sections, observed changes in key bed properties as a function of magnetic field strength can often be correlated with transitions between bed regimes.

The observable behavioral differences in the bed regimes of the MSFB suggest that it may be possible to vary the properties of the MSFB markedly by simply changing the magnetic field strength. This would be valuable for processes with rapidly changing conditions, and for systems where many different processes are run in the same reactor.

6.2 Gas Void Fraction

For a liquid velocity of 5.15 cm/s, the onset of the frozen regime caused a substantial increase in local gas void fraction for gas velocities of 1.1 and 2.0 cm/s, but a decrease for a gas velocity of 0.6 cm/s. There was a wide variation among the five replicate measurements for the two higher gas velocities, with replicates varying from as high as 0.33 to as low at 0.001. This trend is consistent with the observation that the bubbles channel through preferred paths of reduced resistance within the frozen bed. When one of these paths intersected the probe tip, an artificially high void fraction was observed, whereas when the probe was bypassed, an artificially low value of void fraction was obtained. In the case of the lowest gas velocity, the frozen-bed void fraction was uniformly low in value. The low gas flow rate was probably inadequate to keep the channels open against the force of the applied magnetic field. This explanation agrees with the observation that bubbles appeared to flow around the bed under these conditions.

The data taken at a liquid velocity of 6.44 cm/s showed similar trends, except that the large increases in void fraction occurred in the channel regime rather than the frozen regime. This observation suggests that there is little difference between the physical behavior

of the channel and frozen regimes. The only observable difference between the two regimes was that the solid particles in the channel regime vibrated, while those in the frozen regime did not. Again, the frozen-bed void fraction was very low for the lowest gas velocity. For a liquid velocity of 7.71 cm/s, the modest increase in gas holdup observed at the highest gas velocity was again associated with the channel regime. However, in this case there was apparently no effect of magnetic field strength for gas velocities of 0.6 and 1.1 cm/s. It is not clear why the void fraction data for the highest liquid flow rate were so much different than those for the lower flow rates.

Qualitative observations of the MSFB revealed that the bubble size decreased as the magnetic field strength increased. Kwauk *et al.*[39] found that the bubble size in a three phase MSFB decreased exponentially with increasing field strength. As smaller bubbles exhibit lower rise velocities, this trend suggests that gas void fraction should increase with field strength. Although two and three fold increases in the local gas void fraction were observed in this study with application of the magnetic field, these results are questionable due to the point measurement technique used. Artificially high values were obtained when the probe happened to be in a bubble channel and low values were obtained otherwise. Moreover, the probe would not necessarily detect an increase in gas void fraction caused by entrapment of bubbles in the bed structure. Thus, point measurements of void fraction may not accurately reflect the radially averaged gas void fraction in the frozen and channel regimes. The comparison of values from the optical probe (point measurement) with measurements using the valve technique (average

measurement) shown in Figure 5-13 support this conclusion. There was a strong correlation between the valve technique and the optical probe for zero magnetic field, but little correlation at a field of 275 gauss in the frozen regime.

6.3 Liquid Dispersion

There were sharp decreases in liquid mixing for the lowest liquid velocity: a four fold increase in Peclet number at a gas velocity of 0.6 cm/s, and a two fold increase in Peclet number at a gas velocity of 1.1 cm/s. The scatter among replicates was largest when mixing was the least, suggesting that the phenomenon responsible for the reduction in mixing may be transient or unstable under the conditions used in this study. Neverthless, a two-level analysis of variance[94] of the data showed that the increases were statistically significant. It is not clear why the decrease in liquid mixing occurred in the destabilized regime for a gas velocity of 0.6 cm/s and in the channel regime for a gas velocity of 1.1 cm/s.

It was surprising that the magnetic field apparently had no effect on the liquid mixing for higher liquid velocities of 6.44 and 7.71 cm/s. It is possible that the greater interparticle spacing at these velocities may not facilitate the interparticle phenomena that reduce liquid mixing.

Table 6-1 compares literature Pe values (RU/D_{ax}) to the values measured in this study. Davison[96] used alginate particles with a density of 1.05 to 1.15 g/mL. Kim and Kim[97] and Muroyama[98] used glass beads with a density of 2.5 g/mL. The density of the beads used in this study was 1.7 g/mL. Since it has been shown that the liquid mixing in low density particle systems is higher than that of

Table 6-1 Comparison of Measured and Literature Pe Numbers

Author	System Studied	Re	Bead Density (g/mL)	Pe Range
Davison[96]	Three-phase gel beads	1	1.05-1.15	.002-.08
Kim and Kim[97]	Three-phase glass beads	100-200	2.5	.09
Muroyama[98]	Three-phase glass beads	100-200	2.5	.05-.11
Present Study	Three-phase magnetized gel beads with Fe_3O_4	100-200	1.7	.03-.19

dense particle systems[96], it would be expected that the Peclet numbers determined in this study would be between the values measured for the low density particle system and the dense particle systems. However this was not the case; the Peclet numbers from this study are in the same range as those of the glass bead study, and in some cases are larger than those of the glass bead studies. These results reinforce the finding that application of a magnetic field can reduce the axial mixing in a three-phase fluidized bed system.

It has been shown that plug flow behavior gives higher volumetric productivity for reactions exhibiting positive order kinetics or product inhibition[99]. These types of kinetics occur commonly in biological systems, making the MSFB a good candidate for a bioreactor system. For systems which exhibit negative order kinetics, such as substrate inhibition, the bed could be used without the magnetic field or with a field applied to only a portion of the bed, to allow more liquid mixing.

6.3.1 Diffusion Coefficients

The results from the diffusion data clearly indicate that a two parameter fit to Equation 3-14 was necessary to obtain a good fit. The parameter α is defined by Equation 3-15 as the ratio of the liquid volume external to the beads to the bead volume, and it was assumed in the derivation of Equation 3-14 that the total bead volume was accessible to the diffusing molecules. However, this assumption is of questionable validity, because the metal powder occupies, and possibly blocks access to, a portion of the bead volume. The α values determined from the diffusion studies, 2.23, 2.26, and 2.55 for alginate beads containing 0, 5, and 50% by weight magnetite,

respectively, were significantly greater than the value of 2.0 obtained assuming the entire internal volume of the beads was accessible. These results suggest that the bead volume accessible to the diffusing molecule is less than the total bead volume. The appropriate definition of α then, should be the ratio of the liquid volume external to the beads to the accessible volume inside the beads.

6.3.2 Pore Volume Distributions

Figure 5-18a shows the porosities of the alginate beads, that is, the amount of accessible bead volume per unit total bead volume, as a function of pore size. These data were used to calculate α values for the calcium chloride tracer of 2.15, 2.35, and 3.77 for alginate beads containing 0, 5, and 50% by weight magnetite, respectively. The values for the 0 and 5% by weight magnetite agree fairly well with the values obtained from diffusion data, but the value for the 50% by weight magnetite differed by 48%. One possible explanation for this discrepancy is that the solute exclusion technique used sugars or polysaccharides for the diffusing molecules, whereas the other unsteady-state diffusion experiments used an ionic compound (calcium chloride). These two classes of tracer molecules could interact differently with the alginate matrix or the magnetite in the beads. The fact that the α values agree best for the lowest magnetite concentrations suggests that calcium chloride may adsorb to the magnetite. Adsorption would increase the amount of calcium chloride taken up by the beads, causing an overprediction of the accessible pore volume, and, therefore, a smaller value of α.

From Figure 5-18a, the value of bead porosity, ϵ_p, required to solve Equations 3-9 and 3-10 can be determined. The tracer used in this study was calcium chloride. Since calcium chloride dissociates in water into ions the molecular diameter of the tracer is the average of the calcium and the chloride ions. The average number of water molecules which coordinate the ions in aqueous solution is six[99] and spacing them evenly around the ion gives an average diameter equal to the diameter of two water molecules (diameter of 4.2 Å[99]) plus the diameter of the ion itself (calcium ion = 2 Å and chloride ion = 3.6 Å[99]). This gives a diameter of 10.4 Å for calcium and 12.0 Å for chloride with an average value of 11.2 Å. From Figure 5-18a, a molecule of this size would experience a 50% porosity in alginate beads containing 50% by weight magnetite.

Figure 5-17 shows that the addition of magnetite reduces the amount of accessible void volume in the beads since the asymptotic value of each curve represents the total accessible void volume of the beads. The magnetite occupies volume and obstructs pores of the beads, thus also hindering diffusion.

Figure 5-18b, shows that there is a shift toward larger pores as the percentage of magnetite in the beads increases. For example, a molecule with a diameter of 10 Å, would have access to have 98, 98, and 92% of the volume accessible to water in beads containing 0, 5, and 50% by weight magnetite, respectively. In contrast, a molecule with a diameter of 204 Å, would have access to 12, 19, and 26% respectively in the same beads. The magnetite may interfere with the cross-linking of the alginate during bead formation, thus resulting in larger pores.

6.4 Gas-to-Liquid Mass Transfer

It is unclear why the magnetic field affected k_La for the highest and lowest liquid velocities, but not the intermediate velocity. This behavior suggests that two different mechanisms were responsible for the increases in k_La, one of which predominated at the lowest liquid velocity, and the other predominated at the highest velocity. Since the maximum k_La values for a liquid velocity of 5.15 cm/s appeared in the chain-channel regime, the increase probably arose from bubble phenomena that are exclusive to that regime. One observation made in this regime for a liquid velocity of 5.15 cm/s and the two lower gas velocities was that small bubbles (2-3 mm diameter) became entrapped in the three-dimensional mesh of solid particles which formed in this regime. By increasing the bubble residence time, this phenomenon would increase the bubble void fraction, the interfacial area for mass transfer, and hence k_La. However, the fiber optic probe would not necessarily indicate the increase in the local void fraction. Thus, it is reasonable that no increase in local void fraction was observed under these conditions. While this observation offers an explanation for increased mass transfer at the lower gas velocities, there is none for the highest gas velocity. Further study is needed to explain increases in mass transfer for a liquid velocity of 7.71 cm/s.

The MSFB would be a valuable tool for systems where the gas-to-liquid mass transfer step is rate limiting, since the gas-to-liquid mass transfer can be increased by setting the MSFB to the appropriate conditions described above.

6.5 Dimensional Analysis of the Fluidized Bed Model

The dimensionless group Φ can be interpreted physically in terms of two Peclet numbers, $D_{ax,app}/RU$ and D_e/RU. The first group would be the ratio of the dispersive transport to convective convective and the second group the ratio of diffusive transport to convective transport. When the rate of intraparticle diffusion is large compared to either dispersion or convection, the value of Φ becomes large, and the correction factor becomes less than one.

With the plot shown in Figure 5-34, it is now possible to conduct a tracer experiment in a fluidized or packed bed system, calculate the apparent dispersion coefficient using any of the methods described in Section 2.4.3, calculate Φ and Pe_{app}, then graphically determine the correction factor. Multiplication of the correction factor by the observed dispersion coefficient will then give the true dispersion coefficient. This approach eliminates the need to solve Equation 3-9 and 3-10 to account for the effects of both diffusion and axial dispersion. It also shows the regimes within which the effects of diffusion may be neglected.

However, there are some limitations to this model. The numerical technique used to solve the model was unstable for values of Pe_{app} less than 20 and for liquid velocities less than 5 cm/s. The experimentally determined correction factors calculated from the dispersion data measurements in this study agree very well with the correction factors shown in Figure 5-34. However, these correction factors were all greater than 0.9, so the ability of the model to predict correction factors much less than 0.9 was not tested. To further verify the model predictions at higher Φ values, highly

porous, small radius beads, should be used. Such experiments were attempted with highly porous alginate beads without magnetite. Unfortunately, the experimental system gave a Pe_{app} smaller than 20, and the model could not accurately predict the correction factor. It may thus be preferable to use small radius beads to further test the ability of the model to predict correction factors.

6.6 Bioreactor Potential

Based on the results of this study, the three-phase MSFB shows potential for bioreactor application. It is possible to significantly change the bed properties of simply by adjusting the magnetic field strength. Thus, the MSFB can be customized to meet the demands of many types of biological applications. For fast growing biological systems where the rate of oxygen transfer to the liquid phase is rate limiting, the MSFB can be operated in the chain-channel regime where the gas-to-liquid mass transfer coefficient was maximized. For slow growing systems, the cell concentration may be rate limiting. In this case, the cell concentration could be maximized by running the MSFB in the frozen regime where the packing of spherical biocatalyst particles approaches the theoretical limit.

In addition, true continuous processing of the solid phase is possible by operating the MSFB in the frozen regime. Biocatalyst particles would be continuously, or periodically, loated into the top of the reactor and allowed to slowly fall through the reactor in plug flow. Spent biocatalysts would be removed at the same rate from the bottom of the reactor after they stop producing optimally, die, or otherwise exhibit undesirable behavior. Solids residence time could be carefully controlled by the rate of solids addition to maintain

optimal productivity of the bioreactor. This mode of operation should offer imporved performance over conventional bioreactor systems where many of the cells may be dead or in a sub-optimal physiological state. Continuous solids throughput in plug flow is also possible for two-phase MSFB, but scale up of such systems for aerobic bioprocesses would be difficult, because of the limited oxygen-carrying capacity of the aqueous medium.

For reactions which exhibiting positive order kinetics and/or product inhibition, plug flow reactors maximize conversion. By operating the MSFB in the channel regime, where a 400% decrease in the dispersion coefficient was measured, axial mixing of the liquid phase can be minimized. For substrate inhibited reactions, a completely mixed system is desirable and can be easily achieved by using a recycle stream.

The MSFB can thus produce a wide range of properties by simply changing the magnetic field strength, the liquid velocity, and the gas velocity. The MSFB has the capability of acting as a stirred tank by employing a recycle stream, as a packed by operating in the frozen regime, and as a conventional fluidized bed by switching off the magnetic field. In addition, the MSFB offers an excellent package of features not found together in other bioreactor configurations: such as low axial liquid mixing, efficient contacting of gas, liquid, and solid phases, low pressure drops and a low shear environment for immobilized cells.

6.7 Scale-up Considerations

The two important scale-up considerations for the three-phase MSFB are the solid phase and the solenoid. The solid phase used in

this study consisted of 4 mm diameter calcium alginate beads containing 50% by weight magnetite. The relatively large size of the beads would probably lead to significant concentration gradients in the radial direction, leading to reduced catalyst effectiveness factors, and possibly death to cells inside a critical radius. A potential solution to this problem would be to made smaller diameter beads.

In addition, the magnetite tended to leak out of the 50% magnetite beads unless a time consuming coating process was performed on the beads. This coating process would be difficult to conduct aseptically on the beads. A potential solution to this problem would be to make smaller diameter beads containing a lower concentration of magnetite. There was little leakage of magnetite from the alginate beads when only 5% magnetite was present. However, 5% magnetite was not enough for stabilization of the bed at the field strengths used in this study. Thus, there may be an optimum value between 5 and 50% by weight magnetite, where the magnetite will not leak out, but stabilization can be achieved. Higher field strengths may be required for this purpose.

An additional engineering issue is the high viscosity of the magnetite-alginate suspension. Although, in principle, smaller beads can be produced by using a smaller nozzle, the use of small nozzles in making 50% magnetite beads let to plugging of the nozzle. This problem may be overcome by reducing the amount of magnetite in the beads, or better designing the gel dispersion system.

The simplest method to scale up the solenoid is to increase the diameter and the length of the solenoid proportionately while

keeping the ratios α and β (as defined in Figure 3-2) the same. Reasonable criteria for solenoid scale up are that the field strength must remain constant and the ratio of power consumed/surface area available for cooling must either remain constant or decrease. Examination of the solenoid design equations[81], showed that the power consumption of the solenoid was proportional to the solenoid diameter. The power/surface area ratio decreased as the solenoid diameter increased. Thus, better cooling of the solenoid will be possible for larger solenoids. One potential disadvantage to this scale up strategy is that the length of wire might become excessive for large diameter solenoid.

Another scale up strategy would be to keep the length of wire constant was analyzed. The power consumption and ratio of power consumption to surface area available for cooling would remain the same. However, the trade off for this case was that very large currents must be used to obtain a constant field strength. In both of these cases, the power/volume ratio decreases as the solenoid size increases. For very large diameter solenoids, instead of keeping the ratio β (the solenoid length to diameter) constant, it may be desirable to increase the thickness of the wire layer on the solenoid (a_2-a_1) to maintain the desired field strength and decrease the value of β. As this layer becomes thicker, a water jacket alone may not be adequate to cool the solenoid. Other more effective types of cooling have been suggested[81], including the use of hollow wires where cooling water is run through the wires, placement of cooling ducts between the layers of wire, use of liquid gases such as nitrogen, and use of superconductivity. This first two suggestions are probably the

most cost efficient; however, these methods reduce the efficiency of the solenoid[81]. The use of liquid gases would be more costly, and the use of superconductivity would probably make the large scale MSFB prohibitively expensive. However, further increases in the maximum temperature at which superconductivity can be achieved could make this alternative more attractive.

Another important consideration in the scale up of the MSFB is aseptic operation. Introduction of the solid phase at the top of the bed and removal from the bottom present a special problem in maintaining aseptic conditions. Aseptic conditions are especially important for a systems which will be running continuously.

6.8 Conclusions

The three-phase MSFB exhibited several bed regimes that were distinguished by different modes of interaction between the magnetized particles and the rising bubbles: random, chain, chain-channel, destabilized, channel, and frozen. The chain regime is distinguished by small chains of solids forming. The chain-channel regime is characterized by three-dimensional meshes of chains. The destabilized regime occurs when the three-dimensional meshes break into clumps. In these three regimes, a large range of bubble sizes is present, ranging from a few millimeters in diameter to several centimeters. The channel and frozen regimes are characterized by permanent channels in the solid phase through which bubbles preferentially travel. In these two regimes only small bubbles (less than 1 cm) are observed. The chain-channel, destabilized, and channel regimes do not occur in two-phase MSFB indicating the

complexities introduced into three-phase MSFB behavior by the gas phase.

Throughout the course of this study, it has been shown that improvements in bed behavior can be obtained by the application of a magnetic field. A 200-300 percent increase in local gas void fraction was observed in the frozen and channel regimes. A 400 percent increase in Peclet number occurred in the destabilized and channel regimes, and a 30% increase in the mass transfer coefficient occurred in the chain-channel regime. In many cases, the improvements could be attributed to the interactions of gas, liquid, and solid characteristics of a particular bed regime. The increase in mass transfer occurred in the chain-channel regime for liquid velocities of 5.15 and 7.71 cm/s. The increase at 5.15 cm/s could be explained by the small bubbles becoming entrapped in the mesh-like structure of the bed, but the increase at 7.71 cm/s could not be explained. The channel and frozen regimes exhibit similar local gas void fraction properties, while the channel and destabilized regimes exhibit similar liquid mixing properties.

The MSFB properties were strongly affected by the liquid and gas velocities, as well as the magnetic field strength. These variables can thus be used to customize the bed properties for particular applications. The behavior of the three-phase MSFB is much more complicated than the corresponding two-phase systems, and care must be taken in extrapolating data from two-phase systems to three-phase. A theoretical analysis of the effect of tracer diffusion on measured dispersion coefficients was conducted. A correction factor, defined as the ratio of the true dispersion

coefficient to the apparent dispersion coefficient, was graphically correlated as a function of the Peclet number. With this correlation, the extent to which intraparticle tracer diffusion affects the apparent dispersion coefficient can be determined, and the true dispersion coefficient can be calculated, without having to solve the governing partial differential equations. Dimensional analysis indicated that Peclet numbers that express the relative rates of diffusion, dispersion and convection govern when the correction factor would need to be applied.

6.9 Future Work

The large number of unexplainable results from this work shows the complexity of MSFB phenomena. The need for more detailed study of the macroscopic and microscopic bed structures to gain complete understanding of the system is clear.

The original purpose of this work was to develop and optimize a three-phase MSFB for use as a bioreactor. The ability of the MSFB to continuously contact the solid, liquid and gas phases, while the solid phase passes through the reactor in a plug flow should now be exploited in the design of the new bioreactor system. Types of biological systems which would benefit from this reactor configuration are ones that have a limited cell lifetime, produce a toxic product, or store the desired product intracellularly. In addition, a high product value would be required to justify the added cost of providing the magnetic field. An example of this type of system would be production of specialty chemicals using plant cell cultures.

A sterilizable MSFB bioreactor is currently being designed for this purpose. Beads containing magnetite and the desired organism will be fed to the top of the reactor. The magnetic field will prevent mixing of the solids as they proceed down the reactor and are removed from the reactor after the desired residence time. Because there will be no solids mixing, all the cells in the reactor will have nearly identical residence times.

APPENDICES

APPENDIX A

Appendix A: Derivation of Equations

A.1 Unsteady State Well Mixed Model

A mass balance on a well mixed reactor volume gives the following equation

$$\begin{array}{ccccccc} in & - & out & + & generation & = & accumulation \\ FC_o & - & FC_L & + & k_L a V_T (C_L^* - C_L) & = & V_L \dfrac{dC_L}{dt} \end{array} \qquad \text{(A-1)}$$

where F is the flow rate (mL/s), C_o is the inlet concentration in the liquid (g/mL), C_L is the outlet concentration in the liquid (g/mL), V_T is the liquid volume (mL), k_La is the mass transfer coefficient (s^{-1}), C_L^* is the concentration in the liquid phase which is in equilibrium with the gas phase (g/mL), and t is time (s). Rearranging this equation into a more convenient form yields

$$\frac{dC_L}{dt} + C_L\left(\frac{F}{V_T} + k_L a\right) = \frac{FC_o}{V_T} + k_L a C_L^* \qquad \text{(A-2)}$$

Equations of this form have the following solution

$$\begin{gathered} \frac{dy}{dt} + h(t)y = g(t) \\ y(t) = \frac{1}{u}\int u g(t)dt + \frac{B}{u} \\ u(t) = e^{\int h(t)dt} \end{gathered} \qquad \text{(A-3)}$$

For Equation A-2 then

$$h(t) = k_L a + \frac{F}{V_T} \qquad g(t) = \frac{C_o F}{V_T} + k_L a C_L^* \qquad \text{(A-4)}$$

$$u(t) = e^{\int k_L a + \frac{F}{V_T} dt} = e^{(k_L a + \frac{F}{V_T})t}$$

Substituting this into the solution given in equation A-3 gives

$$C_L = e^{-(k_L a + \frac{F}{V_T})t} \int e^{(k_L a + \frac{F}{V_T})t} \left(\frac{C_o F}{V_T} + k_L a C_L^*\right) dt + B e^{-(k_L a + \frac{F}{V_T})t} \qquad \text{(A-5)}$$

Simplifying this equation yields

$$C_L = \frac{\left(\frac{C_o F}{V_T} + k_L a C_L^*\right)}{\left(k_L a + \frac{F}{V_T}\right)} + B e^{-(k_L a + \frac{F}{V_T})t} \qquad \text{(A-6)}$$

Substituting the initial condition that the concentration in the liquid is zero at time zero gives

$$0 = \frac{\left(\frac{C_o F}{V_T} + k_L a C_L^*\right)}{\left(k_L a + \frac{F}{V_T}\right)} + B \qquad \text{(A-7)}$$

Finally, substituting the value for B into Equation A-6 gives the final result

$$C_L = \frac{\left(\frac{C_o F}{V_T} + k_L a C_L^*\right)}{\left(k_L a + \frac{F}{V_T}\right)} \left(1 - e^{-(k_L a + \frac{F}{V_T})t}\right) \qquad \text{(A-8)}$$

A.2 Steady State Well Mixed Model

A steady state mass balance on a well mixed reactor volume gives the following equation

$$\begin{array}{ccccccc} in & - & out & + & generation & = & accumulation \\ FC_o & - & FC_L & + & k_L a V_T (C_L^* - C_L) & = & 0 \end{array} \qquad \text{(A-9)}$$

A.3 Steady State Plug Flow Model

A steady state mass balance on a differential volume element with thickness Δz and cross-section area A is shown in Equation A-10

$$\begin{array}{cccccc} in & - & out & + & generation & = & accumulation \\ AUC_L|_z - AUC_L|_{z+\Delta z} + k_L a A(\Delta z)(C_L^* - C_L) & = & & & 0 & & \end{array} \quad \text{(A-10)}$$

dividing through by $A\Delta z$

$$\frac{UC_L|_z - UC_L|_{z+\Delta z}}{\Delta z} + k_L a(C_L^* - C_L) = 0 \quad \text{(A-11)}$$

and taking the limit as Δz goes to zero gives

$$-\frac{d(UC_L)}{dz} + k_L a(C_L^* - C_L) = 0 \quad \text{(A-12)}$$

Assuming that U is not a function of axial position and rearranging to the form given in Equation A-3

$$\frac{dC_L}{dz} + \frac{k_L a}{U} C_L = \frac{k_L a}{U} C_L^* \quad \text{(A-13)}$$

for this differential equation h(z), g(z), and u(z) are

$$h(z) = \frac{k_L a}{U} \qquad g(z) = \frac{k_L a C_L^*}{U} \quad \text{(A-14)}$$

$$u(z) = e^{\int \frac{k_L a}{U} dz} = e^{(\frac{k_L a}{U})z}$$

Substituting these into the solution given in Equation A-3 yields

$$C_L = e^{-(\frac{k_L a}{U})z} \int e^{(\frac{k_L a}{U})z} \frac{k_L a C_L^*}{U} dz + Be^{-(\frac{k_L a}{U})z} \quad \text{(A-15)}$$

Simplifying this equation gives

$$C_L = C_L^* + Be^{-(\frac{k_L a}{U})z} \quad \text{(A-16)}$$

Using the boundary condition that the liquid concentration at z=0 is zero gives

$$0 = C_L^* + B \quad \text{(A-17)}$$

Substituting this into Equation A-16 gives the final result

$$C_L = C_L^*(1 - e^{-(\frac{k_L a}{U})z}) \quad \text{(A-18)}$$

A.4 Steady State Dispersed Plug Flow Model

A steady state mass balance on a differential volume element of thickness Δz and cross-sectional area A is shown in Equation 2-19

$$\begin{array}{ccccccccc} in & - & out & + & generation & = & accumulation \\ UAC_L|_z + A\varepsilon_L N|_z & - & UAC_L|_{z+\Delta z} - A\varepsilon_L N|_{z+\Delta z} & + & k_L a A(\Delta z)(C_L^* - C_L) & = & 0 \end{array} \quad \text{(A-19)}$$

where N is the flux through the volume element due to disperison, and ϵ_L is the liquid fraction in the volume element. Dividing through by $A\Delta z$ gives

$$\frac{UC_L|_z - UC_L|_{z+\Delta z}}{\Delta z} + \frac{\varepsilon_L(N|_z - N|_{z+\Delta z})}{\Delta z} + k_L a(C_L^* - C_L) = 0 \quad \text{(A-20)}$$

and taking the limit as Δz goes to zero

$$-\frac{d(UC_L)}{dz}-\varepsilon_L\frac{dN}{dz}+k_La(C_L^*-C_L)=0 \qquad \text{(A-21)}$$

Assuming that the dispersive flux can be modelled by a Fickian diffusion mechanism

$$N=-D_{ax}\frac{dC_L}{dz} \qquad \text{(A-22)}$$

and that U is not a function of z the final form of the differential equation results

$$D_{ax}\varepsilon_L\frac{d^2C_L}{dz^2}-U\frac{dC_L}{dz}+k_La(C_L^*-C_L)=0 \qquad \text{(A-23)}$$

The boundary conditions for this differential equation are

$$\begin{aligned} z=0 \qquad & C_L=C_o+\frac{D_{ax}}{U}\frac{dC_L}{dz} \\ z=L \qquad & \frac{dC_L}{dz}=0 \end{aligned} \qquad \text{(A-24)}$$

The characteristic equation for Equation A-23 is

$$n^2-\frac{U}{\varepsilon_L D_{ax}}n-\frac{k_La}{\varepsilon_L D_{ax}}=0 \qquad \text{(A-25)}$$

Using the quadratic formula give the following real roots

$$n_{1,2}=\frac{U}{2D_{ax}\varepsilon_L}\left(1\pm\sqrt{1+\frac{4k_LaD_{ax}\varepsilon_L}{U^2}}\right) \qquad \text{(A-26)}$$

The solution of Equation A-23 will then be of the following form

$$C_L = A_1 e^{n_1 z} + A_2 e^{n_2 z} + A_3 \qquad \text{(A-27)}$$

By inspection the constant term A_3 must be C_L^*. Applying the boundary condition at z=L gives A_1 as a function of A_2

$$A_1 = -\frac{n_2 A_2 e^{(n_1 - n_2)L}}{n_1} \qquad \text{(A-28)}$$

Applying the boundary condition at z=0 and substituting Equation A-28 give an expression for A_2

$$A_2 = \frac{(C_o - C_L^*)}{-\frac{n_2}{n_2} e^{(n_2 - n_1)L} + \frac{D_{ax}}{U} n_2 e^{(n_2 - n_2)L} - \frac{D_{ax}}{U} n_2 + 1} \qquad \text{(A-29)}$$

Multiplying the numerator and denominator by the term $n_1 e^{n_1}$ gives

$$A_2 = \frac{(C_o - C_L^*) n_1 e^{n_1 L}}{-n_2 e^{n_2 L} + \frac{D_{ax}}{U} n_2 n_1 e^{n_2 L} - \frac{D_{ax}}{U} n_2 n_1 e^{n_1 L} + n_1 e^{n_1 L}} \qquad \text{(A-30)}$$

Grouping like terms in the denominator gives

$$A_2 = \frac{(C_o - C_L^*) n_1 e^{n_1 L}}{n_1 e^{n_1 L}[\frac{D_{ax}}{U} n_2 - 1] - n_2 e^{n_2 L}[\frac{D_{ax}}{U} n_1 - 1]} \qquad \text{(A-31)}$$

Expanding the first term in brackets in the denominator gives

$$\frac{D_{ax}}{U} n_2 - 1 = \frac{D_{ax}}{U}[\frac{U}{2 D_{ax} \varepsilon_L}(1 - \sqrt{1 + \frac{4 k_L a D_{ax} \varepsilon_L}{U^2}})] - 1 \qquad \text{(A-32)}$$

Simplifying Equation A-32, it can be shown

$$\frac{D_{ax}}{U}n_2 - 1 = -n_1\frac{U}{D_{ax}} \qquad \text{(A-33)}$$

and a similar expansion can be done on the second term in brackets to show that

$$\frac{D_{ax}}{U}n_1 - 1 = -n_2\frac{U}{D_{ax}} \qquad \text{(A-34)}$$

Substituting the expressions in Equation 2-33 and 2-34 into Equation 2-31 gives a final expression for A_2

$$A_2 = \frac{-(C_o - C_L^*)n_1 e^{n_1 L}}{\frac{U}{D_{ax}}(n_1^2 e^{n_1 L} - n_2^2 e^{n_2 L})} \qquad \text{(A-35)}$$

A similar analysis can be performed to find A_1

$$A_1 = \frac{(C_o - C_L^*)n_2 e^{n_2 L}}{\frac{U}{D_{ax}}(n_1^2 e^{n_1 L} - n_2^2 e^{n_2 L})} \qquad \text{(A-36)}$$

A.5 Stirred Tank in Series Model

A mass balance on a well stirred reactor volume including the effect of tracer diffusion into the solid phase gives

$$\begin{aligned} in \;-\; out \;+\; generation \;&=\; accumulation \\ UAC_o \;-\; UAC_L \;-\; loss\ due\ to\ diffusion \;&=\; \varepsilon_L V_T \frac{dC_L}{dt} \end{aligned} \qquad \text{(A-37)}$$

A convenient description for the term due to diffusion is the negative

of the term describing the accumulation of tracer inside the beads, and unit analysis is used to get the appropriate units of grams/second as shown in Equation A-38

$$\frac{\textit{grams tracer}}{\textit{accessible bead volume}\cdot\textit{time}}\;\frac{\textit{accessible bead volume}}{\textit{bead volume}}\;\frac{\textit{bead volume}}{\textit{total volume}}\;\textit{total volume}$$

$$\frac{dC_B}{dt} \qquad \epsilon_p \qquad \epsilon_s \qquad V_T$$

(A-38)

where C_B is the concentration in the solid phase (g of tracer/mL of accessible bead volume), and ϵ_p is the porosity of the solid phase. Substituting this into Equation A-37 gives

$$UA(C_o - C_L) - \epsilon_p \epsilon_s V_T \frac{dC_B}{dt} = \epsilon_L V_T \frac{dC_L}{dt} \qquad \textbf{(A-39)}$$

APPENDIX B

Appendix B: Computer Programs

B.1 Solenoid Design

```
* * * * * * * * * * * * * * * * * * * * * * * * * * * * * * * * * * * *
C    THIS PROGRAM CALCULATES REQUIRED SYSTEM
C    PARAMETERS TO PRODUCE A GIVEN SPECIFICATION FOR
C    A GIVEN FIELD STRENGTH OR A GIVEN LENGTH OF WIRE
* * * * * * * * * * * * * * * * * * * * * * * * * * * * * * * * * * * *
     REAL*8 DS,LS,DW,HO,PI,RHO,A,A1,BETA,LW
     REAL*8 ALPHA,N,FAB,I
     REAL*8 R,V,P,LAMBDA,Q,WV,WS,D2,VEL
     REAL*8 D,H,DELTW,DELTC,DELTF
     REAL*8 DELTI,DELTS,KCU,KFORM,KI,TFORM,TI
     INTEGER STEP
     PRINT*,'DO YOU WANT TO STEP OFF LENGTH OR
    $    FIELD,1=LENGTH 2=FIELD'
     READ*,STEP
     PRINT*,'INPUT DIAMETER AND LENGTH OF
    $    SOLENOID,AND WIRE DIAMETER
    $    IN CENTIMETERS'
     READ*,DS,LS,DW
     PRINT*,'INPUT FIELD STRENGTH IN OERSTEDS'
     READ*,HO
     PRINT*,'INPUT LENGTH OF WIRE IN METERS'
     READ*,LW
     OPEN(2,FILE='CURRENT',STATUS='NEW')
     OPEN(1,FILE='HEAT',STATUS='NEW')
     IF(STEP.EQ.1) THEN
      WRITE(1,*),'SOLENOID LENGTH   =',LS,'CM'
      WRITE(1,*),'SOLENOID DIAMETER =',DS,'CM'
      WRITE(1,*),'WIRE DIAMETER     =',DW,'CM'
      WRITE(1,*)
      WRITE(2,*),'SOLENOID LENGTH   =',LS,'CM'
      WRITE(2,*),'SOLENOID DIAMETER =',DS,'CM'
      WRITE(2,*),'WIRE DIAMETER     =',DW,'CM'
      WRITE(2,*)
      GOTO 40
     ENDIF
     WRITE(1,*),'SOLENOID LENGTH   =',LS,'CM'
     WRITE(1,*),'SOLENOID DIAMETER =',DS,'CM'
     WRITE(1,*),'WIRE DIAMETER     =',DW,'CM'
     WRITE(1,*)
     WRITE(2,*),'SOLENOID LENGTH   =',LS,'CM'
     WRITE(2,*),'SOLENOID DIAMETER =',DS,'CM'
     WRITE(2,*),'WIRE DIAMETER     =',DW,'CM'
     WRITE(2,*)
40    PI=3.141592654
     RHO=1.7E-6
     LAMBDA=PI/4.*((DW-.00762)/DW)**2.
     KCU=3.86
     KFORM=.0099822
     KI=.014
```

```
      TFORM=.00762
      TI=.2
      WRITE(1,*),'FLOW RATE    WATER TEMP    SOLENOID
     $    TEMP     FIELD   STRENGTH    LENGTH OF WIRE'
      WRITE(2,*),' N      R       LW      I       P       V
     $      ALPHA    HO'
20     A=(DW/2.)**2.*PI
      A1=DS/2.
      BETA=(LS/2.)/A1
      LW=LW*100
      ALPHA=(LW*A/(2*A1**3*PI*BETA)+1)**0.5
      N=2.*A1**2.*BETA*(ALPHA-1)/A
      FAB=LOG((ALPHA+(ALPHA**2.+BETA**2.)**0.5)
     $    /(1+(BETA**2.+1)**0.5))
      FAB=4*PI*BETA/10.*FAB
      I=2*HO*A1*BETA*(ALPHA-1)/(N*FAB)
      R=N**2*RHO/A1*PI*(ALPHA+1)
     $    /(2*BETA*(ALPHA-1)*LAMBDA)
      V=I*R
      P=PI*N**2*I**2*RHO*(ALPHA+1)
     $   /(2*A1*BETA*(ALPHA-1)*LAMBDA)
      Q=P/41.86
      WV=P/(A1**3*2*PI*BETA*(ALPHA**2-1))
      WS=P/(PI*(DS-0.4)*LS)
      D2=DS-0.4
      VEL=4*Q/(PI*(D2**2-6**2.))
      D=DS-6.4
      H=9E-3*(1+1.5E-2*19)*VEL**0.8/D**0.2
      DELTW=14+10+WS/H
      DELTC=WV*.2**2/(2*KCU)
      DELTF=WS*TFORM/KFORM
      DELTI=WS*TI/KI
      DELTS=DELTC+DELTF+DELTI
      IF(STEP.EQ.1) THEN
       GOTO 10
      ENDIF
      WRITE(2,100),N,R,LW/100,I,P,V,ALPHA,HO
100    FORMAT(F6.0,3X,F6.2,3X,F7.1,3X,
     $    F7.2,3X,F8.2,3X,F7.2,3X,F8.5,3X,F5.1)
      WRITE(1,300),Q,DELTW,DELTS,HO,LW/100
300    FORMAT(F7.2,9X,F8.4,9X,F8.4,11X,F5.1,13X,F7.1)
      HO=HO+10
      LW=LW/100.
      IF(HO.GT.500.) THEN
       GOTO 30
      ENDIF
      GOTO 20
10     WRITE(2,200),N,R,LW/100,I,P,V,ALPHA,HO
200    FORMAT(F6.0,3X,F6.2,3X,F7.1,3X,F7.2,
     $    3X,F8.2,3X,F7.2,3X,F8.5,3X,F5.1)
      WRITE(1,400),Q,DELTW,DELTS,HO,LW/100
400    FORMAT(F7.2,9X,F8.4,9X,F8.4,11X,F5.1,13X,F7.1)
      LW=LW/100.
```

```
      LW=LW+50
      IF(LW.GT.2000.) THEN
        GOTO 30
      ENDIF
      GOTO 20
30     CLOSE(2)
      CLOSE(1)
      STOP
      END

* * * * * * * * * * * * * * * * * * * * * * * * * * * * * * * * * * * *
C       THIS PROGRAM CALCULATES THE AXIAL FIELD
C       PROFILE OF A SOLENOID
* * * * * * * * * * * * * * * * * * * * * * * * * * * * * * * * * * * *
      REAL*8 H(600),ALPHA,BETA,HO
      INTEGER I
5     OPEN(2,FILE='STRENGTH',STATUS='NEW')
      Z=0.5
      PRINT*,'ENTER THE FIELD STRENGTH'
      READ*,HO
      PI=3.141592654
      DO 10  I=1,160
      ALPHA=1.11279
      BETA=30.75/4.6
      BETAMI=ABS(BETA-Z/4.6)
      BETAPL=BETA+Z/4.6
      F=LOG((ALPHA+(ALPHA**2+BETA**2)**0.5)
     $   /(1+(1+BETA**2)**0.5))
      F=4*PI*BETA*F/10
      FPL=LOG((ALPHA+(ALPHA**2+BETAPL**2)**0.5)
     $   /(1+(1+BETAPL**2)**0.5))
      FPL=4*PI*BETAPL*FPL/10
      FMI=LOG((ALPHA+(ALPHA**2+BETAMI**2)**0.5)
     $   /(1+(1+BETAMI**2)**0.5))
      FMI=4*PI*BETAMI*FMI/10
      IF((Z/4.).LE.BETA) THEN
         H(I)=HO*(FPL+FMI)/(2*F)
         WRITE(2,100), Z, H(I)
100       FORMAT(F5.1,5X,F7.2)
         Z=Z+0.5
      ELSE
         H(I)=HO*(FPL-FMI)/(2*F)
         WRITE(2,200) Z,H(I)
200       FORMAT(F5.1,5X,F7.2)
         Z=Z+0.5
      ENDIF
10    CONTINUE
      CLOSE(2)
      PRINT*,'DO YOU WANT ANOTHER TRY?, YES=1, NO=2'
      READ*,TRY
      IF(TRY.EQ.1) THEN
      GOTO 5
      ENDIF
```

```
      STOP
      END
```

B.2 Gas Void Fraction

```
* * * * * * * * * * * * * * * * * * * * * * * * * * * * * * * * * * * *
C     THIS PROGRAM CALCULATES THE VOID FRACTION
C    FROM DATA COLLECTED FROM A OPTICAL FIBER PROBE
* * * * * * * * * * * * * * * * * * * * * * * * * * * * * * * * * * * *
      real a, b, c, t, v, i, nse, sum, t1, inc, ltime, noise, hival
      real percent, void
      integer j, flag1, flag2, k
      write(*,*) 'INPUT NUMBER OF DATA FILES'
      read(*,*) n
      write(*,*) 'INPUT LAST TIME POINT:'
      read(*,*) ltime
      write(*,*)'INPUT THE NOISE LEVEL AND HIGH VALUE:'
      read(*,*) noise,hival
      write(*,*) 'INPUT THE % ABOVE NOISE TO USE:'
      read(*,*) percent
      i = 1./100.
      percent = percent/100.
      nse = noise + (hival - noise) * percent
      do 30 k = 1, n
        write(*,*)
        open(2,file=' ',status='old')
        read(2,*) a, b
        sum = 0.0
        if (b .le. nse) then
          flag1 = 1
        else
          flag1 = 0
        endif
        do 10 j = 1, 10000
          if (a .ge. ltime) goto 20
          read(2,*) t, v
          if (v .le. nse) then
            flag2 = 1
          else
            flag2 = 0
          endif
          if ((flag1 .eq. 0) .and. (flag2 .eq. 0)) then
            sum = sum + i
          elseif (flag1 .ne. flag2) then
            t1 = a + (t - a)*(nse - b)/(v - b)
            if (flag1 .gt. flag2) then
              inc = t - t1
            else
              inc = t1 - a
            endif
            sum = sum + inc
          endif
          a = t
```

```
        b = v
        flag1 = flag 2
  10    continue
  20    void = sum/ltime
        write(*,*) 'THE VOID FRACTION =  ', void
        close(2)
  30 continue
     stop
     end

* * * * * * * * * * * * * * * * * * * * * * * * * * * * * * * * * * *
C      THIS PROGRAM CALCULATE THE BUBBLE VELOCITY OF
C     A BUBBLE WHICH TRAVELS BETWEEN TWO OPTICAL
C     FIBER PROBES
* * * * * * * * * * * * * * * * * * * * * * * * * * * * * * * * * * *
     real t,tau,step,up,cross,cross1,low,fli,time,corr(55,5)
     real keep(55,5)
     integer n, num, count
     character*20 name1, name2
     write(*,*) 'INPUT TOTAL TIME, STEP SIZE, AND NUMBER
    $    OF POINTS'
     read(*,*) t,step,num
     write(*,*) 'INPUT A GUESS OF TAU'
     read(*,*) tau
     write(*,*)'INPUT THE NAME OF FILES FOR PROBE 1 AND 2'
     read(*,*) name1,name2
     tau = tau - 25*step
     do 5 k = 1,50
10      n = tau/step
       open(2, file=name1, status='old')
       open(3, file=name2, status='old')
       do 20 i=1,n
         read(3,*) time,up
20      continue
       read(2,*) tl,low
       read(3,*) time,up
       cross = low*up
       do 30 j=1,10000
         read(2,*) tl,low
         read(3,*) time, up
         fli = low*up
         if(time.eq.t) then
           cross = fli +cross
           goto 40
         else
           cross = cross + 2*fli
         endif
30      continue
40      do 50 i=1,2
         if(i.eq.1) then
           corr(k,i) = cross/(2*num)
         else
           corr(k,i) = tau
```

```
        endif
50      continue
       close(2)
       close(3)
       tau = tau + step
       write(*,*) 'loop',k
5     continue
     keep(1,1) = corr(1,1)
     keep(1,2) = corr(1,2)
     do 60 i=2,50
       if(corr(i,1).gt.keep(1,1)) then
         keep(1,1) = corr(i,1)
         keep(1,2) = corr(i,2)
       endif
60    continue
     write(*,*)'tau =',keep(1,2)
     stop
     end
```

B.3 Optimization Program

The remaining programs utilize an optimization called PATERN which finds the optimum value of a variable. The PATERN program will be listed here and deleted from the subsequent programs to save space.

```
      SUBROUTINE PATERN(NP,P,STEP,NRD,IO,COST)
C-----THE SIZE OF B1,B2,T,AND S NEED ONLY BE EQUAL TO
C-----    THE NUMBER OF PAR
      DIMENSION P(1000),STEP(1000),B1(100),B2(100)
      DIMENSION T(100),S(100)
C-------------------------------------------------------
C     THE FOLLOWING COMMAND ALLOWS PATERN TO USE
C     AN INTEGER VARIABLE AS THE THIRD PARAMETER P(3).
C
      NSRC   =3
      P(NSRC) =     ifix(P(NSRC))
C-------------------------------------------------------
C-----STARTING POINT
      L=1
      ICK=2
      ITTER=0
      DO5 I=1,NP
      B1(I)=P(I)
      B2(I)=P(I)
      T(I)=P(I)
 5    S(I)=STEP(I)*10.
C-----INITIAL BOUNDARY CHECK AND COST EVALUATION
      CALL BOUNDS(P,IOUT)
      IF(IOUT.LE.0)GOTO10
              IF(IO.LE.0)GOTO6
              WRITE(*,1005)
```

```
            WRITE(*,1000)(J,P(J),J=1,NP)
 6  RETURN
10   CALL PROC(P,C1)
            IF(IO.LE.0)GOTO11
            WRITE(*,1001)ITTER,C1
            WRITE(*,1000)(J,P(J),J=1,NP)
C-------BEGINNING OF PATTERN SEARCH STRATEGY
11   DO99 INRD=1,NRD
     DO12 I=1,NP
12   S(I)=S(I)/10.
C-------------------------------------------------------------
     S(NSRC) =      1.0001
C-------------------------------------------------------------
            IF(IO.LE.0)GOTO20
            WRITE(*,1003)
            WRITE(*,1000)(J,S(J),J=1,NP)
20   IFAIL=0.0
C-----PRETURBATION ABOUT T
     DO30 I=1,NP
     IC=0
21   P(I)=T(I)+S(I)
     IC=IC+1
     CALL BOUNDS(P,IOUT)
     IF(IOUT.GT.0)GOTO23
     CALL PROC(P,C2)
            L=L+1
            IF(IO.LT.3)GOTO22
            WRITE(*,1002)L,C2
            WRITE(*,1000)(J,P(J),J=1,NP)
22   IF(C1-C2)23,23,25
23   IF(IC.GE.2)GOTO24
     S(I)=-S(I)
     GOTO21
24   IFAIL=IFAIL+1
     P(I)=T(I)
     GOTO30
25   T(I)=P(I)
     C1=C2
30   CONTINUE
     IF(IFAIL.LT.NP)GOTO35
     IF(ICK.EQ.2)GOTO90
     IF(ICK.EQ.1)GOTO35
     CALL PROC(T,C2)
            L=L+1
            IF(IO.LT.2)GOTO31
            WRITE(*,1002)L,C2
            WRITE(*,1000)(J,T(J),J=1,NP)
31   IF(C1-C2)32,34,34
32   ICK=1
     DO33 I=1,NP
     B1(I)=B2(I)
     P(I)=B2(I)
33   T(I)=B2(I)
```

```
      GOTO20
 34   C1=C2
 35   IB1=0
      DO39 I=1,NP
      B2(I)=T(I)
      IF(ABS(B1(I)-B2(I)).LT.1.0E-20)IB1=IB1+1
 39   CONTINUE
      IF(IB1.EQ.NP)GOTO90
      ICK=0
              ITTER=ITTER+1
              IF(IO.LT.2)GOTO40
              WRITE(*,1001)ITTER,C1
              WRITE(*,1000)(J,T(J),J=1,NP)
C-----ACCELERATION STEP
 40   SJ=1.0
      DO45 II=1,11
      DO42 I=1,NP
      T(I)=B2(I)+SJ*(B2(I)-B1(I))
C-------------------------------------------------------------
       IF(I.EQ.NSRC)T(I)=ifix(T(I))
C-------------------------------------------------------------
 42   P(I)=T(I)
      SJ=SJ-.1
      CALL BOUNDS(T,IOUT)
      IF(IOUT.LT.1)GOTO46
      IF(II.EQ.11)ICK=1
 45   CONTINUE
 46   DO47 I=1,NP
 47   B1(I)=B2(I)
      GOTO20
 90   DO91 I=1,NP
 91   T(I)=B2(I)
 99   CONTINUE
      DO100 I=1,NP
100   P(I)=T(I)
      COST=C1
              IF(IO.LE.0)RETURN
              WRITE(*,1004)L,C1
              WRITE(*,1000)(J,P(J),J=1,NP)
      RETURN
1000  FORMAT(3(35X,I7,5X,E13.6/))
1001  FORMAT(//1X13HITERATION NO.  ,I5/5X,5HCOST=
     $    ,E15.6,20X,10HPARAMETERS)
1002  FORMAT(10X3HNO.,I4, 8X5HCOST=,E15.6)
1003  FORMAT(/1X28HSTEP SIZE FOR EACH PARAMETER   )
1004  FORMAT(1H113HANSWERS AFTER
     $    ,I3,2X,23HFUNCTIONAL EVALUATIONS   //
     $    5X5HCOST=,E15.6,20X,18HOPTIMAL PARAMETERS  )
1005  FORMAT(1H135HINITIAL PARAMETERS OUT OF
     $    BOUNDS       )
      END
```

B.4 Dispersion Coefficients

```
* * * * * * * * * * * * * * * * * * * * * * * * * * * * * * * * * * * *
C     SUBROUTINE PROC FOR PROGRAM CALLED PATERN
C
C     PURPOSE:  TO ESTIMATE DISPERSION COEFFICIENTS BY
C                  READING IN DATA CONTAINING TIME -VS-
C                     CONCENTRATION VALUES.
* * * * * * * * * * * * * * * * * * * * * * * * * * * * * * * * * * * *
C
C     MAIN PROGRAM
C
C
      INTEGER NDATA,NP,NPASS,IO
      integer ip, i, nin, nres, nterm
      real pm(20), cdi(200), cwork(10), toin, dtin, tores, dtres,
     $     cdr(200), tau, p(10), step(10)
      common /main1/cdi,toin,dtin
      common /main2/cdr,tores,dtres
      common /main5/nin,nres
      common /pbparm/pm
      common /main4/tau,nterm
      open(2,file='file2.csv',status='old')
      open(3,file='file1.csv',status='old')
      open(4,file='file3.csv',status='old')
      ip=8
      read(2,300) (pm(i), i=1,ip)
      write(*,*) (pm(i), i=1,ip)
  300  format(8f10.0)
      read(3,100) toin,dtin
      write(*,*)toin,dtin
  100  format(2f10.0)
      nin=0
  110  format(10f8.0)
    1  read(3,110,end=90) (cwork(i), i=1,10)
      write(*,*) (cwork(i), i=1,10)
      do 10 i = 1, 10
        if (cwork(i) .lt. 0.0) goto 90
        nin=nin+1
        if (nin .gt. 200) goto 90
        cdi(nin)=cwork(i)
        write(*,*) cdi(nin)
   10  continue
      goto 1
   90  nres=0
      read(3,*) tores,dtres
      write(*,*) tores,dtres
    2  read(3,110,end=91) (cwork(i), i=1,10)
      write(*,*) (cwork(i), i=1,10)
      do 20 i=1,10
        if (cwork(i) .lt. 0.0) goto 91
        nres=nres+1
        if (nres .gt. 200) goto 91
        cdr(nres)=cwork(i)
        write(*,*) cdr(nres)
```

```
 20  continue
     goto 2
 91  read(4,200) tau,nterm
     write(*,*) tau, nterm
200  format(f10.0,i10)

     call norsig
     call fouexp

C     SEARCH INITIALIZATION
     P(1)= 0.01
     p(2)= 1.0e-3
     STEP(1)=0.01
     step(2)=1.0e-3
     NP=2
     NPASS=3
     IO=3
C
C
C     START SEARCH
C
     CALL PATERN(NP,P,STEP,NPASS,IO,COST)
C
C     SEARCH COMPLETE, PRINT RESULTS
C     PRINT 399, P(1), P(2), COST
C399   FORMAT(F10.3,10X,F10.3)
     OPEN (UNIT=30,FILE='FOR30.DAT',STATUS='NEW')
     WRITE (30,399) P(1),P(2),COST
399   FORMAT(E10.3,5X,F6.3,5X,E10.3)
     STOP
     END
C
C
C
C     THIS FILE IS A PAIR OF SUBROUTINES WRITTEN TO BE
C     COMPATIBLE WITH THE OPTIMIZATION SUBROUTINE
C     PATERN.  THEY SIMULATE A PROCESS USING DISCRETE
C     DIFFERENCE EQUATIONS AND COMPARE THE
C     SIMULATION OUTPUT WITH THE ACTUAL OUTPUT
C     (READ IN THROUGH A DATA FILE), CALCULATING AN
C     ERROR OR "COST" ASSOCIATED WITH THAT
C     SIMULATION.  PATERN USES THESE SUBROUTINES
C     ITERATIVELY IN ORDER TO FIND THE OPTIMUM SET OF
C     TRANSFER FUNCTION PARAMETERS TO FIT THE DATA.
C
C
     SUBROUTINE PROC(P,COST)
     dimension p(10)

    common/pbparm/pm(20)
    common/main3/error
    pm(2)=p(1)
    pm(7)=p(2)
```

```
      call precur
      cost=error

       RETURN
       END
C
C
C
       SUBROUTINE BOUNDS(P,IOUT)
       DIMENSION P(10), STEP(10)
       IOUT=0
       IF(P(1).LE.0) IOUT=1
       RETURN
       END
C
C
C
C

      subroutine norsig
      integer znin,znres
      common /main1/ cdin,ztoin,zdtin
      common /main2/ cdres,ztores,zdtres
      common /main5/znin,znres
      common /signal/toin,dtin,nin,cin(200),
     $      tores,dtres,nres,cres(200)
      dimension cdin(200),cdres(200)
      nin=znin
      toin=ztoin
      dtin=zdtin
      nres=znres
      tores=ztores
      dtres=zdtres
      call normlz(dtin,nin,cdin,ain,cin)
      call normlz(dtres,nres,cdres,ares,cres)
      return
      end

      subroutine normlz(dt,n,cd,area,cn)
      dimension cd(200),cn(200)
      area = 0.0
      do 10 i=1,n
        area=area+cd(i)
10    continue
      area=area*dt
      if(area.eq.0.0) then
        write(*,600)
        do 20 i=1,n
          cn(i)=cd(i)
20      continue
        return
      elseif(area.lt.0.0) then
        write(*,610)
```

```
      endif
      do 30 i=1,n
        cn(i)=cd(i)/area
30    continue
      return

600   format(1h0,'area of curve is zero(returned signal is not normal
     $ized).'/)
610   format(1h0,'area of curve is negative.'/)
      end

      subroutine fouexp
      common /main4/ztau,znterm
      common /signal/ toin,dtin,nin,cin(200),
     $           tores,dtres,nres,cres(200)
      common/fdata/ tau,nterm,aoin,ain(200),bin(200),
     $          aores,ares(200),bres(200)
      tau=ztau
      nterm=znterm
      if(tau.lt.(tores+dtres*float(nres))/2.0) then
        tau=(tores+dtres*float(nres))/2.0*1.5
        write(*,610) tau
      endif
      if(nterm.lt.1.or.nterm.gt.ifix(tau/dtres+0.5)) then
        nterm=ifix(tau/dtres+0.5)
        write(*,620) nterm
      endif
      if(nterm.gt.200) then
        nterm=200
        write(*,620) nterm
      endif
      call foucoe(toin,dtin,nin,cin,tau,nterm,aoin,ain,bin)
      call foucoe(tores,dtres,nres,cres,tau,nterm,aores,ares,bres)
      return

610   format(1h0,'half period (tau) is replaced by',e15.7)
620   format(1h0,'number of terms (nterm) is replaced by',i5)
      end

      subroutine foucoe(to,dt,nt,cn,tau,nterm,ao,a,b)
      dimension cn(200),a(200),b(200)
      data pi/3.141593/
      ao=0.0
      sq=0.0
      do 10 i=1,nt
        ao=ao+cn(i)
        sq=sq+cn(i)**2
10    continue
      ao=ao*dt/tau
      sq=sq*dt
      cotest=ao/2.0
      sqtest=2.0*(ao/2.0)**2*tau
      do 20 n=1,nterm
```

```
      x=0.0
      y=0.0
      sv=float(n)*pi/tau
      do 30 i=1,nt
        z=sv*(to+float(i-1)*dt)
        x=x+cn(i)*cos(z)
        y=y+cn(i)*sin(z)
30     continue
      a(n)=x*dt/tau
      b(n)=y*dt/tau
      cotest=cotest+a(n)
      sqtest=sqtest+(a(n)**2+b(n)**2)*tau
      if(mod(n,10).eq.0) then
        rat=sqtest/sq
      endif
20   continue
     return
     end

     subroutine precur
     common /main3/err
     common/signal/toin,dtin,nin,cin(200),tores,dtres,nres,
    $          cres(200)
     common/fdata/tau,nterm,aoin,ain(200),bin(200),aores,
    $          ares(200),bres(200)
     common/pbparm/ pm(20)
     dimension aclc(200),bclc(200)
     call clccoe(pm,tau,nterm,nt,aoin,ain,bin,aoclc,aclc,bclc)
     call clccur(tau,nt,aoclc,aclc,bclc,0.0,2.0*tau,dtres)
     x=2.0*(aores/2.0-aoclc/2.0)**2
     y=2.0*(aores/2.0)**2
     do 40 i=1,nt
       x=x+(ares(i)-aclc(i))**2+(bres(i)-bclc(i))**2
       y=y+ares(i)**2+bres(i)**2
40   continue
     err = sqrt(x/y)
     return
     end

     subroutine clccoe(pm,tau,nterm,nt,aoin,ain,bin,aoclc,aclc,bclc)
     dimension pm(20),ain(200),bin(200),aclc(200),bclc(200)
     data pi/3.141593/
     call transf(0,0.0,pm,an,bn)
     aoclc=aoin*an
     do 10 n=1,nterm
       w=float(n)*pi/tau
       call transf(1,w,pm,an,bn)
       aclc(n)=ain(n)*an+bin(n)*bn
       bclc(n)=bin(n)*an-ain(n)*bn
       if(an**2+bn**2.lt.1.0e-8) then
         nt=n
         return
       endif
```

```
10   continue
     nt=nterm
     return
     end

     subroutine transf(ictl,w,pm,an,bn)
     dimension pm(20)
     real*8 d1,d2,d3,d4,d5
     save d1,d2,d3,d4,d5
     complex*16 cs,cphi,cex,coth,cq,cf
     if(ictl.eq.0) then
       d1=pm(7)/(pm(1)*pm(2))
       d2=pm(1)/pm(2)
       d3=pm(8)*pm(3)/(pm(4)*pm(5))
       if(pm(8).eq.0.0) then
         d4=0.0
       else
         d4=pm(6)/pm(8)
       endif
       d5=pm(5)
     endif
     if(w.eq.0.0) then
       an=1.0
       bn=0.0
       return
     endif
     cs=cmplx(0.0,w)
     if(d4.eq.0.0) then
       cf=cdexp(1.0/(2.0*d1)*(1.0-cdsqrt(1.0+4*d1*d2*cs)))
     else
       cphi=d5*cdsqrt(cs*d4)
       cex=cdexp(-2.0*cphi)
       coth=(1.0+cex)/(1.0-cex)
       cq=d3*(cphi*coth-1.0)
       cf=cdexp(1.0/(2.0*d1)*(1.0-cdsqrt(1.0+4*d1*d2*(cs+cq))))
     endif
     an=cf
     bn=dimag(cf)
     return
     end

     subroutine clccur(tau,nt,ao,a,b,t1,t2,dt)
     dimension a(200),b(200),c(500),t(500)
     data pi/3.141593/
     if(dt.eq.0) then
       in=1
       dtw=dt
     else
       in=ifix((t2-t1)/dt+0.5)
       if(in.ge.0) then
         in=in+1
         dtw=dt
       else
```

```
        in=-in+1
        dtw=-dt
      endif
      if(in.gt.500) then
        in=500
        write(*,610) in
      endif
    endif
    do 10 i=1,in
      t(i)=t1+float(i-1)*dtw
      c(i)=ao/2.0
10   continue
    do 20 n=1,nt
      sv=float(n)*pi/tau
      do 30 i=1,in
        z=sv*t(i)
        c(i)=c(i)+(a(n)*cos(z)+b(n)*sin(z))
30     continue
20   continue
    return
610  format(1h0,'number of data(in) is replaced by',i5/)
    end
```

B.5 Mass Transfer Coefficients

```
* * * * * * * * * * * * * * * * * * * * * * * * * * * * * * * * * * * *
C     SUBROUTINE PROC FOR PROGRAM CALLED PATERN
C     PURPOSE:  TO ESTIMATE MASS TRANSFER
C     COEFFICIENTS FROM POSITION -VS- OXYGEN
C     CONCENTRATION VALUES
* * * * * * * * * * * * * * * * * * * * * * * * * * * * * * * * * * * *
C
C     MAIN PROGRAM
C
C
      IMPLICIT DOUBLE PRECISION(A-H,O-Z)
      INTEGER NDATA,NP,NPASS,IO
      character*20 dfile
      DIMENSION P(10), STEP(10)
      CHARACTER CONCEN*20
      COMMON /param/ c(100),z(100),dax,el,eg,es,zl,ul,zh,
     $            pt,ndata,cin
      common/expt/ conc(100)
C
C     SEARCH INITIALIZATION
      P(1)=.01d0
C     p(2)=.06d0
      STEP(1)=p(1)*.1d0
C     step(2)=p(2)*.1d0
C     NP=2
      np=1
      NPASS=3
```

```
      IO=3
C
C     READ IN DATA
C
C
C      write(*,*)'enter data file name'
C      read(*,*) dfile
      OPEN(UNIT=20,FILE=' ',STATUS='OLD')
      zh = .02464
      write(*,*)'enter gas and solid fractions, and inlet conc(mg/L)'
      read(*,*) eg,es,cin
      el = 1.0d0 -(eg+es)
      cin=cin/100.0d0*8.26d0
C      write(*,*)'enter the room pressure (atm) and column
     $     length (m)'
C      read(*,*) pt,zl
      pt=1.0d0
      zl=0.85d0
      write(*,*)'enter the axial dispersion coefficient and superficial
     $ liquid velocity'
      read(*,*) dax,ul
      do 10 i=1,100
        read(20,*) z(i),c(i)
        ndata = i-1
        if(z(i).lt.0.d0) goto 20
10     continue

C
C
C
      WRITE(*,*)
      WRITE(*,*)'CONCENTRATION(g/L)        TIME(MIN)'
20     DO 150 J=1,NDATA
        WRITE(*,350)C(J),Z(J)
350       FORMAT(6X,F6.2,18X,F6.2)
150    CONTINUE
C
C
C     START SEARCH
C
      CALL PATERN(NP,P,STEP,NPASS,IO,COST)
C
C     SEARCH COMPLETE, PRINT RESULTS
C     PRINT 300, P(1), P(2), COST
C300   FORMAT(F10.3,10X,F10.3)
      OPEN (UNIT=30,FILE='FOR30.DAT',STATUS='NEW')
      do 500 i=1,ndata
        WRITE (30,*)z(i),conc(i)
500    continue
300    FORMAT(E10.3,5X,F6.3,5X,E10.3)
      STOP
      END
C
```

```
C
C
C     THIS FILE IS A PAIR OF SUBROUTINES WRITTEN TO BE
C     COMPATIBLE WITH THE OPTIMIZATION SUBROUTINE
C     PATERN.  THEY SIMULATE A PROCESS USING DISCRETE
C     DIFFERENCE EQUATIONS AND COMPARE THE
C     SIMULATION OUTPUT WITH THE ACTUAL OUTPUT
C     (READ IN THROUGH A DATA FILE), CALCULATING AN
C     ERROR OR "COST" ASSOCIATED WITH THAT
C     SIMULATION.  PATERN USES THESE SUBROUTINES
C     ITERATIVELY IN ORDER TO FIND THE OPTIMUM SET OF
C     TRANSFER FUNCTION PARAMETERS TO FIT THE DATA.
C
C
      SUBROUTINE PROC(P,COST)
      IMPLICIT DOUBLE PRECISION (A-H,O-Z)
      DIMENSION P(10), STEP(10), CONC(100),pos(100)
      dimension xfinal(100),yfinal(2,100)
      COMMON /param/ c(100),z(100),dax,el,eg,es,zl,ul,zh,
     $             pt,ndata,cin
      common /expt/ conc
C     common /data/ pe,st,a,b

C     INITIALIZE ARRAYS AND DEFINE PARAMETERS
C
      zkla=P(1)
C       ul=p(2)
      ERROR=0.0
      TOTAL=0.0
C
      gamma=(es*1700+el*1000+eg*11.8)*9.80*(zl)
     $     /(pt*1.01325e5)
C       write(*,*)'gamma'
      pe=ul*zl/(dax*el)
      st=zkla*zl/ul
      a=pt*.21/zh*(1+gamma)
      b=-(pt*.21/zh)*gamma
C       write(*,*)'pe=',pe,'st=',st,'a=',a,'b=',b,'cin=',cin
      capb=(a-cin-(b/st))*pe-b
      r1=pe/2*(1+(1+4*st/pe)**0.5)
      r2=pe/2*(1-(1+4*st/pe)**0.5)
      capn=r1**2*exp(r1)-r2**2*exp(r2)
      a1=(capb*r2*exp(r2)-b*r1)/capn
      a2=(-capb*r1*exp(r1)+b*r2)/capn
C     write(*,*)'capn=',capn, 'a1=',a1,'a2=',a2
c     if(a1.lt.0.0) then
C       a1=abs(a1)
C       a1=-exp(log(a1)-capn)
C      else
C       a1=exp(log(a1)-capn)
C      endif
C      if(a2.lt.0.0) then
C       a2=abs(a2)
```

```
C       a2=-exp(log(a2)-capn)
C      else
C       a2=exp(log(a2)-capn)
C      endif
C      write(*,*)'st=',st,'pe=',pe,'capn=',capn
C     write(*,*)'a=',a,'b=',b,'capb=',capb,'r1=',r1,'r2=',r2
C      write(*,*) 'before call'
c      write(*,*)'a1=',a1,'a2=',a2,'gamma=',gamma
      do 10 i=1,ndata
        pos(i)=z(i)
        conc(i)=a1*exp(r1*pos(i))+a2*exp(r2*pos(i))
     $    +a-(b/st)+b*pos(i)
        err=(conc(i)-c(i))**2
        error=error+err
10     continue
      error=(error/(ndata-1))**0.5
      cost=error
      return
      END
C
C
C
      SUBROUTINE BOUNDS(P,IOUT)
      IMPLICIT DOUBLE PRECISION (A-H,O-Z)
      DIMENSION P(10), STEP(10)
      COMMON /param/ c(100),z(100),dax,el,eg,es,zl,ul,zh,
     $           pt,ndata,cin
      IOUT=0
C      IF(P(1).LE.0.or.p(2).le.0) IOUT=1
      if(p(1).le.0) iout = 1
      RETURN
      END
```

B.6 Diffusion Coefficients

```
* * * * * * * * * * * * * * * * * * * * * * * * * * * * * * * * * *
C     SUBROUTINE PROC FOR PROGRAM CALLED PATERN
C
C     PURPOSE: TO ESTIMATE DIFFUSION COEFFICIENTS BY
C              READING IN DATA CONTAINING TIME -VS-
C                CONCENTRATION  VALUES.
* * * * * * * * * * * * * * * * * * * * * * * * * * * * * * * * * *
C
C     MAIN PROGRAM
      IMPLICIT DOUBLE PRECISION(A-H,O-Z)
      INTEGER NDATA,NP,NPASS,IO
      COMMON C(4000), T(4000), Q(10000), NDATA, X, NQ, R
      COMMON NTYPE, XB
      DIMENSION P(10), STEP(10)
      CHARACTER CONCEN*20
C
C     SEARCH INITIALIZATION
```

```
      P(1)=2.0E-4
      P(2)=2.00
      STEP(1)=1.0E-4
      STEP(2)=0.1
      NP=2
      NPASS=3
      IO=3
C
C     READ IN DATA
C
5     WRITE(*,*)'WHAT TYPE OF DIFFUSION PROBLEM DO
     $    YOU WISH TO'
      WRITE(*,*)'SOLVE? ENTER THE NUMBER FOR THE
     $    DESIRED TYPE.'
      WRITE(*,*)
      WRITE(*,*)'1.  DIFFUSION FROM LIQUID INTO
     $    INITIALLY'
      WRITE(*,*)'   SOLUTE FREE SPHERES.'
      WRITE(*,*)'2.  DIFFUSION FROM SPHERES INTO
     $    INITIALLY'
      WRITE(*,*)'   SOLUTE FREE LIQUID.'
      READ(*,*) NTYPE
      WRITE(*,*)
C
      IF(NTYPE.EQ.1) THEN
        WRITE(*,*)'ENTER INITIAL LIQUID CONCENTRATION
     $       IN g/L'
        READ(*,*) X
        WRITE(*,*)
      ELSEIF(NTYPE.EQ.2) THEN
        WRITE(*,*)'ENTER INITIAL BEAD CONCENTRATION IN
     $       g/L'
        READ(*,*) XB
        WRITE(*,*)
      ELSE
        WRITE(*,*)'YOU DID NOT ENTER A 1 OR A 2. TRY
     $       AGAIN'
        WRITE(*,*)
        GOTO 5
      ENDIF
C
      WRITE(*,*)'ENTER THE NAME OF THE
     $    TIME-CONCENTRATION FILE'
      WRITE(*,*)'AND THE NUMBER OF DATA POINTS'
      READ(*,*) CONCEN, NDATA
      WRITE(*,*)
C
      OPEN(UNIT=20,FILE=CONCEN,STATUS='OLD')
C
C
      WRITE(*,*)'ENTER THE NUMBER OF Q VALUES DESIRED'
      READ(*,*) NQ
      WRITE(*,*)
```

```
      WRITE(*,*)'ENTER THE RADIUS OF THE BEADS'
      READ(*,*) R
      WRITE(*,*)
C
      WRITE(*,*)
      WRITE(*,*)'CONCENTRATION(g/L)       TIME(MIN)'
      DO 150 J=1,NDATA
        READ(20,*)t(J),c(J)
        WRITE(*,350)C(J),T(J)
350       FORMAT(6X,F6.2,18X,F6.2)
150    CONTINUE
C
C
C     START SEARCH
C
      CALL PATERN(NP,P,STEP,NPASS,IO,COST)
C
C     SEARCH COMPLETE, PRINT RESULTS
C     PRINT 300, P(1), P(2), COST
C300   FORMAT(F10.3,10X,F10.3)
      OPEN (UNIT=30,FILE='FOR30.DAT',STATUS='NEW')
      WRITE (30,300) P(1),COST
300    FORMAT(E10.3,5X,F6.3,5X,E10.3)
      STOP
      END
C
C
C
C     THIS FILE IS A PAIR OF SUBROUTINES WRITTEN TO BE
C     COMPATIBLE WITH THE OPTIMIZATION SUBROUTINE
C     PATERN.  THEY SIMULATE A PROCESS USING DISCRETE
C     DIFFERENCE EQUATIONS AND COMPARE THE
C     SIMULATION OUTPUT WITH THE ACTUAL OUTPUT
C     (READ IN THROUGH A DATA FILE), CALCULATING AN
C     ERROR OR "COST" ASSOCIATED WITH THAT
C     SIMULATION.  PATERN USES THESE SUBROUTINES
C     ITERATIVELY IN ORDER TO FIND THE OPTIMUM SET OF
C     TRANSFER FUNCTION PARAMETERS TO FIT THE DATA.
C
C
      SUBROUTINE PROC(P,COST)
      IMPLICIT DOUBLE PRECISION (A-H,O-Z)
      COMMON C(4000), T(4000), Q(10000), NDATA, X, NQ, R
      COMMON NTYPE, XB
      DIMENSION P(10), STEP(10), CONC(100)
C
C     INITIALIZE ARRAYS AND DEFINE PARAMETERS
C
      D=P(1)
      ALPHA = P(2)
      ERROR=0.0
      TOTAL=0.0
C
```

```
C     PURPOSE: TO CALCULATE THE Q VALUES BASED ON THE
     $     ALPHA GIVEN
C
      alow = 0.0
      aloval = tan(alow)-3*alow/(3+alpha*alow**2)
      j = 0
      FINC = 0.001
      kount = 0
      q(1) = 0.0
      do 5 k=2,nq+1
2       up = alow + FINC
        hival = tan(up)-3*up/(3+alpha*up**2)
        if(hival.lt.0.0.and.aloval.gt.0.0) j=j+1
        if(aloval.lt.0.0.and.hival.gt.0.0) j=j+1
        if(j.eq.2) goto 11
        alow = up
        aloval = hival
        goto 2
11    if(kount.gt.500) then
        FINC = FINC/10
        alow = q(k-1) + FINC
        aloval = tan(alow)-3*alow/(3+alpha*alow**2)
        j = 0
        goto 2
      endif
      aloval = tan(alow)-3*alow/(3+alpha*alow**2)
      if(aloval.lt.0.0) then
        flagl = 0
      else
        flagl = 1
      endif
      hival = tan(up)-3*up/(3+alpha*up**2)
      if(hival.lt.0.0) then
        flagh = 0
      else
       flagh = 1
      endif
      if(flagl.eq.0.and.flagh.eq.1) then
        guess = (up - alow)/2. + alow
        amidval = tan(guess)-3*guess/(3+alpha*guess**2)
        if(abs(amidval).lt.1.0e-8) goto 100
        kount = kount + 1
        if(amidval.lt.0.0) then
          alow = guess
          goto 11
        else
          up = guess
          goto 11
        endif
      else
        guess = (up - alow)/2. + alow
        amidval = tan(guess)-3*guess/(3+alpha*guess**2)
        if(abs(amidval).lt.1.0e-8) goto 100
```

```
      kount = kount + 1
      if(amidval.lt.0.0) then
        up = guess
        goto 11
      else
        alow = guess
        goto 11
      endif
    endif
100   q(k) = guess
    kount = 0
    alow = guess+ FINC
    aloval = tan(alow)-3*alow/(3+alpha*alow**2)
    j=0
5    continue
C
C     CALCULATE COST
C
    IF(NTYPE.EQ.1) THEN
    DO 20 J=1,NDATA
        DO 10 I=2,NQ+1
            TERM1=(6*(1+ALPHA)*EXP(-D*Q(I)
   $          **2*T(J)/R**2))
            TERM=TERM1/(9+9*ALPHA+Q(I)
   $          **2*ALPHA**2)
            TOTAL=TOTAL+TERM
10       CONTINUE
        CONC(J)=((X*ALPHA)/(1+ALPHA))*(1+TOTAL)
        ERR=(C(J)-CONC(J))**2
        ERROR=ERROR+ERR
        COST=(error/(ndata-2))**0.5
        TOTAL=0.0
20    CONTINUE
    GOTO 300
    ELSE
    DO 30 J=1,NDATA
        DO 40 I=2,NQ+1
            TERM1=(6*(1+ALPHA)*EXP(-D*Q(I)
   $          **2*T(J)/R**2))
            TERM=TERM1/(9+9*ALPHA+Q(I)
   $          **2*ALPHA**2)
            TOTAL=TOTAL+TERM
40       CONTINUE
        CONC(J)=(XB/(1+ALPHA))*(1-TOTAL)
        ERR=ABS((C(J)-CONC(J))/conc(j))
        ERROR=ERROR+ERR
        COST=ERROR
        TOTAL=0.0
30    CONTINUE
    ENDIF
300   RETURN
    END
C
```

```
C
C
      SUBROUTINE BOUNDS(P,IOUT)
      IMPLICIT DOUBLE PRECISION (A-H,O-Z)
      COMMON C(4000),T(4000),Q(10),NDATA, X, NQ, R
      COMMON NTYPE, XB
      DIMENSION P(1), STEP(1)
      IOUT=0
      IF(P(1).LT.0.OR.P(2).LT.0) IOUT=1
      RETURN
      END
```

B.7 Fluidized Bed Simulation

```
* * * * * * * * * * * * * * * * * * * * * * * * * * * * * * * *
C     THIS PROGRAM SIMULATES A FLUIDIZED BED USING
C     A STIRRED TANK IN SERIES MODEL AND PREDICTS
C     BED BEHAVIOR WHEN A PULSE IS APPLIED.  THE
C     DISPERSION COEFFICIENT OF THE SIMULATED SYSTEM
C    IS DETERMINED IN THE SECOND HALF OF THE PROGRAM
* * * * * * * * * * * * * * * * * * * * * * * * * * * * * * * *
     implicit double precision (a-h,o-z)
     common/pbparm/pm(20)
     common/counter/i,nprob1,nprob2
     open(1,file='file4.csv',status='old')
     open(2,file='file5.csv',status='old')
     open(3,file='file6.csv',status='old')
     open(6,file='tank4.csv',status='new')
     open(7,file='tank5.csv',status='new')
     vb=0.00196d0
     write(*,*)'how many tanks do you want'
     read(*,*)ntank
     tankvol=vb/ntank
     write(*,*)'enter velocity,bead radius, and bead porosity'
     read(*,*)u,br,ep
     a=.00196d0
     write(*,*)'enter the gas void fraction'
     read(*,*)eg
     write(*,*)'enter solid  fraction, and diffusion coefficient'
     read(*,*)es,de
     eb = 1.0d0-(eg+es)
     write(3,*)u
     write(3,*)a
     write(3,*)br
     write(3,*)ep
     write(3,*)tankvol
     write(3,*)es
     write(3,*)de
     write(3,*)eg
     nprob1=6*ntank/10
     nprob2=9*ntank/10
     close(3)
```

```
      call norsig
      call fouexp
      call rdparm(pm)
      do 10 i=1,ntank
        call precur
10    continue
      close(8)
      close(7)
      call disp1
      stop
      end

      subroutine norsig
      implicit double precision (a-h,o-z)
      common /signal/toin,dtin,nin,cin(200)
      dimension cdin(5000)
c     write(6,610)
      call rdsigl(toin,dtin,nin,cdin)
      call normlz(dtin,nin,cdin,ain,cin)
      call print(toin,dtin,nin,cdin,ain,cin)
      return

610   FORMAT(/1H0,'*** MEASURED SIGNALS ***')
      end

      subroutine rdsigl(to,dt,n,cd)
      implicit double precision (a-h,o-z)
      dimension cd(200),cwork(10)
      read(1,*) to, dt
c     write(6,600) to, dt
c     if(to.lt.0.d0) write(6,610)
c     if(dt.le.0.0d0) write(6,620)
      n=0
1     do 900 i=1,10
        read(1,*,end=90) cwork(i)
c       write(6,630)     cwork(i)
        if (cwork(i).lt.0.0d0) goto 5
900   continue
5     do 10 i=1,10
        n=n+1
        if(cwork(i).lt.0.0d0) return
        if(n.gt.200) goto 91
        cd(n)=cwork(i)
10    continue
      goto 1
90    write(6,640)
      stop
91    write(6,650)
      stop

100   format(2f10.0)
110   format(10f8.0)
600   format(1h0,5x,'to =',f10.5,5x,'dt =',f10.5/)
```

```
610   format(1h0,'starting time (to) is negative.'/)
620   format(1h0,'time interval (dt) is not positive.'/)
630   format(1h,10f8.2)
640   format(1h0,'end of data cannot be found. (sub.rdsigl)'/)
650   format(1ho,'number of data exceeds 200. (sub.rdsigl)'/)
      end

      subroutine normlz(dt,n,cd,area,cn)
      implicit double precision (a-h,o-z)
      dimension cd(200),cn(200)
      area = 0.0d0
      do 10 i=1,n
        area=area+cd(i)
10    continue
      area=area*dt
      if(area.eq.0.0d0) then
c       write(6,600)
        do 20 i=1,n
          cn(i)=cd(i)
20      continue
        return
      elseif(area.lt.0.0d0) then
c       write(6,610)
      endif
      do 30 i=1,n
        cn(i)=cd(i)/area
30    continue
      return

600   format(1h0,'area of curve is zero(returned signal is not normal
     $ized).'/)
610   format(1h0,'area of curve is negative.'/)
      end

      subroutine print(toin,dtin,nin,cdin,ain,cin)
      implicit double precision (a-h,o-z)
      dimension cdin(200),cin(200)
c     write(6,600)
c     write(6,610) toin,dtin,nin,ain
c     write(6,630)
      do 10 i=1,nin
        tin=toin +float(i-1)*dtin
c       write(6,650)i,tin,cdin(i),cin(i)
10    continue
      return

600   format(//1h0,'***** input and response signals *****'/1h0,10x
     $,6x,'starting time',5x,'time interval',5x,'no of data',5x,'area')
610   format(1h0,5x,' input ',4x,f10.4,7x,f10.4,8x,i5,5x,e13.5)
630   format(1h0,15x,'======== input
     $    ========',15x,'======== response
     $    ========'/1h,4x,'n',2(7x,'time     reading
     $    (normalized)'))
```

```
650  format(1h,i5,3x,f10.4,f10.4,3x,f10.5)
     end

     subroutine fouexp
     implicit double precision (a-h,o-z)
     common /signal/ toin,dtin,nin,cin(200)
     common/fdata/ tau,nterm,aoin,ain(200),bin(200)
     read(2,*) tau,nterm
c    write(6,600) tau, nterm
     if(tau.lt.(toin+dtin*float(nin))/2.0d0) then
       tau=(toin+dtin*float(nin))/2.0d0*1.5d0
c      write(6,610) tau
     endif
     if(nterm.lt.1.or.nterm.gt.idint(tau/dtin+0.5d0)) then
       nterm=idint(tau/dtin+0.5d0)
c      write(6,620) nterm
     endif
     if(nterm.gt.200) then
       nterm=200
c      write(6,620) nterm
     endif
c    write(6,630)
     call foucoe(toin,dtin,nin,cin,tau,nterm,aoin,ain,bin)
c    write(6,640)
     return

200  format(f10.0,i10)
600  format(//1h0,'***** fourier expansion *****'/1h0,5x,'half
    $period =',e13.5,5x,'no of terms=',i5)
610  format(1h0,'half period (tau) is replaced by',e15.7)
620  format(1h0,'number of terms (nterm) is replaced by',i5)
630  format(1h0,5x,'+++++ conversion check (input) +++++')
640  format(1h0,5x,'+++++ conversion check (response)
    $     +++++')
     end

     subroutine foucoe(to,dt,nt,cn,tau,nterm,ao,a,b)
     implicit double precision (a-h,o-z)
     dimension cn(200),a(200),b(200)
     data pi/3.141593d0/
     ao=0.0d0
     sq=0.0d0
     do 10 i=1,nt
       ao=ao+cn(i)
       sq=sq+cn(i)**2
10   continue
     ao=ao*dt/tau
     sq=sq*dt
c    write(6,600)
     cotest=ao/2.0d0
     sqtest=2.0d0*(ao/2.0d0)**2*tau
     do 20 n=1,nterm
       x=0.0d0
```

```
      y=0.0d0
      sv=float(n)*pi/tau
      do 30 i=1,nt
        z=sv*(to+float(i-1)*dt)
        x=x+cn(i)*cos(z)
        y=y+cn(i)*sin(z)
30     continue
      a(n)=x*dt/tau
      b(n)=y*dt/tau
      cotest=cotest+a(n)
      sqtest=sqtest+(a(n)**2+b(n)**2)*tau
      if(mod(n,10).eq.0) then
        rat=sqtest/sq
c        write(6,610) n,rat,cotest
      endif
20   continue
    return

600  format(1h0,10x,'no of terms',8x,'ratio',7x,'value at t=0')
610  format(1h,10x,i5,10x,f10.5,5x,f10.5)
    end

    subroutine rdparm(pm)
    implicit double precision (a-h,o-z)
    dimension pm(20)
    character*4 pname(8)
    data pname/'u   ','a   ','r   ','ep  ','vt  ','es  ',
   $       'ds  ','eg'/
    ip=8
    open(3,file='file6.csv',status='old')
    do 10 i=1,ip
      read(3,*) pm(i)
c      write(6,600)
c      write(6,*) i,pname(i),pm(i)
10   continue
    return

600  format(//1h0,'*****packed-bed parameters *****'/)
    end

    subroutine precur
    implicit double precision (a-h,o-z)
    common/signal/toin,dtin,nin,cin(200)
    common/fdata/tau,nterm,aoin,ain(200),bin(200)
    common/pbparm/ pm(20)
    common/counter/i,nprob1,nprob2
    dimension aclc(200),bclc(200)
    open(8,file='tank6.csv',status='new')
c    write(6,600)
    call clccoe(pm,tau,nterm,nt,aoin,ain,bin,aoclc,aclc,bclc)
    if(i.eq.nprob2) then
      write(7,*) nterm
      write(7,*) aoclc
```

```
      do 30 k=1,nterm
        write(7,*) aclc(k)
30     continue
      do 40 k=1,nterm
        write(7,*) bclc(k)
40     continue
    endif
    if(i.eq.nprob1) then
    write(8,*)nterm
    write(8,*)aoclc
    do 50 k=1,nterm
      write(8,*)aclc(k)
50   continue
    do 60 k=1,nterm
      write(8,*)bclc(k)
60   continue
    endif
    do 20 j=1,nterm
      ain(j)=aclc(j)
      bin(j)=bclc(j)
20   continue
    aoin=aoclc
    return

600   format(//1h0,'*****calculation of response curve *****')
    end

    subroutine clccoe(pm,tau,nterm,nt,aoin,ain,bin,aoclc,aclc,bclc)
    implicit double precision (a-h,o-z)
    dimension pm(20),ain(200),bin(200),aclc(200),bclc(200)
    data pi/3.141593d0/
    call transf(0,0.0d0,pm,an,bn)
    aoclc=aoin*an
    do 10 n=1,nterm
      w=float(n)*pi/tau
      call transf(1,w,pm,an,bn)
      aclc(n)=ain(n)*an+bin(n)*bn
      bclc(n)=bin(n)*an-ain(n)*bn
      if(an**2+bn**2.lt.1.0d-8) then
        nt=n
        return
      endif
10   continue
    nt=nterm
    return
    end

    subroutine transf(ictl,w,pm,an,bn)
    implicit double precision (a-h,o-z)
    dimension pm(20)
    save d1,d2,d3,d4,d5,e1
    complex*16 cs,cphi,cex,coth,cq,cf,c
    if(ictl.eq.0) then
```

```
      d1=pm(1)*pm(2)/((1.0d0-(pm(6)+pm(8)))*pm(5))
      d2=pm(7)*pm(4)*pm(6)*6.0d0/((1.0d0-(pm(6)
     $    +pm(8)))*pm(3)**2)
      d3=pm(1)*pm(2)/((1.0d0-(pm(6)+pm(8)))*pm(5))
      endif
      if(w.eq.0.0d0) then
        an=1.0d0
        bn=0.0d0
        return
      endif
      cs=dcmplx(0.0d0,w)
      cq=dcmplx(0.0d0,0.0d0)
      do 10 i=1,500
        sigma=3.1415927d0*real(i)/pm(3)
        alpha=pm(7)*sigma**2
        cq=cq+cs/(cs+alpha)
10    continue
      cf=d1/(cs+d1+d2*cq)
      an=cf
      bn=dimag(cf)
      return
      end

C     MAIN PROGRAM

      subroutine disp1
      implicit double precision (a-h,o-Z)
      INTEGER NDATA,NP,NPASS,IO
      integer ip, i, nin, nres, nterm
      common/main1/nterm,tau
      common /pbparm1/pm
      common/four/aoclcsig,aoclcres,aclcsig,bclcsig,aclcres,bclcres
      dimension pm(20),cdi(400),cwork(400),cdr(400),p(10),step(10)
      dimension aclcsig(500),bclcsig(500),aclcres(500),bclcres(500)
c     open(10,file='input4.csv',status='old')
      open(11,file='tank5.csv',status='old')
      open(12,file='input5.csv',status='old')
      open(13,file='tank6.csv',status='old')
      ip=9
      write(*,*)'L,U,a,eb,R,ep,Dax,De,eg'
      read(*,*) (pm(i), i=1,ip)
 300  format(8f10.4)
      read(13,*) nterm
      read(13,*)aoclcsig
      do 900 k=1,nterm
        read(13,*)aclcsig(k)
900   continue
      do 910 k=1,nterm
        read(13,*)bclcsig(k)
910   continue
      read(11,*)nterm
      read(11,*)aoclcres
      do 920 k=1,nterm
```

```
        read(11,*)aclcres(k)
920     continue
      do 930 k=1,nterm
        read(11,*)bclcres(k)
930     continue
      read(12,*)tau,nt

C     SEARCH INITIALIZATION
      do 1000 l=1,2
      if(l.eq.2) pm(8)=0.0d0
      P(1)= 0.08d0
      p(2)=8.0d-4
      STEP(1)=0.001d0
      step(2)=1.0d-5
      NP=2
      NPASS=3
      IO=3
C
C
C     START SEARCH
C
      CALL PATERN(NP,P,STEP,NPASS,IO,COST)
C
C     SEARCH COMPLETE, PRINT RESULTS
C     PRINT 399, P(1), P(2), COST
C399   FORMAT(F10.3,10X,F10.3)
      OPEN (UNIT=30,FILE='FOR35.DAT',STATUS='NEW')
      if(l.eq.1) write(*,*)'diffusion is not zero'
      if(l.eq.2) write(*,*)'diffusion is zero'
      WRITE (30,*) P(1),P(2),COST
399    FORMAT(E10.3,5X,F6.3,5X,E10.3,5x,E10.3)
1000   continue
      STOP
      END
C
C
C
C     THIS FILE IS A PAIR OF SUBROUTINES WRITTEN TO BE
C     COMPATIBLE WITH THE OPTIMIZATION SUBROUTINE
C     PATERN.  THEY SIMULATE A PROCESS USING DISCRETE
C     DIFFERENCE EQUATIONS AND COMPARE THE
C     SIMULATION OUTPUT WITH THE ACTUAL OUTPUT
C     (READ IN THROUGH A DATA FILE), CALCULATING AN
C     ERROR OR "COST" ASSOCIATED WITH THAT
C     SIMULATION.  PATERN USES THESE SUBROUTINES
C     ITERATIVELY IN ORDER TO FIND THE OPTIMUM SET OF
C     TRANSFER FUNCTION PARAMETERS TO FIT THE DATA.
C
C
      SUBROUTINE PROC(P,COST)
      implicit double precision (a-h,o-z)
      dimension p(10)
```

```
      common/pbparm1/pm(20)
      common/main3/error
      pm(2)=p(1)
      pm(7)=p(2)
      call precurl
      cost=error

       RETURN
       END
C
C
C
       SUBROUTINE BOUNDS(P,IOUT)
       implicit double precision (a-h,o-z)
       DIMENSION P(10), STEP(10)
       IOUT=0
       IF(P(1).LE.0.0) iout=1
       if(p(2).le.0.0) iout=1
       RETURN
       END
C
      subroutine precurl
      implicit double precision (a-h,o-z)
      common /main3/err
      common/main1/nterm,tau
      common/pbparm1/ pm(20)
      common/four/aoclcsig,aoclcres,aclcsig,bclcsig,aclcres,bclcres
      dimension aclcsig(500),bclcsig(500),aclcres(500),bclcres(500)
      dimension aclc(400),bclc(400)
      call clccoel(pm,tau,nterm,aoclcsig,aclcsig,bclcsig
     $          ,aoclc,aclc,bclc)
      x=2.0d0*(aoclcres/2.0d0-aoclc/2.0d0)**2
      y=2.0d0*(aoclcres/2.0d0)**2
      do 40 i=1,nterm
        x=x+(aclcres(i)-aclc(i))**2+(bclcres(i)-bclc(i))**2
        y=y+aclcres(i)**2+bclcres(i)**2
40    continue
      err = sqrt(x/y)
      return
      end

      subroutine clccoel(pm,tau,nterm,aoin,ain,bin,aoclc,aclc,bclc)
      implicit double precision (a-h,o-z)
      dimension pm(20),ain(400),bin(400),aclc(400),bclc(400)
      data pi/3.141593d0/
      call transfl(0,0.0d0,pm,an,bn)
      aoclc=aoin*an
      do 10 n=1,nterm
        w=float(n)*pi/tau
        call transfl(1,w,pm,an,bn)
        aclc(n)=ain(n)*an+bin(n)*bn
        bclc(n)=bin(n)*an-ain(n)*bn
        if(an**2+bn**2.lt.1.0d-8) then
```

```
        nt=n
        return
      endif
10   continue
     nt=nterm
     return
     end

     subroutine transfl(ictl,w,pm,an,bn)
     implicit double precision (a-h,o-z)
     dimension pm(20)
     save d1,d2,d3,d4,d5,e1
     complex*16 cs,cphi,cex,coth,cq,cf
     if(ictl.eq.0) then
       e1=pm(8)*pm(6)
       d1=pm(7)/(pm(1)*pm(2))
       d2=pm(1)/pm(2)
       d3=e1*pm(3)/(pm(4)*pm(5))
       if(pm(8).eq.0.0d0) then
         d4=0.0d0
       else
         d4=pm(6)/e1
       endif
       d5=pm(5)
     endif
     if(w.eq.0.0d0) then
       an=1.0d0
       bn=0.0d0
       return
     endif
     cs=dcmplx(0.0d0,w)
     if(d4.eq.0.0d0) then
       cf=cdexp(1.0d0/(2.0d0*d1)*(1.0d0-
    $    cdsqrt(1.0d0+4*d1*d2*cs)))
     else
       cphi=d5*cdsqrt(cs*d4)
       cex=cdexp(-2.0d0*cphi)
       coth=(1.0d0+cex)/(1.0d0-cex)
       cq=d3*(cphi*coth-1.0d0)
       cf=cdexp(1.0d0/(2.0d0*d1)*(1.0d0-cdsqrt(1.0d0+4*d1*d2
    $     *(cs+cq))))
     endif
     an=cf
     bn=dimag(cf)
     return
     end
```

Appendix C

Appendix C: Data Tables

Table C-1 Data from Figure 5-1

Current(Amps)	Experimental Field Strength (Gauss)	Predicted Field Strength (Gauss)
0	0	0
0.17		10
0.25	18	
0.34		20
0.4	31	
0.51		30
0.68		40
0.75	42	
0.85		50
1	60	
1.03		60
1.2		70
1.25	80	
1.37		80
1.5	90	
1.54		90
1.71		100
1.75	100	
1.88		110
2	120	
2.05		120
2.22		130
2.25	136	
2.39		140
2.5	150	
2.56		150
2.73		160
2.75	162	
2.9		170
3	180	
3.08		180
3.25	196	
3.25		190
3.42		200
3.5	209	
3.59		210
3.75	221	
3.76		220
3.93		230
4	243	
4.1		240
4.25	260	
4.27		250

Table C-1 (continued) Data from Figure 5-1

Current(Amps)	Experimental Field Strength (Gauss)	Predicted Field Strength (Gauss)
4.44	260	
4.5	271	
4.61		270
4.75	284	
4.78		280
4.9	297	
4.96		290
5.13		300

Table C-2 Data from Figure 5-2

Dimensionless Position	Experimental Field Strength (Gauss)	Predicted Field Strength (Gauss)
0.000	106.00	106.00
0.033		106.00
0.067		105.98
0.100		105.96
0.133		105.93
0.167		105.90
0.200		105.85
0.233		105.79
0.267		105.71
0.300		105.63
0.333	105.00	105.52
0.367		105.40
0.400		105.26
0.433		105.08
0.467		104.88
0.500		104.63
0.533		104.33
0.567		103.97
0.600		103.53
0.633		102.99
0.667	100.00	102.31
0.700		101.45
0.733		100.34
0.767		98.90
0.800		97.00
0.833	90.00	94.44
0.867		90.98
1.000	45.000	
1.133		23.67
1.167		18.18
1.200		14.13
1.233		11.16
1.267		8.95
1.300		7.30
1.333		6.03
1.367		5.05
1.400		4.28
1.433		3.67
1.467		3.17
1.500	15.00	2.76

Table C-3 Data from Figure 5-3

Gas Velocity (cm/s)	Field Strength (Gauss) at which regimes first appear				
	Random	Chain	Chain-channel	Destabilized	Frozen
0.6	10	50	60	80	110
1.1	10	50	75	110	180
2	20	80	110	180	270

Table C-4 Data from Figure 5-4

Gas Velocity (cm/s)	Field Strength (Gauss) at which regimes first appear				
	Random	Chain	Chain-channel	Destabilized	Frozen
0.6	10	40	90	110	150
1.1	20	60	90	120	300
2	30	90	110	130	

Table C-5 Data from Figure 5-5

Gas Velocity (cm/s)	Field Strength (Gauss) at which regimes first appear				
	Random	Chain	Chain-channel	Destabilized	Frozen
0.6	20	60	100	130	240
1.1	30	60	100	150	300
2	40	80	120	180	

Table C-6 Data from Figure 5-7

Field Strength (Gauss)	Gas Void Fraction at Gas velocities of 0.6 cm/s	1.1 cm/s	2.0 cm/s
0	0.0431	0.0719	0aw095
50	0.0294		
75		0.0610	0.0929
100	0.0083		
150	0.0223	0.0536	0.1011
200		0.0659	
225			0.1481
300	0.0060	0.2410	0.1400

Table C-7 Data from Figure 5-8

Field Strength (Gauss)	Gas Void Fraction at Gas velocities of 0.6 cm/s	1.1 cm/s	2.0 cm/s
0	0.0421	0.0702	0.1001
50	0.0401		
75		0.0594	0.0922
100	0.0520		
150	0.0527	0.0661	0.0879
200		0.1698	
225			0.1294
300	0.0066	0.1400	0.2288

Table C-8 Data from Figure 5-9

Field Strength (Gauss)	Gas Void Fraction at Gas velocities of 0.6 cm/s	1.1 cm/s	2.0 cm/s
0	0.0398	0.0652	0.0994
50	0.0378		
75		0.0608	0.0790
100	0.0381		
150	0.0335	0.0600	0.0905
200		0.0240	
225			0.1087
300	0.0355	0.0558	0.1255

Table C-9 Data from Figure 5-10

	Gas velocities 0.6 cm/s		1.1 cm/s		2.0 cm/s	
Field Strength (Gauss)	void fraction	95% confidence interval	void fraction	95% confidence interval	void fraction	95% confidence interval
0	0.0431	0.0104	0.0719	0.0026	0.1095	0.0068
50	0.0294	0.0129				
75			0.0610	0.0111	0.0929	0.012
100	0.0083	0.0068				
150	0.0223	0.0147	0.0536	0.0221	0.1011	0.0295
200			0.0659	0.0248		
225					0.1481	0.0176
300	0.0060	0.0186	0.241	0.0286	0.14	0.0707

Table C-10 Data from Figure 5-11

	Gas velocities					
	0.6 cm/s		1.1 cm/s		2.0 cm/s	
Field Strength (Gauss)	void fraction	95% confidence interval	void fraction	95% confidence interval	void fraction	95% confidence interval
0	0.0421	0.0109	0.0702	0.0075	0.1001	0.0084
50	0.0401	0.0147				
75			0.0594	0.0044	0.0922	0.0167
100	0.0520	0.0268				
150	0.0527	0.0223	0.0661	0.0088	0.0879	0.0181
200			0.1698	0.0244		
225					0.1294	0.0568
300	0.0066	0.0160	0.14	0.0925	0.2288	0.0798

Table C-11 Data from Figure 5-12

	Gas velocities					
	0.6 cm/s		1.1 cm/s		2.0 cm/s	
Field Strength (Gauss)	void fraction	95% confidence interval	void fraction	95% confidence interval	void fraction	95% confidence interval
0	0.0398	0.0044	0.0652	0.0128	0.0994	0.0065
50	0.0378	0.0115				
75			0.0608	0.0081	0.0790	0.0129
100	0.0381	0.0157				
150	0.0335	0.0074	0.0600	0.0162	0.0905	0.0137
200			0.0240	0.0138		
225					0.1087	0.0175
300	0.0355	0.0268	0.0558	0.0120	0.1255	0.0438

Table C-12 Data from Figure 5-13

Gas Void Fraction Measured By Two Techniques			
Field Strength = 0 Gauss		Field Strength = 270 Gauss	
ϵ_g (Probe)	ϵ_g (Valve)	ϵ_g (Probe)	ϵ_g (Valve)
0.0210	0.0350	0.0170	0.1400
0.0360	0.0650	0.0330	0.1930
0.0550	0.0900	0.0440	0.0060

Table C-13 Data from Figure 5-14

Experimental Data from Probe 1					
Time(s)	Voltage (Volts)	Time(s)	Voltage (Volts)	Time(s)	Voltage (Volts)
0	0	5.3	0.10014	10.6	0.00794
0.1	0.00313	5.4	0.10014	10.7	0.00794
0.2	0.00951	5.5	0.10489	10.8	0.00632
0.3	0.01745	5.6	0.09695	10.9	0.00794
0.4	0.03496	5.7	0.08581	11	0.00951
0.5	0.0461	5.8	0.08738	11.1	0.00951
0.6	0.05879	5.9	0.089	11.2	0.00794
0.7	0.06993	6	0.09057	11.3	0.00794
0.8	0.10489	6.1	0.08262	11.4	0.00632
0.9	0.12872	6.2	0.07787	11.5	0.00475
1	0.14461	6.3	0.07149	11.6	0
1.1	0.15737	6.4	0.07631	11.7	0.00475
1.2	0.16368	6.5	0.07312	11.8	0.00632
1.3	0.16687	6.6	0.06517	11.9	0.00632
1.4	0.16368	6.7	0.06036	12	0.00632
1.5	0.17006	6.8	0.0550	12.1	0.00475
1.6	0.18276	6.9	0.04922	12.2	0.00475
1.7	0.19389	7	0.05879	12.3	0.00313
1.8	0.19708	7.1	0.05404	12.4	0
1.9	0.19233	7.2	0.04922	14.5	0.01074
2	0.1907	7.3	0.0461	14.6	0.01074
2.1	0.19389	7.4	0.04291	14.7	0.00917
2.2	0.20184	7.5	0.04291	14.8	0.00766
2.3	0.19865	7.6	0.0556	14.9	0.00766
2.4	0.19708	7.7	0.04128	15	0.00458
2.5	0.20027	7.8	0.03177	15.1	0.00609
2.6	0.20184	7.9	0.03015	15.2	0.00609
2.7	0.20184	8	0.03015	15.3	0.00766
2.8	0.20027	8.1	0.02858	15.4	0.00609
2.9	0.20027	8.2	0.02702	15.5	0.00609

Table C-13 (continued) Data from Figure 5-14

Experimental Data from Probe 1					
Time(s)	Voltage (Volts)	Time(s)	Voltage (Volts)	Time(s)	Voltage (Volts)
3	0.20184	8.3	0.02383	15.6	0.00609
3.1	0.19865	8.4	0.02858	15.7	0.00458
3.2	0.19233	8.5	0.02858	15.8	0.00458
3.3	0.18751	8.6	0.02858	15.9	0.00301
3.4	0.18276	8.7	0.02383	16	0
3.5	0.17482	8.8	0.0222		
3.6	0.17163	8.9	0.0222		
3.7	0.16687	9	0.02064		
3.8	0.16212	9.1	0.01908		
3.9	0.15737	9.2	0.01908		
4	0.15255	9.3	0.01589		
4.1	0.14942	9.4	0.01426		
4.2	0.13666	9.5	0.01589		
4.3	0.13985	9.6	0.01426		
4.4	0.11921	9.7	0.0127		
4.5	0.11127	9.8	0.01113		
4.6	0.10645	9.9	0.01145		
4.7	0.1144	10	0.0127		
4.8	0.13347	10.1	0.01113		
4.9	0.11602	10.2	0.0127		
5	0.10489	10.3	0.01589		
5.1	0.1017	10.4	0.0127		
5.2	0.1017	10.5	0.00951		

Experimental Data from Probe 2					
Time(s)	Voltage (Volts)	Time(s)	Voltage (Volts)	Time(s)	Voltage (Volts)
2	0	7.3	0.12414	12.6	0.0184
2.1	0.00766	7.4	0.12414	12.7	0.01532
2.2	0.01224	7.5	0.12263	12.8	0.01532
2.3	0.01532	7.6	0.11497	12.9	0.00766
2.4	0.01991	7.7	0.10882	13	0.01224
2.5	0.02606	7.8	0.10267	13.1	0.01074
2.6	0.03372	7.9	0.09965	13.2	0.01074
2.7	0.04289	8	0.09808	13.3	0.01074
2.8	0.05362	8.1	0.09657	13.4	0.01532
2.9	0.06895	8.2	0.09657	13.5	0.01375
3	0.08427	8.3	0.09193	13.6	0.01532
3.1	0.09808	8.4	0.08891	13.7	0.01224
3.2	0.10731	8.5	0.08125	13.8	0.01074
3.3	0.11956	8.6	0.07661	13.9	0.00917
3.4	0.12872	8.7	0.07818	14	0.01532

Table C-13 (continued) Data from Figure 5-14

Experimental Data from Probe 2					
Time(s)	Voltage (Volts)	Time(s)	Voltage (Volts)	Time(s)	Voltage (Volts)
3.5	0.13488	8.8	0.08125	14.1	0.00917
3.6	0.13795	8.9	0.08125	14.2	0.00766
3.7	0.14254	9	0.0751	14.3	0.00917
3.8	0.14103	9.1	0.07052	14.4	0.01074
3.9	0.14411	9.2	0.07052		
4	0.1502	9.3	0.07661		
4.1	0.15478	9.4	0.07661		
4.2	0.15786	9.5	0.06744		
4.3	0.15786	9.6	0.06436		
4.4	0.15635	9.7	0.06436		
4.5	0.15786	9.8	0.06286		
4.6	0.15786	9.9	0.05978		
4.7	0.15943	10	0.05212		
4.8	0.15328	10.1	0.05212		
4.9	0.16094	10.2	0.04747		
5	0.16401	10.3	0.04446		
5.1	0.16251	10.4	0.04596		
5.2	0.15478	10.5	0.04138		
5.3	0.15478	10.6	0.05362		
5.4	0.15478	10.7	0.04289		
5.5	0.15478	10.8	0.03981		
5.6	0.1502	10.9	0.03523		
5.7	0.15177	11	0.03523		
5.8	0.15328	11.1	0.03981		
5.9	0.15177	11.2	0.04138		
6	0.1502	11.3	0.0383		
6.1	0.1471	11.4	0.0368		
6.2	0.14562	11.5	0.03523		
6.3	0.14411	11.6	0.02907		
6.4	0.13946	11.7	0.02606		
6.5	0.13337	11.8	0.02757		
6.6	0.1318	11.9	0.02907		
6.7	0.13029	12	0.02757		
6.8	0.12263	12.1	0.02606		
6.9	0.12414	12.2	0.01991		
7	0.12722	12.3	0.01683		
7.1	0.13029	12.4	0.0184		
7.2	0.12872	12.5	0.0184		

Table C-14 Data from Figure 5-15

Time (min)	Ca^{+2} Tracer Concentration (g/L) Experimental	One Parameter Fit	Two Parameter Fit
0.0	11.88	11.82	11.87
1.0	10.48	11.13	10.71
2.0	10.14	10.82	10.31
3.0	9.90	10.60	10.05
4.0	9.75	10.43	9.85
5.0	9.63	10.28	9.70
6.0	9.51	10.16	9.57
7.0	9.45	10.05	9.46
8.0	9.33	9.95	9.38
9.0	9.28	9.86	9.30
10.0	9.24	9.78	9.23
11.0	9.18	9.70	9.18
12.0	9.13	9.63	9.13
13.0	9.11	9.57	9.08
14.0	9.06	9.51	9.05
15.0	9.02	9.45	9.01
16.0	8.99	9.40	8.98
17.0	8.99	9.35	8.96
18.0	8.94	9.30	8.93
19.0	8.92	9.25	8.91
20.0	8.91	9.21	8.90
21.0	8.89	9.17	8.88
22.0	8.87	9.13	8.87
23.0	8.86	9.09	8.86
24.0	8.86	9.06	8.84
25.0	8.86	9.02	8.84
26.0	8.84	8.99	8.83
27.0	8.84	8.96	8.82
28.0	8.84	8.93	8.81
29.0	8.82	8.90	8.81
30.0	8.82	8.87	8.80
31.0	8.82	8.85	8.80
32.0	8.82	8.82	8.79
33.0	8.82	8.80	8.79
34.0	8.79	8.77	8.79
35.0	8.79	8.75	8.79
36.0	8.77	8.73	8.78
37.0	8.77	8.71	8.78
38.0	8.79	8.69	8.78
39.0	8.77	8.67	8.78
40.0	8.77	8.65	8.78
41.0	8.76	8.63	8.78
42.0	8.77	8.61	8.77
43.0	8.76	8.59	8.77
44.0	8.74	8.58	8.77

Table C-14 (continued) Data from Figure 5-15

Time (min)	Ca^{+2} Tracer Concentration (g/L) Experimental	One Parameter Fit	Two Parameter Fit
45.0	8.76	8.56	8.77
46.0	8.77	8.54	8.77
47.0	8.76	8.53	8.77
48.0	8.77	8.51	8.77
49.0	8.74	8.50	8.77
50.0	8.77	8.49	8.77
51.0	8.77	8.47	8.77
52.0	8.76	8.46	8.77
53.0	8.76	8.45	8.77
54.0	8.74	8.43	8.77
55.0	8.76	8.42	8.77
56.0	8.74	8.41	8.77
57.0	8.74	8.40	8.77
58.0	8.74	8.39	8.77
59.0	8.76	8.38	8.77
60.0	8.74	8.37	8.77

Table C-15 Data from Figure 5-16

Agitation Rate (rpm)	Diffusion Coefficient × 10^4 (cm^2/s)
0	2.51
50	5.13
100	5.66
240	5.6
290	5.72

Table C-16 Data from Figure 5-17

Molecular Diameter (Å)	Excluded Void Volume Distribution for 0% beads Experimental Data	Curve Fit Data
4	0	0.0025
10	0.0398	0.0188
12	0.0748	0.0255
38	0.1340	0.1446
51	0.2282	0.2215
61	0.2487	0.2845
90	0.4586	0.4623
118	0.5916	0.6022
204	0.8466	0.8230
270	0.9796	0.8826
560	0.8910	0.9364

Molecular Diameter (Å)	Excluded Void Volume Distribution for 5% beads Experimental Data	Curve Fit Data
4	0	0.0011
10	0.0741	0.0194
38	0.1388	0.1088
51	0.1533	0.1601
61	0.2340	0.2030
90	0.3202	0.3332
118	0.4403	0.4507
204	0.6746	0.6829
270	0.7872	0.7622
560	0.8341	0.8474

Molecular Diameter (Å)	Excluded Void Volume Distribution for 50% beads Experimental Data	Curve Fit Data
4	0	0
10	0.0421	0.0380
38	0.0757	0.0790
51	0.1074	0.1002
61	0.1672	0.1184
90	0.1800	0.1769
118	0.2111	0.2341
204	0.3402	0.3686
270	0.4355	0.4258
560	0.5287	0.4971

Table C-17a Data from Figure 5-18a

Pore Diameter (Å)	Porosity for Beads With Various Percentage Magnetite 0%	5%	50%
4	0.9339	0.8464	0.4971
10	0.9176	0.8281	0.4591
12	0.9109	0.8474	0.4971
38	0.7918	0.7386	0.4181
51	0.7148	0.6873	0.3969
61	0.6519	0.6445	0.3786
90	0.4741	0.5142	0.3202
118	0.3342	0.3967	0.2630
204	0.1133	0.1646	0.1284
270	0.0538	0.0852	0.0713
560	0.0000	0.0000	0.0000

Table C-17b Data from Figure 5-18b

Pore Diameter (Å)	Percent of Total Pore Volume Accessible (%) 0%	5%	50%
4	100.0	100.0	100.0
8	98.7	98.3	93.8
10	98.0	97.7	92.4
12	97.3	97.0	91.4
38	84.6	87.2	84.1
51	76.3	81.1	79.8
61	69.6	76.1	76.2
90	50.6	60.7	64.4
118	35.7	46.8	52.9
204	12.1	19.4	25.8
270	5.7	10.0	14.3
560	0.0	0.0	0.0

Table C-18 Data from Figure 5-19

Time(s)	Voltage	Predicted Data Time(s)	Voltage	Time(s)	Voltage	Time(s)	Voltage
0	0.00088	5.2	0.14232	10.5	0.0601	15.8	0.00913
0.1	0.00095	5.3	0.1421	10.6	0.0580	15.9	0.00878
0.2	0.00091	5.4	0.1419	10.7	0.0559	16	0.00844
0.3	0.00077	5.5	0.14172	10.8	0.05378	16.1	0.00812
0.4	0.00053	5.6	0.14153	10.9	0.05168	16.2	0.0078
0.5	0.00021	5.7	0.14134	11	0.04962	16.3	0.0075
0.6	0.00015	5.8	0.14109	11.1	0.04764	16.4	0.0072
0.7	0.00053	5.9	0.14077	11.2	0.04576	16.5	0.0069
0.8	0.00087	6	0.14035	11.3	0.04398	16.6	0.00661
0.9	0.00114	6.1	0.1398	11.4	0.04232	16.7	0.00632
1	0.0013	6.2	0.13909	11.5	0.04078	16.8	0.00604
1.1	0.00131	6.3	0.13822	11.6	0.03936	16.9	0.00576
1.2	0.00116	6.4	0.13719	11.7	0.03805	17	0.00549
1.3	0.00088	6.5	0.13599	11.8	0.03684	17.1	0.00523
1.4	0.000	6.6	0.13464	11.9	0.03573	17.2	0.00496
1.5	0.00015	6.7	0.13315	12	0.03469	17.3	0.0047
1.6	0.00072	6.8	0.13152	12.1	0.03372	17.4	0.00444
1.7	0.00124	6.9	0.12979	12.2	0.03281	17.5	0.00417
1.8	0.0016	7	0.12797	12.3	0.03193	17.6	0.00389
1.9	0.00168	7.1	0.12606	12.4	0.03109	17.7	0.00359
2	0.00134	7.2	0.12409	12.5	0.03028	17.8	0.00329
2.1	0.00046	7.3	0.12206	12.6	0.0295	17.9	0.00297
2.2	0.00108	7.4	0.11997	12.7	0.02874	18	0.00263
2.3	0.00338	7.5	0.11783	12.8	0.02801	18.1	0.00229
2.4	0.00654	7.6	0.11563	12.9	0.02731	18.2	0.00195
2.5	0.0106	7.7	0.11338	13	0.02663	18.3	0.0016
2.6	0.0156	7.8	0.11107	13.1	0.02597	18.4	0.00127
2.7	0.02152	7.9	0.10872	13.2	0.02534	18.5	0.00095
2.8	0.0283	8	0.10632	13.3	0.02473	18.6	0.00067
2.9	0.03586	8.1	0.10389	13.4	0.02413	18.7	0.00041
3	0.04407	8.2	0.10145	13.5	0.02355	18.8	0.0002
3.1	0.05278	8.3	0.09901	13.6	0.02297	18.9	0.00003
3.2	0.06182	8.4	0.09659	13.7	0.02238	19	0.00009
3.3	0.07101	8.5	0.09423	13.8	0.02178	19.1	0.00017
3.4	0.08015	8.6	0.09193	13.9	0.02116	19.2	0.0002
3.5	0.08905	8.7	0.08978	14	0.02052	19.3	0.0002
3.6	0.09754	8.8	0.08763	14.1	0.01985	19.4	0.00016
3.7	0.10547	8.9	0.08566	14.2	0.01915	19.5	0.0001
3.8	0.11272	9	0.08382	14.3	0.01843	19.6	0.00003
3.9	0.11918	9.1	0.0821	14.4	0.01769	19.7	0.00005
4	0.1248	9.2	0.08051	14.5	0.01693	19.8	0.00012
4.1	0.12956	9.3	0.07901	14.6	0.01616	19.9	0.00018

Table C-18 (continued) Data from Figure 5-19

Experimental Data					
Time(s)	Voltage	Time(s)	Voltage	Time(s)	Voltage
2.3	0	7.6	0.11401	12.9	0.02989
2.4	0.00426	7.7	0.10829	13	0.02989
2.5	0.00712	7.8	0.10257	13.1	0.02849
2.6	0.00998	7.9	0.09691	13.2	0.02849
2.7	0.01565	8	0.09831	13.3	0.02703
2.8	0.01991	8.1	0.09977	13.4	0.02703
2.9	0.01851	8.2	0.10257	13.5	0.02563
3	0.02563	8.3	0.10257	13.6	0.02563
3.1	0.03701	8.4	0.10257	13.7	0.02563
3.2	0.05131	8.5	0.10117	13.8	0.02563
3.3	0.06556	8.6	0.09977	13.9	0.02423
3.4	0.07694	8.7	0.09119	14	0.02423
3.5	0.08692	8.8	0.08546	14.1	0.02423
3.6	0.09691	8.9	0.08546	14.2	0.02423
3.7	0.10403	9	0.08692	14.3	0.02137
3.8	0.10829	9.1	0.08692	14.4	0.01991
3.9	0.11541	9.2	0.08692	14.5	0.01851
4	0.11967	9.3	0.08692	14.6	0.01138
4.1	0.11967	9.4	0.08406	14.7	0.0171
4.2	0.1268	9.5	0.0812	14.8	0.01138
4.3	0.13112	9.6	0.08546	14.9	0.00998
4.4	0.13252	9.7	0.08400	15	0.00998
4.5	0.13678	9.8	0.08546	15.1	0.01278
4.6	0.13824	9.9	0.0812	15.2	0.01565
4.7	0.13538	10	0.07122	15.3	0.01851
4.8	0.13398	10.1	0.06842	15.4	0.01991
4.9	0.13678	10.2	0.07554	15.5	0.0171
5	0.13678	10.3	0.07122	15.6	0.01424
5.1	0.13678	10.4	0.06696	15.7	0.01424
5.2	0.13964	10.5	0.0627	15.8	0.01278
5.3	0.1425	10.6	0.05844	15.9	0.01278
5.4	0.1439	10.7	0.05558	16	0.01278
5.5	0.14676	10.8	0.05558	16.1	0.01138
5.6	0.14536	10.9	0.05558	16.2	0.01138
5.7	0.1439	11	0.05412	16.3	0.00998
5.8	0.13964	11.1	0.05271	16.4	0.00852
5.9	0.12826	11.2	0.05271	16.5	0.00712
6	0.1268	11.3	0.05131	16.6	0.00852
6.1	0.12966	11.4	0.04985	16.7	0.00712
6.2	0.12399	11.5	0.04845	16.8	0.00712
6.3	0.1268	11.6	0.04845	16.9	0.00712
6.4	0.13112	11.7	0.04699	17	0.00712
6.5	0.13252	11.8	0.04273	17.1	0.00712
6.6	0.12399	11.9	0.03847	17.2	0.00712
6.7	0.12253	12	0.03135	17.3	0.00566
6.8	0.12399	12.1	0.02703	17.4	0.00566

Table C-18 (continued) Data from Figure 5-19

Experimental Data					
Time(s)	Voltage	Time(s)	Voltage	Time(s)	Voltage
6.9	0.12826	12.2	0.02703	17.5	0.00566
7	0.13112	12.3	0.02989	17.6	0.00566
7.1	0.13112	12.4	0.02423	17.7	0.00566
7.2	0.12399	12.5	0.03135	17.8	0.00566
7.3	0.12253	12.6	0.02989	17.9	0.00998
7.4	0.11827	12.7	0.02989		
7.5	0.11255	12.8	0.02989		

Table C-19 Data from Figure 5-20

	True and Apparent Peclet Numbers for Two Liquid Velocities			
Gas	U = 7.71 cm/s		U = 6.44 cm/s	
Velocity (cm/s)	Pe_{true}	Pe_{app}	Pe_{true}	Pe_{app}
0.6	0.1081	0.0850	0.0618	0.0544
1.1	0.0543	0.0504	0.0395	0.0347
2.0	0.0545	0.0499	0.0291	0.0267

Table C-20 Data from Figure 5-21

Field Strength	Peclet Numbers at Gas Velocities of		
(Gauss)	0.6 cm/s	1.1 cm/s	2.0 cm/s
0	0.1228	0.1549	0.0651
50	0.2098		
75		0.2279	0.1834
100	0.7678		
150	0.0910	0.4900	0.1837
200		0.0746	
225			0.1208
300	0.1603	0.1535	0.2080

Table C-21 Data from Figure 5-22

Field Strength (Gauss)	Peclet Numbers at Gas Velocities of 0.6 cm/s	1.1 cm/s	2.0 cm/s
0	0.1023	0.0675	0.0490
50	0.1446		
75		0.1595	0.1431
100	0.1153		
150	0.1252	0.1089	0.0771
200		0.1674	
225			0.1106
300	0.1160	0.1109	0.1432

Table C-22 Data from Figure 5-23

Field Strength (Gauss)	Peclet Numbers at Gas Velocities of 0.6 cm/s	1.1 cm/s	2.0 cm/s
0	0.1740	0.0873	0.0900
50	0.1809		
75		0.1419	0.2155
100	0.1340		
150	0.1677	0.1218	0.1036
200		0.1038	
225			0.1242
300	0.1421	0.1077	0.0713

Table C-23 Data from Figure 5-24

	Gas velocities					
	0.6 cm/s		1.1 cm/s		2.0 cm/s	
Field Strength (Gauss)	Pe number	95% confidence interval	Pe number	95% confidence interval	Pe number	95% confidence interval
0	0.1228	0.0386	0.1549	0.0343	0.0651	0.0243
50	0.2098	0.2482				
75			0.2279	0.0574	0.1834	0.0756
100	0.7678	0.3749				
150	0.0910	0.0234	0.4900	0.2201	0.1837	0.1311
200			0.0746	0.0347		
225					0.1208	0.0425
300	0.1603	0.0595	0.1535	0.0876	0.2080	0.1616

Table C-24 Data from Figure 5-25

	Gas velocities					
	0.6 cm/s		1.1 cm/s		2.0 cm/s	
Field Strength (Gauss)	Pe number	95% confidence interval	Pe number	95% confidence interval	Pe number	95% confidence interval
0	0.1022	0.0230	0.0675	0.0230	0.0490	0.0124
50	0.1446	0.0882				
75			0.1595	0.0957	0.1431	0.0938
100	0.1153	0.0832				
150	0.1252	0.0234	0.1089	0.0354	0.0771	0.0143
200			0.1674	0.3280		
225					0.1106	0.0207
300	0.1160	0.0659	0.1109	0.0650	0.1432	0.0670

Table C-25 Data from Figure 5-26

Field Strength (Gauss)	Gas velocities 0.6 cm/s void fraction	0.6 cm/s 95% confidence interval	1.1 cm/s void fraction	1.1 cm/s 95% confidence interval	2.0 cm/s void fraction	2.0 cm/s 95% confidence interval
0	0.1740	0.0126	0.0873	0.0276	0.0900	0.0309
50	0.1809	0.1436				
75			0.1419	0.0534	0.2155	0.0775
100	0.1340	0.0809				
150	0.1677	0.0374	0.1218	0.0665	0.1036	0.0108
200			0.1038	0.0171		
225					0.1242	0.0363
300	0.1421	0.1066	0.1077	0.0978	0.0713	0.0005

Table C-26 Data from Figure 5-27

Dimensionless Position	Aqueous O_2 Concentration (mg/L) Predicted	Experimental
0.000	0.2525	
0.059	0.3825	0.3769
0.118	0.5100	
0.176	0.6348	0.6055
0.235	0.7572	
0.294	0.8770	
0.353	0.9945	0.9580
0.412	1.1095	
0.471	1.2221	
0.529	1.3324	1.3632
0.588	1.4403	
0.647	1.5460	
0.706	1.6494	1.6687
0.765	1.7506	
0.824	1.8495	
0.882	1.9454	1.9415
0.941	2.0338	
1.000	2.0850	

Table C-27 Data from Figure 5-28

Field Strength (Gauss)	k_La Values at Gas Velocities of 0.6 cm/s	1.1 cm/s	2.0 cm/s
0	0.0188	0.0298	0.0393
75	0.0240	0.0391	0.0527
150	0.0198	0.0328	0.0454
225	0.0223	0.0342	0.0430
300	0.0239	0.0363	0.0456

Table C-28 Data from Figure 5-29

Field Strength (Gauss)	k_La Values at Gas Velocities of 0.6 cm/s	1.1 cm/s	2.0 cm/s
0	0.0184	0.0289	0.0397
75	0.0183	0.0290	0.0381
150	0.0180	0.0291	0.0394
225	0.0196	0.0306	0.0396
300	0.0203	0.0317	0.0387

Table C-29 Data from Figure 5-30

Field Strength (Gauss)	k_La Values at Gas Velocities of 0.6 cm/s	1.1 cm/s	2.0 cm/s
0	0.0188	0.0296	0.0397
75	0.0195	0.0337	0.0460
150	0.0200	0.0348	0.0462
225	0.0188	0.0292	0.0389
300	0.0177	0.0278	0.0348

Table C-30 Data from Figure 5-31

	Gas velocities					
	0.6 cm/s		1.1 cm/s		2.0 cm/s	
Field Strength (Gauss)	k_La	95% confidence interval	k_La	95% confidence interval	k_La	95% confidence interval
0	0.0188	0.0014	0.0298	0.0016	0.0393	0.0021
75	0.0240	0.0029	0.0391	0.0023	0.0527	0.0027
150	0.0198	0.0038	0.0328	0.0026	0.0454	0.0031
225	0.0223	0.0023	0.0342	0.0021	0.0430	0.0027
300	0.0239	0.0010	0.0363	0.0027	0.0456	0.0028

Table C-31 Data from Figure 5-32

	Gas velocities					
	0.6 cm/s		1.1 cm/s		2.0 cm/s	
Field Strength (Gauss)	k_La	95% confidence interval	k_La	95% confidence interval	k_La	95% confidence interval
0	0.0184	0.0018	0.0289	0.0002	0.0397	0.0004
75	0.0183	0.0004	0.0290	0.0009	0.0381	0.0012
150	0.0180	0.0010	0.0291	0.0005	0.0394	0.0009
225	0.0196	0.0012	0.0306	0.0022	0.0396	0.0011
300	0.0203	0.0032	0.0317	0.0015	0.0387	0.0032

Table C-32 Data from Figure 5-33

	Gas velocities					
	0.6 cm/s		1.1 cm/s		2.0 cm/s	
Field Strength (Gauss)	k_La	95% confidence interval	k_La	95% confidence interval	k_La	95% confidence interval
0	0.0188	0.0009	0.0296	0.0008	0.0397	0.0017
75	0.0195	0.0007	0.0337	0.0009	0.0460	0.0009
150	0.0200	0.0006	0.0348	0.0024	0.0462	0.0013
225	0.0188	0.0010	0.0292	0.0006	0.0389	0.0019
300	0.0177	0.0018	0.0278	0.0018	0.0348	0.0010

Table C-33 Data from Figure 5-34

$Pe_{true} = 20$			$Pe_{true} = 50$		
η	Φ_{app}	Pe_{app}	η	Φ_{app}	Pe_{app}
.9987	.858E-08	18.20	.9980	.380E-08	45.02
.9953	.886E-07	18.28	.9935	.394E-07	44.83
.9934	.225E-06	18.13	.9896	.999E-07	44.64
.9907	.356E-06	18.19	.9869	.159E-06	44.52
.9817	.144E-05	18.01	.9743	.643E-06	43.94
.9727	.327E-05	17.84	.9618	.147E-05	43.36
.9699	.438E-05	17.74	.9563	.197E-05	43.10
.9671	.468E-05	17.73	.9540	.210E-05	43.01
.9640	.587E-05	17.67	.9496	.264E-05	42.80
.9634	.588E-05	17.66	.9489	.264E-05	42.77
.9554	.926E-05	17.50	.9375	.418E-05	42.25
.9520	.106E-04	17.44	.9331	.478E-05	42.04
.9513	.115E-04	17.41	.9312	.520E-05	41.95
.9490	.119E-04	17.39	.9287	.540E-05	41.86
.9471	.135E-04	17.34	.9258	.610E-05	41.71
.9436	.150E-04	17.28	.9213	.681E-05	41.51
.9388	.185E-04	17.18	.9145	.841E-05	41.18
.9359	.202E-04	17.13	.9107	.919E-05	41.01
.9307	.244E-04	17.02	.9032	.111E-04	40.67
.9228	.311E-04	16.86	.8921	.143E-04	40.16
.9165	.372E-04	16.74	.8836	.171E-04	39.76
.9148	.397E-04	16.71	.8809	.183E-04	39.64
.9070	.470E-04	16.56	.8708	.217E-04	39.18
.9063	.502E-04	16.54	.8689	.231E-04	39.09
.8784	.876E-04	16.01	.8322	.409E-04	37.40
.8758	.104E-03	15.94	.8253	.488E-04	37.08
.8550	.160E-03	15.54	.7953	.760E-04	35.71
.8419	.166E-03	15.31	.7829	.790E-04	35.14
.8268	.277E-03	14.98	.7532	.134E-03	33.77
.7996	.460E-03	14.45	.7108	.228E-03	31.83
.7412	.200E-02	13.25	.5869	.111E-02	26.16

Table C-33 (continued) Data from Figure 5-34

Pe_{true} = 100			Pe_{true} = 200		
η	Φ_{app}	Pe_{app}	η	Φ_{app}	Pe_{app}
.9975	.164E-08	98.12	.9969	.815E-09	197.76
.9916	.170E-07	97.55	.9896	.847E-08	196.34
.9870	.431E-07	97.07	.9836	.215E-07	195.13
.9834	.686E-07	96.72	.9797	.342E-07	194.32
.9673	.279E-06	95.13	.9597	.140E-06	190.34
.9515	.638E-06	93.56	.9403	.321E-06	186.52
.9444	.857E-06	92.88	.9321	.432E-06	184.85
.9418	.917E-06	92.61	.9291	.462E-06	184.23
.9361	.115E-05	92.03	.9217	.582E-06	182.81
.9354	.115E-05	91.97	.9212	.583E-06	182.65
.9210	.183E-05	90.53	.9037	.928E-06	179.20
.9156	.210E-05	90.00	.8971	.106E-05	177.90
.9134	.228E-05	89.76	.8940	.116E-05	177.29
.9092	.238E-05	89.40	.8878	.121E-05	176.09
.9063	.268E-05	89.09	.8859	.136E-05	175.64
.9003	.300E-05	88.50	.8779	.153E-05	174.10
.8921	.371E-05	87.67	.8689	.189E-05	172.25
.8874	.406E-05	87.20	.8629	.207E-05	171.07
.8782	.492E-05	86.28	.8523	.252E-05	168.94
.8646	.633E-05	84.93	.8359	.325E-05	165.70
.8539	.760E-05	83.87	.8233	.392E-05	163.16
.8505	.813E-05	83.54	.8192	.420E-05	162.35
.8482	.850E-05	83.31	.8045	.501E-05	159.44
.8382	.968E-05	82.32	.8014	.536E-05	158.81
.8356	.104E-04	82.06	.7482	.971E-05	148.20
.7907	.185E-04	77.60	.7378	.117E-04	146.16
.7817	.221E-04	76.72	.6948	.186E-04	137.58
.7450	.349E-04	73.06	.6773	.195E-04	134.05
.7308	.364E-04	71.65	.6346	.339E-04	125.61
.6931	.625E-04	67.92	.5747	.600E-04	113.66
.6410	.108E-03	62.76	.3929	.352E-03	77.56
.4828	.577E-03	47.14	.3929	.352E-03	1.00

Table C-33 (continued) Data from Figure 5-34

Pe_{true} = 500			Pe_{true} = 1000		
η	Φ_{app}	Pe_{app}	η	Φ_{app}	Pe_{app}
.9864	.339E-08	491.73	.9835	.170E-08	982.31
.9796	.862E-08	488.21	.9741	.433E-08	972.46
.9732	.137E-07	485.14	.9664	.690E-08	965.24
.9478	.564E-07	472.26	.9350	.285E-07	933.86
.9227	.130E-06	459.80	.9046	.664E-07	903.58
.9126	.176E-06	454.84	.8943	.896E-07	892.57
.9082	.188E-06	452.72	.8883	.963E-07	886.70
.8989	.238E-06	447.93	.8771	.122E-06	875.21
.8984	.238E-06	447.61	.8762	.122E-06	874.61
.8758	.382E-06	436.48	.8494	.197E-06	847.71
.8677	.439E-06	432.28	.8400	.226E-06	838.53
.8648	.477E-06	430.78	.8363	.246E-06	835.32
.8539	.564E-06	425.38	.8235	.292E-06	821.79
.8506	.503E-06	423.97	.8106	.264E-06	809.66
.8404	.637E-06	418.76	.8024	.333E-06	800.96
.8323	.788E-06	414.63	.7983	.410E-06	796.75
.8235	.866E-06	410.34	.7865	.453E-06	785.09
.8117	.105E-05	404.37	.7739	.552E-06	772.47
.7913	.137E-05	394.27	.7502	.721E-06	748.88
.7763	.166E-05	386.64	.7325	.876E-06	731.23
.7705	.178E-05	383.87	.7267	.941E-06	725.41
.7521	.214E-05	374.53	.7034	.114E-05	701.61
.7492	.229E-05	373.04	.7017	.122E-05	700.42
.6821	.424E-05	339.56	.6205	.233E-05	619.15
.6727	.509E-05	334.98	.6153	.278E-05	614.22
.6215	.827E-05	309.47	.5596	.459E-05	557.90
.5942	.885E-05	295.59	.5179	.507E-05	516.30
.5517	.155E-04	274.59	.4838	.885E-05	482.35
.4838	.284E-04	240.64	.4118	.166E-04	410.59
.2851	.193E-03	141.58	.2127	.129E-03	211.79

Table C-33 (continued) Data from Figure 5-34

Pe_{true} = 1500			Pe_{true} = 2000		
η	Φ_{app}	Pe_{app}	η	Φ_{app}	Pe_{app}
.9941	.108E-09	1489.38	.9961	.813E-10	1987.80
.9806	.113E-08	1469.31	.9789	.852E-09	1955.87
.9723	.289E-08	1457.62	.9669	.218E-08	1934.56
.9619	.462E-08	1441.35	.9586	.348E-08	1915.17
.9267	.192E-07	1388.67	.9185	.145E-07	1835.46
.8925	.449E-07	1337.56	.8835	.340E-07	1765.47
.8816	.605E-07	1321.14	.8719	.460E-07	1740.95
.8728	.652E-07	1308.63	.8616	.496E-07	1722.52
.8607	.827E-07	1289.94	.8476	.630E-07	1694.51
.8594	.828E-07	1288.41	.8476	.630E-07	1693.90
.8299	.134E-06	1243.88	.8145	.102E-06	1627.93
.8201	.154E-06	1229.50	.8035	.118E-06	1606.36
.8182	.168E-06	1225.39	.8027	.128E-06	1601.79
.8012	.200E-06	1201.01	.7838	.153E-06	1566.73
.7811	.182E-06	1170.04	.7548	.141E-06	1509.05
.7739	.230E-06	1159.83	.7541	.217E-06	1507.41
.7733	.282E-06	1159.25	.7503	.178E-06	1500.45
.7600	.313E-06	1138.00	.7389	.241E-06	1475.52
.7473	.381E-06	1120.43	.7265	.294E-06	1452.44
.7234	.499E-06	1082.73	.6997	.386E-06	1398.99
.7042	.608E-06	1053.98	.6792	.472E-06	1357.98
.6971	.655E-06	1043.30	.6726	.508E-06	1344.68
.6703	.851E-06	1003.13	.6445	.663E-06	1288.56
.6693	.798E-06	1002.71	.6431	.623E-06	1284.72
.5789	.166E-05	866.69	.5487	.156E-05	1096.97
.5784	.197E-05	865.63	.5462	.132E-05	1090.24
.5196	.329E-05	777.61	.4900	.262E-05	977.37
.4674	.375E-05	698.74	.4286	.306E-05	855.15
.4414	.646E-05	660.54	.4106	.521E-05	818.96
.3684	.124E-04	551.32	.3376	.101E-04	673.42
.1749	.105E-03	261.27	.1502	.914E-04	298.92

Table C-34 Data from Figure 5-35

	Pe_{app}							
Φ_{app}	2000	1500	1000	500	200	100	50	20
.249E-04	1.000	1.000	1.000	1.000	1.000	1.000	1.000	1.000
.304E-04	1.000	1.000	1.000	1.000	1.000	1.000	1.000	1.000
.372E-04	1.000	1.000	.997	1.000	1.000	1.000	1.000	1.000
.454E-04	1.000	1.000	.995	1.000	1.000	1.000	1.000	1.000
.555E-04	1.000	.988	.990	1.000	1.000	1.000	1.000	1.000
.677E-04	1.000	.984	.987	1.000	1.000	1.000	1.000	1.000
.827E-04	1.000	.982	.987	1.000	1.000	1.000	1.000	1.000
.101E-03	1.000	.980	.985	1.000	1.000	1.000	1.000	.999
.123E-03	1.000	.977	.985	1.000	1.000	1.000	1.000	.999
.151E-03	.999	.977	.981	1.000	1.000	1.000	1.000	.997
.184E-03	.989	.975	.981	1.000	1.000	1.000	.999	.996
.225E-03	.976	.970	.982	1.000	1.000	1.000	.997	.995
.275E-03	.960	.962	.980	1.000	1.000	1.000	.996	.994
.335E-03	.941	.950	.974	1.000	1.000	.999	.990	.993
.410E-03	.917	.933	.964	.999	1.000	.998	.986	.992
.500E-03	.890	.913	.950	.991	1.000	.995	.983	.991
.611E-03	.857	.887	.931	.980	.997	.991	.981	.001
.912E-03	.776	.819	.878	.946	.979	.982	.978	.000
.111E-02	.727	.776	.843	.923	.967	.976	.976	.001
.166E-02	.610	.670	.754	.860	.933	.958	.970	.002
.248E-02	.465	.536	.638	.776	.885	.931	.959	.003
.370E-02	.288	.369	.490	.665	.818	.890	.938	.005
.552E-02	.078	.168	.310	.526	.731	.834	.906	.007
.823E-02			.092	.355	.619	.758	.859	.949
.101E-01				.257	.553	.713	.829	.933
.123E-01				.150	.481	.661	.794	.914
.150E-01				.033	.400	.603	.754	.891
.183E-01					.312	.539	.708	.863
.224E-01					.215	.468	.656	.830
.273E-01					.110	.389	.598	.792
.334E-01						.302	.533	.748
.408E-01						.208	.461	.698
.498E-01						.104	.382	.641
.608E-01							.295	.578
.743E-01							.199	.507
.907E-01							.095	.428
.111E+00								.342
.135E+00								.247

Table C-35 Data from Figure 5-36

Parameter	Φ_{app}	η	Pe_{app}
Bead Radius (m)			
.00200	.492E-05	.8782	86.28
.00025	.577E-03	.4828	47.14
.00050	.108E-03	.6410	62.76
.00100	.221E-04	.7817	76.72
.00300	.210E-05	.9156	90.00
.00400	.115E-05	.9354	91.97
Velocity (m/s)			
.10000	.238E-05	.9092	89.40
.08000	.300E-05	.9003	88.50
.06000	.406E-05	.8874	87.20
.03000	.850E-05	.8482	83.31
Bead Porosity			
.98000	.760E-05	.8539	83.87
.90000	.633E-05	.8646	84.93
.70000	.371E-05	.8921	87.67
.60000	.268E-05	.9063	89.09
.50000	.183E-05	.9210	90.53
.40000	.115E-05	.9361	92.03
.30000	.638E-06	.9515	93.56
.20000	.279E-06	.9673	95.13
.10000	.686E-07	.9834	96.72
.05000	.170E-07	.9916	97.55
Liquid Fraction			
.80000	.857E-06	.9444	92.88
.70000	.228E-05	.9134	89.76
.50000	.968E-05	.8382	82.32
.40000	.185E-04	.7907	77.60
.30000	.364E-04	.7308	71.65
.95000	.431E-07	.9870	97.07
.99000	.164E-08	.9975	98.12
Diffusion Coefficient (m^2/s)			
.5E-08	.625E-04	.6931	67.92
.3E-08	.349E-04	.7450	73.06
.1E-08	.104E-04	.8356	82.06
.8e-09	.813E-05	.8505	83.54
.1e-09	.917E-06	.9418	92.61

BIBLIOGRAPHY

BIBLIOGRAPHY

1. Chervenak, M.C., S. Feigelman, R. Wolk, C.R. Byrd, L.R. Hellwig, and R.P. Van Driesen. 1963. Hy-C cracking. **Chemical Engineering Progress. 59**(2):53.

2. Kielbach, A.W. 1959. The development of floating-bed scrubbers. **Chemical Engineering Progress Symposium Series. 57**(35):51.

3. Hellwig, K.C., H.C. Chervenak, E.S. Johanson, H.H. Stotler, and R.H. Wolk. 1968. Convert coal to liquid fuels with H-coal. **Chemical Engineering Progress Symposium Series. 64**:85-98.

4. Cooper, P.F., and B. Atkinson. 1981. **Biological Fluidized Bed Treatment of Water and Wastewater.** Ellis Horwood Publishers, Chichester, England.

5. Ostergaard, K. 1968. **Advances in Chemical Engineering.** T.B. Drew (ed.). Academic Press, New York. pp. 71-137.

6. Frijlink, J.J., and J.M. Smith. 1986. Coalescence in three phase systems. Proceedings of the International Conference on Bioreactor Fluid Dynamics, Cambridge, England. Paper no. 23. pp. 317-328.

7. Rosensweig, R.E. 1978. Process for operating a magnetically stabilized bed. U.S. Patent 4 115 927.

8. Rosensweig, R.E. 1979. Fluidization: hydrodynamics stabilization with a magnetic field. **Science. 204**(6):57-60.

9. Rosensweig, R.E., J.H. Siegell, W.K. Lee, and T. Mikus. 1981. Magnetically stabilized fluidized solids. **AIChE Symposium Series, 77**(205):8.

10. Ostergaard, K. 1971. Three-phase fluidization. In **Fluidization.** J.F. Davidson and D. Harrison (eds). Academic Press, New York. pp 751-778.

11. Filippov, M.V. 1960. The effect of a magnetic field on a ferromagnetic particle suspension bed. **Prik. Magnit. Lat. SSR. 12**:215.

12. Kirko, I.M. and M.V. Filippov. 1960. Standard correlations for

a fluidized bed of ferromagnetic particles in a magnetic field. **Zh. Tek. Fiz. 30**:1081.

13. Filippov, M.V. 1961. Resistance and expansion of a fluidized bed of ferromagnetic particles in a magnetic field. **Latv. PSR Zinat. Akad. Vestis. 12**(173):47.

14. Filippov, M.V. 1962. Some properties of a suspended bed of ferromagnetic particles in a magnetic field. **Voprosy Magnitnoi Gidrodinamiki I Dinamiki Plazmy.** 635.

15. Filoppov, M.V. 1962. Fluidization of a suspended layer of magnetite in a magnetic field. **Latv. PSR Zinat. Akad. Vestis. 1**(174):69.

16. Siegell, J.H. 1989. Early studies of magnetized-fluidized beds. **Powder Technology. 57**:213-220.

17. Herschler, A. 1965. Fluid treating method and apparatus. U.S. Patent 3 219 318.

18. Herschler, A. 1969. Method for production and control of fluidized beds. U.S. Patent 3 439 899.

19. Katz, H. 1967. Method of stabilizing a fluidized bed using a glow discharge. U.S. Patent 3 4 249.

20. Katz, H., and J.T. Sears. 1969. Electric field phenomena in fluidized and fixed beds. **The Canadian Journal of Chemical Engineering. 47**:50.

21. Shumkov, S.H., and D.G. Ivanov. 1975. **Khim. Ind. 47**(10):442.

22. Nekrasov, Z.I., and V.V. Chekin. 1961. **Izv. Akad. Nauk. Otd. Tekh. Nauk. Met. iToplivo. 6**:25.

23. Ivanov, D.G., and S.H. Shumkov. 1974. **Khim. Ind. 46**(3):108.

24. Ivanov, D.G., and S.H. Shumkov. 1972. **God. Vissh. Khimi. Kotekhnol. Inst. 19**(1):141.

25. Shumkov, S.H., and D.G. Ivanov. 1977. **God. Vissh. Khimi. Kotekhnol. Inst. 22**(3):87.

26. Shumkov, S.H., and D.G. Ivanov. 1976. **Zhurnal Prik. Khimii. 49**(11):2406.

27. Bologa, M.K., and S.V. Syutkin. 1977. **Electron Obrab Mater. 68**:37.

28. Bologa, M.K., and S.V. Syutkin. 1976. **Electron Obrab Mater. 6**:61.

29. Liu, Y.A., R.K. Hamby, and R.D. Colberg. 1991. Fundamental and practical developments of magnetofluidized beds: a review. **Powder Technology. 640**:3-41.

30. Rosensweig, R.E. 1979. Hydrocarbon conversion process utilizing a magnetic field in a fluidized bed of catalytic particles. U.S. Patent 4 136 016.

31. Rosensweig, R.E., 1979. Magnetic Stabilization of the state of uniform fluidization. **Industrial and Engineering Chemistry Fundamentals. 18**(3):260-269.

32. Lee, W.K. 1983. the rheology of magnetically stabilized fluidized solids. **AIChE Symposium Series. 79**(222):87-96.

33. Arnaldos, J., J. Casal, A. Lucas, and L. Puigjaner. 1985. Magnetically stabilized fluidization: modelling and application to mixtures. **Powder Technology. 44**:57-62.

34. Arnaldos, J., and J. Casal. 1987. Study and modelling of mass transfer in magnetically stabilized fluidized beds. **International Journal of Heat and Mass Transfer.** (7):1525-1529.

35. Siegell, J.H. 1987. Liquid-fluidized magnetically stabilized beds. **Powder Technology. 52**:139-148.

36. Goetz, V., and D.J. Graves. 1991. Axial dispersion in a magnetically stabilized fluidized bed liquid chromatography column. **Powder Technology. 64**:81-92.

37. Burns, M.A., and D.J. Graves. 1988. Structural studies of a liquid-fluidized magnetically stabilized bed. **Chemical Engineering Communications. 67**:315-330.

38. Hu, T.T., and J.Y. Wu. 1987. Study on the characterization of a biological fluidized bed in a magnetic field. **Chemical Engineering Research and Design. 65**:238.

39. Kwauk, M. X. Ma, F. Ouyang, Y. Wu, D. Weng, and L. Cheng. 1992. Magnetofluidized G/L/S systems. **Chemical Engineering Science. 47**(13/14):3467-3474.

40. Wang, Y., E. Jaraiz-M, O. Levenspiel, and T.J. Fitzgerald. 1982. A magnetic control valve for flowing solids (MVS): exploratory studies. **Industrial and Engineering Chemistry Process Design and Development. 21**:717.

41. Wang, Y. E. Jaraiz-M, G.T. Zhang, R.T. Chan, and O. Levenspiel. 1983. The MDD: a magnetic distributor for fluidized beds: preliminary studies. In **Fluidization**. D. Kunii and R. Toei (eds.). Engineering Foundation, New York. p 241.

42. Fitzgerald, T.J., and O. Levenspiel. 1984. Magnetic distributor-downcomer for fluidized beds and magnetic valve to control the flow of solids. U.S. Patent 4 463 502.

43. Jaraiz-M, E., G.T. Zhang, Y. Wang, and O. Levenspiel. 1984. The magnetic distributor-downcomer (MDD) for fluidized beds. **Powder Technology. 38**:53.

44. Pirkle, J.C. Jr., P.A. Ruziska, and L.J. Shulik. 1988. Circulating magnetically stabilized bed reactors. **Chemical Engineering Communications. 67**:89.

45. Luchesi, P.J., W.H. Hatch, F.X. Mayer, and R.E. Rosensweig. 1979. Magnetically stabilized beds: new gas-solids contacting technology. Proceedings of the 10th World Petroleum Congress. Bucharest, Heyden, Philadelphia. 4:419.

46. Coulaloglou, C.A., and J.H. Siegell. 1981. Continuous countercurrent fluid-solids contacting process stabilized by a magnetic field. U.S. Patent 4 247 987.

47. Savage, D.W. 1981. Process for the separation of contaminants from feed streams using magnetic beds. U.S. Patent 4 283 204.

48. Pirkle, J.C. Jr. 1987. Continuous sorption process. U.S. Patent 4 655 796.

49. Burns, M.A., and D.J. Graves. 1985. Continuous affinity chromatography using a magnetically stabilized fluidized bed. **Biotechnolgy Progress. 1**(2):95-103.

50. Siegell, J.H., G.D. Dupre, and C.J. Pirkle Jr. 1986. Chromatographic separations in a cross-flow MSB. **Chemical Engineering Progress.** November. pp 57-61.

51. Burns, M.A. and D.J. Graves. 1987. The magnetically stabilized fluidized bed as a biochemical processing tool. **Annals of the New York Academy of Sciences, Enzyme Engineering 8.** A.I. Laskin, K. Mosbach, D. Thomas, and L.B. Wingard Jr. (eds.). Vol. 501. pp. 103-107.

52. Bramble, J.L., D.J. Graves, and P. Brodelius. 1990. Plant cell culture using a novel bioreactor: the magnetically stabilized fluidized bed. **Biotechnology Progress. 6**:452-457.

53. Wild, G. M. Saberian, J.L. Schwartz, and J.C. Charpentier. 1984. Gas-liquid-solid fluidized bed reactors. State of the art and industrial possibilities. **International Chemical Engineering. 24**(4):639-676.

54. Bhatia, V.K., and N. Epstein. 1972. Three-phase fluidization: a generalized wake model. Proceedings of the International Symposium on Fluidization and Its Applications. Cepadues Editions, Toulouse. p. 380.

55. Achwal, S.K., and J.B. Stepanek. 1975. An alternative method of determining hold-up in gas-liquid systems. **Chemical Engineering Science. 30**:1443.

56. Miller, N. and R.E. Mitchie. 1970. Measurement of local voidage in liquid/gas two phase flow systems using a universal probe. **Journal of the British Nuclear Society. 9**(2):94-100.

57. DeLasa, H., S.L.P. Lee, and M.A. Bergougnou. 1984. Bubble measurement in three-phase fluidized beds using a U-shaped optical fiber. **The Canadian Journal of Chemical Engineering. 62**:165-169.

58. Abuaf, N., O.C. Jones Jr., and G.A. Zimmer. 1978. Optical probe for local void fraction and interface velocity measurements. **Review of Scientific Instruments. 49**(8):1090-1094.

59. Ishida, M. and T. Hitashi. 1982. An optical probe to detect both bubbles and suspended particles in a three-phase fluidized bed. **Journal of Chemical Engineering. 15**(5):389-391.

60. Bailey, J.E., and D.F. Ollis. 1986. **Biochemical Engineering Fundamentals.** McGraw-Hill, New York. 2nd ed.

61. Wakao, N., and S. Kaguei. 1982. Parameter estimation from tracer response measurements. In **Heat and Mass Transfer in Packed Beds.** Gordon and Breach, New York. pp. 1-71.

62. Alvarez-Cuenca, M., and M.A. Nerenberg. The two-zone model: a quantitative description of the oxygen mass transfer in bubble columns and three phase fluidized beds. In **Advances in Biotechnology.** Pergammon Press. 1:643-650.

63. Decker, W.D., R. Burchhart, and G. Zoll. 1974. Mixing and mass transfer in tall bubble columns. **Chemical Engineering Science. 29**:2177-2188.

64. Kim, S.D., G.J. Baker, and M.A. Bergougnou. 1972. Holdup and axial mixing characteristics of two and three phase fluidized beds. **The Canadian Journal of Chemical Engineering. 50**:695-701.

65. Singh, V., W. Hensler, R. Fuchs, and A. Constantinides. 1986. On-line determination of mixing parameters in fermentors using pH tranisents. Proceedings of the International Conference of Bioreactor Fluid Dynamics. Paper no. 18. pp 231-256.

66. Michelsen, M.L., and K. Ostergaard. 1970. Hold-up and fluid mixing in gas-liquid fluidized beds. **The Chemical Engineering Journal.** 1:37-45.

67. Lubbert, A., T. Korte, and B. Larson. 1986. Simple measuring techniques for the determination of bubble and bulk-phase velocities in bioreactors. Proceedings of the International Conference on Bioreactor Fluid Dynamics. Paper no. 3. pp 33-43.

68. Ostergaard, K. and M.L. Michelsen. 1969. **The Canadian Journal of Chemical Engineering.** 47:107.

69. Anderssen, A.S., and E.T. White. 1971. **Chemical Engineering Science.** 26:1203.

70. Hopkins, M.J., A.J. Sheppard, and P. Eisenklam. 1969. **Chemical Engineering Science.** 24:1131.

71. Gangwal, S.K., R.R. Hudgins, A.W. Byrson, and P.L. Silveston. 1971. **The Canadian Journal of Chemical Engineering.** 49:113.

72. Dunn, I.J., and A. Einsele. 1975. Oxygen transfer coefficients by the dynamic method. **Journal of Applied Chemistry and Biochemistry.** 25:707-720.

73. Heineken, F.G. 1970. **Biotechnology and Bioengineering.** 12:145.

74. Heineken, F.G. 1971. **Biotechnology and Bioengineering.** 13:599.

75. Linek, V. 1972. **Biotechnology and Bioengineering.** 14:285.

76. Linek, V., M. Sobotha, and A. Prokop. 1973. **Biotechnology and Bioengineering Symposium.** 4:429.

77. Van't Riet, K. 1979. Review of measuring methods and results in nonviscous gas-liquid mass transfer in stirred vessels. **Industrial and Engineering Chemistry Process Design and Development.** 18(3):357-364.

78. Eroglu, I, and T. Dogu. 1987. Significance of boundary conditions in a two phase flow system with mass transfer. **Chemical Engineering Science.** 42(1):169-172.

79. Deckwer, W.D., K. Nguyen-Tien, A. Schumpe, and Y. Serpemen. 1982. Oxygen mass transfer into aerated CMC solutions in a bubble column. **Biotechnology and Bioengineering. 24**:461-481.

80. Tang, W.T., and L.S. Fan. 1990. Gas-liquid mass transfer in a three phase fluidized bed containing low density particles. **Industrial and Engineering Chemistry Research. 29**:128-133.

81. Montgomery, D.B. 1969. **Solenoid Magnet Design.** Wiley-Interscience, New York.

82. Bendat, J.S., and A.G. Piersol. 1971. **Random Data: Analysis and Measurement Procedures.** Wiley-Intersciences, New York. pp. 1-35.

83. Moore, C.F., C.L. Smith, and P.W. Murrill. Multidimensional optimization using PATERN search. Louisiana State University, Baton Rouge, Louisiana.

84. Nguyen, A.-L., and J.H.T. Luong. 1986. Diffusion in κ-carrageenan gel beads. **Biotechnology and Bioengineering. 27**:1261-1267.

85. Crank, J. 1975. **The Mathematics of Diffusion.** 2nd ed. Oxford University Press, New York. pp. 93-97.

86. Cheetham, P.S.J., K.W. Blunt, and C. Bucke. 1979. Physical studies on cell immobilization using calcium alginate gels. **Biotechnology and Bioengineering. 21**:2155-2168.

87. Stone, J.E., A.M. Scallan, E. Donefer, and E. Ahlgren. 1969. Digestibility as a simple function of a molecule of similar size to a cellulase enzyme. **Advances in Chemistry Series. 95**:219.

88. Stone, J.E., and A.M. Scallan. 1968. A structural model for the cell wall of water-swollen wood pulp fibres based on their accessibility to macromolecules. **Cellulose Chemistry and Technology. 2**:343-358.

89. Thompson, D.N. 1989. The effect of physical and chemical constraints on the enzymatic hydrolysis of lignocellulosic materials. Master's Thesis, Michigan State University.

90. Weimer, P.J., and W.M. Weston. 1985. Relationship between the fine structure of native cellulose and cellulose degradability by the cellulase complexes of *Trichoderma reesi* and *Clostridium thermocellum*. **Biotechnology and Bioengineering. 27**:1450.

91. Carslaw, H.S., and J.C. Jaeger. 1959. **Conduction of Heat in Solids.** Oxford University Press, New York.

92. Rosen, J.B. 1952. Kinetics of a fixed bed system for solid diffusion into spherical particles. **Journal of Chemistry and Physics. 20**:387.

93. Rasmuson, A., and I. Neretnieks. 1980. Exact solution of a model for diffusion in particles and longitudinal dispersion in packed beds. **AIChE Journal. 26**(4):686-690.

94. Rice, J.A. 1988. **Mathematical Statistics and Data Analysis.** Wadsworth and Brooks/Cole, Pacific Grove, California.

95. Perry, R.H., D.W. Green, and J.O. Maloney (eds.). 1984. **Perry's Chemical Engineers' Handbook.** 6th ed. Mcgraw-Hill Book Company, New York.

96. Davison, B.H. 1989. Dispersion and holdup in a three-phase fluidized-bed bioreactor. **Applied Biochemistry and Biotechnology. 20/21**:449-460.

97. Muroyama, K. and Liang-Shih Fan. 1985. Fundamentals of gas-liquid-solid fluidization. **AIChE Journal. 31**(1):1-33.

98. Kim, S.D., and C.H. Kim. 1983. Axial dispersion characteristics of three-phase fluidized beds. **Journal of Chemical Engineering of Japan. 16**:172.

99. Andrews, G. 1988. Fluidized-beds bioreactors. **Biotechnology and Genetic Engineering Reviews. 6**:151-178.

100. Whitten, K.W., and K.D. Gailey. 1981. **General Chemistry.** Saunders College Publishing, Philadelphia, Pennsylvania.